UNIVERSIDADE DE SÃO PAULO
INSTITUTO DE FÍSICA DE SÃO CARLOS

Rafael Besse

Ab initio study of structural, energetic, and electronic properties of two-dimensional transition metal dichalcogenides

São Carlos

2021

Rafael Besse

Ab initio study of structural, energetic, and electronic properties of two-dimensional transition metal dichalcogenides

Thesis presented to the Graduate Program in Physics at the Instituto de Física de São Carlos, Universidade de São Paulo, to obtain the degree of Doctor in Science.

Concentration area: Basic Physics

Advisor: Prof. Dr. Juarez Lopes Ferreira da Silva

Corrected version
(Original version available on the Program Unit)

São Carlos
2021

Besse, Rafael
Ab initio study of structural, energetic, and electronic properties of two-dimensional transition metal dichalcogenides / Rafael Besse; advisor Juarez Lopes Ferreira da Silva - corrected version -- São Carlos 2021.
160 p.

Thesis (Doctorate - Graduate Program in Basic Physics) -- Instituto de Física de São Carlos, Universidade de São Paulo - Brasil , 2021.

1. Two-dimensional materials. 2. Transition metal dichalcogenides. 3. van der Waals heterobilayers. I. da Silva, Juarez Lopes Ferreira, advisor. II. Title.

ACKNOWLEDGEMENTS

I am very grateful to my supervisor Prof. Dr. Juarez Lopes Ferreira da Silva for his well organized and hard work to provide a helpful and fruitful guidance, and also for the immense contribution to my scientific formation since my undergraduate research project and master's study.

Many thanks to the colleagues and friends of the QTNano group, especially Alexandre C. Dias, Augusto C. H. Da Silva, Carlos M. O. Bastos, Diego Guedes-Sobrinho, Julian F. R. V. Silveira, Mailde S. Ozório, Naidel A. M. S. Caturello, and Vivianne K. Ocampo-Restrepo for the constructive discussions and for the good times we spent together. I also thank Prof. Dr. Matheus Paes Lima for the collaboration.

I wish to thank Prof. Dr. Shengbai Zhang for having me in his research group at the Rensselaer Polytechnic Institute and for the valuable contributions to the research projects developed during my stay, and the group members for the shared knowledge, especially Dr. Damien West. I also thank Dr. Han Wang for his helpful contributions.

I gratefully acknowledge FAPESP for the doctoral scholarship (grant 2017/09077-7) and the scholarship for research internship abroad (grant 2019/09276-5). I also gratefully acknowledge CNPq for the 11 months of doctoral scholarship (140737/2017-0). I would like also to thank IFSC, IQSC, and staffs for the infrastructure and assistance to develop this work. I acknowledge the computational infrastructure provided by the Department of Information Technology and the Information Technology Superintendence of the University of São Paulo, and also LNCC/MCTI for HPC resources of the SDumont supercomputer.

Lastly, I would like to extend my deepest gratitude to my family, especially my parents, Sandra and Luiz Carlos, for the support and encouragement.

ABSTRACT

BESSE, R. **Ab initio study of structural, energetic, and electronic properties of two-dimensional transition metal dichalcogenides**. 2021. 160p. Thesis (Doctor in Science) - Instituto de Física de São Carlos, Universidade de São Paulo, São Carlos, 2021.

The advances in techniques for the isolation and synthesis of two-dimensional materials have opened new paths for the investigation of novel physical phenomena and properties, with great potential for technological innovation. In this context, transition metal dichalcogenides form a prominent class of compounds, due to their unique electronic and optical properties. This thesis aims to contribute to the understanding of the physical properties of two-dimensional transition metal dichalcogenides, studying a wide variety of systems by means of calculations based on density functional theory and time-dependent density functional theory combined with molecular dynamics. The analysis of relative phase stability in $MoSe_2$ showed that the Peierls transition mechanism leads to the stabilization of the distorted octahedral phase, and a phase preference transition induced by the nanoflakes sizes was demonstrated. By investigating two-dimensional materials based on dichalcogenides of transition metals of groups 8 to 11, it was found that weak interlayer binding, typical of two-dimensional materials, occurs in the systems with transition metals of groups 8 and 10, whereas a strong contribution of chemical bonds was observed in the remaining materials. The identified semiconductor monolayers also have transition metals from groups 8 and 10, and the chemical trends of band offsets could be explained and employed with Anderson's rule to predict junction types of heterobilayers. With the examples of the heterobilayers of MQ_2 (M = Mo, Ni, Pt; Q = S, Se), it was found that although interlayer binding is dominated by weak interactions, interlayer coupling can significantly influence band gaps beyond the approximation of Anderson's rule. Two mechanisms are crucial for these effects, namely, the interlayer hybridization of electron states and the formation of electric dipole at the interface, which was explained by a simple physical model. In the $MoS_2/PtSe_2$ heterobilayer, it was observed that a photoexcitation across the band gap of MoS_2 generates electron transfer to the $PtSe_2$ layer at a faster rate than hole transfer, leading to an effective charge separation, despite the type-I band alignment. Both carriers transfers are influenced by the level crossings induced by the interfacial dipole caused by the imbalance in charge transfer.

Keywords: Two-dimensional materials. Transition metal dichalcogenides. van der Waals heterobilayers.

RESUMO

BESSE, R. **Estudo ab initio das propriedades estruturais, energéticas e eletrônicas de dicalcogenetos de metais de transição bidimensionais**. 2021. 160p. Tese (Doutorado em Ciências) - Instituto de Física de São Carlos, Universidade de São Paulo, São Carlos, 2021.

Os avanços nas técnicas de isolamento e síntese de materiais bidimensionais abriram novos caminhos para a investigação de novos fenômenos e propriedades físicas, com grande potencial para inovações tecnológicas. Nesse contexto, dicalcogenetos de metais de transição formam uma classe proeminente de compostos, devido às suas propriedades eletrônicas e ópticas únicas. Essa tese visa contribuir com o entendimento das propriedades físicas de dicalcogenetos de metais de transição, estudando uma ampla variedade de sistemas por meio de cálculos com base na teoria do funcional da densidade e teoria do funcional da densidade dependente do tempo combinada com dinâmica molecular. A análise da estabilidade relativa das fases em $MoSe_2$ mostrou que o mecanismo de transição de Peierls leva à estabilização da fase octaédrica distorcida, e uma transição de preferência de fase induzida pelos tamanhos de nanoflocos foi demonstrada. Pela investigação de materiais bidimensionais com base em dicalcogenetos dos metais de transição dos grupos 8 a 11, foi encontrado que a fraca interação entre camadas, típica de materiais bidimensionais, ocorre em sistemas com metais de transição dos grupos 8 e 10, enquanto uma grande contribuição de ligações químicas foi observada nos demais materiais. As monocamadas semicondutoras identificadas também possuem metais de transição dos grupos 8 e 10, e as tendências químicas de deslocamentos de bandas puderam ser explicadas e utilizadas com a regra de Anderson para prever tipos de junções em heterobicamadas. Com os exemplos das heterobicamadas de MQ_2 (M = Mo, Ni, Pt; Q = S, Se), foi encontrado que embora a ligação entre camadas seja dominada por interações fracas, o acoplamento entre camadas pode influenciar singnificativamente o *band gap* além da aproximação da regra de Anderson. Dois mecanismos são cruciais para esses efeitos, especificamente, hibridizações de estados eletrônicos entre camadas e a formação de dipolo elétrico na interface, que foi explicada por um modelo físico simples. Na heterobicamada $MoS_2/PtSe_2$, foi observado que uma fotoexcitação no *band gap* de MoS_2 gera transferência de elétrons para $PtSe_2$ em uma taxa mais rápida que a transferência de buracos, levando a uma separação efetiva de carga, apesar do alinhamento tipo-I. As transferências dos dois portadores são influenciadas por cruzamentos de níveis induzidos pelo dipolo interfacial causado pela desigualdade na transferência de carga.

Palavras-chave: Materiais bidimensionais. Dicalcogenetos de metais de transição. Heterobicamadas de van der Waals.

LIST OF FIGURES

LIST OF TABLES

LIST OF ABBREVIATIONS AND ACRONYMS

2D	Two-dimensional
ALDA	Adiabatic local density approximation
BO	Born–Oppenheimer
CBM	Conduction band minimum
DFT	Density functional theory
DOS	Density of states
ELF	Electron localization function
FBZ	First Brillouin zone
f.u.	Formula unit
GGA	Generalized gradient approximation
HF	Hartree–Fock
HK	Hohenberg–Kohn
KS	Kohn–Sham
LDA	Local density approximation
LR	Long range
LCAO	Linear combination of atomic orbitals
MD	Molecular dynamics
PAW	Projector augmented wave
PCE	Power conversion efficiency
RG	Runge–Gross
SIESTA	Spanish Initiative for Electronic Simulations with Thousands of Atoms
SR	Short range
TDAP	Time Dependent *Ab initio* Package
TDDFT	Time dependent density functional theory

TM	Transition metal
TMD	Transition metal dichalcogenides
VASP	Vienna *Ab initio* Simulation Package
VBM	Valence band maximum
vdW	van der Waals

CONTENTS

1 INTRODUCTION

This thesis presents a study on the physical properties of two-dimensional (2D) materials, specifically the family of transition metal dichalcogenides (TMDs). In this chapter, the factors that drive the interest in investigating these materials are discussed, followed by an introduction to their fundamental characteristics. A review of current scientific challenges related to the understanding and control of the properties of 2D TMDs is presented, highlighting the open problems to be addressed, based on which the objectives of this work are defined.

1.1 Motivation

The experimental isolation of graphene,[1] a 2D honeycomb lattice of carbon with one-atom thickness, has opened up a new road for advances in the development of low-dimensional devices. The method that was discovered to obtain graphene crystallites was also successfully applied to isolate monolayers of other 2D materials,[2] also defined by one- or few-atoms thicknesses, thus creating a huge potential for the investigation of properties and phenomena of a wide range of 2D materials. Initially, the efforts were essentially concentrated on graphene, mostly due to the observation of excellent electronic properties of its isolated crystals, for example, the high charge carrier mobility, even at chemically and electronically induced high carrier concentrations.[3] However, some limitations were encountered for graphene, for example, the lack of a band gap is a challenge for its application in electronics and optoelectronics, and therefore, other 2D materials have been brought to the limelight. Hexagonal boron nitride (h-BN), an insulator that shares graphene's honeycomb structure, but with a small lattice constant mismatch, was shown to yield good device quality when employed as substrate for graphene.[4] TMDs, which are among the most important and widely studied 2D materials, appeared as excellent candidates for semiconducting applications, due to their natural band gaps.[5]

The library of already known 2D materials is not restricted to the previous examples and advances have been made in other compounds, such as elemental materials other than graphene (e.g. silicene[6] and black phosphorous[7]), MXenes,[8] ternary trichalcogenides,[9] and perovskites.[10] The vast majority of 2D materials are obtained from layered van der Waals (vdW) solids, which are formed by the stacking of layers, where intralayer bonding is dominated by covalent and ionic bonds and the layers are bound by vdW forces. Therefore, the impressive rise in the importance of 2D materials has driven several efforts to identify layered vdW solids among already known crystal structures.[11–14] In this context, the evaluation of the magnitude of interlayer binding, the exfoliation energy,[15] is important to access the potential exfoliability of layered solids. Of these, 2D TMDs

have attracted special attention due to their excellent properties for multiple promising applications, for example nanoelectronics,[16] electrocatalysis,[17] and thermoelectrics.[18]

Existing methods for isolating sheets of 2D materials can be classified in two main categories: top-down and bottom-up methods. Top-down methods consist in the exfoliation of layers from a layered crystal, for instance, through mechanical exfoliation, as in the Schotch tape method, that was employed to exfoliate graphite in the first isolation of graphene.[1] This method allows to obtain crystals with good quality employing fairly cheap and readily available apparatus, but does not offer a scalable way of obtaining monolayers of 2D materials. This deficiency is overcome with another top-down approach, namely liquid-phase exfoliation, that consists in separating the layers from the crystal through sonication in a liquid solution.[19] Although this method allows high scalability compared to mechanical exfoliation, there can be drawbacks, such as the quality and size of exfoliated crystals.[20] These exfoliation methods contrast with approaches in which sheets are directly grown, often called bottom-up methods, which offer potential for high degree of morphological control and scalability, specially with chemical vapor deposition.[21]

The progress in the techniques to obtain and manipulate 2D sheets and the knowledge of the vast library of 2D materials made possible to design materials through the controlled vertical stacking of different monolayers in a chosen sequence, often called vdW heterostructures, which enabled an important route to explore novel properties and phenomena within 2D materials.[22,23] The interlayer binding is dominated by weak vdW interactions, thus allowing to explore combinations of the numerous 2D materials relaxing the condition of strict lattice matching of usual heterojunctions. In particular, vdW heterostructures based on TMDs have exhibited promising properties for several applications, such as photodetectors,[24] light emitters,[25] photocatalysis,[26] nanoelectronic[27] and spintronic devices,[28] which reveals the versatility of TMDs for the design of vdW heterostructures, in which a suitable band alignment between component layers is an important factor.[29] Therefore, the study of 2D TMDs is a key step to guide the advances in the design of novel 2D materials and vdW heterostructures.

1.2 Two-dimensional transition metal dichalcogenides

TMDs are compounds with chemical formula MQ_2, where M is a transition metal (TM) and Q is a chalcogen, specifically, S, Se, and Te. Among the most important factors that contribute to the interest in 2D TMDs is the possibility to modify their physical and chemical properties through layer stacking,[30] exploration of the large number of possible chemical compositions,[31] and alloying.[32] The interest in TMDs for 2D materials has been mainly focused on compositions with group 6 TMs, namely, the sulfides and selenides of Mo and W, and also, but to a lesser extent, on compositions with TMs from groups 4, 5 and 10. This is because in these compounds, TMDs crystallize in vdW layered structures,[31]

and therefore, they facilitate the obtention of ultrathin 2D sheets.

Layered TMDs can be found in a variety of polymorphs, which can differ on the intralayer arrangement of atoms and also on the stacking pattern of the layers.[31,33] The monolayers are composed of a plane of TM atoms in a triangular lattice that is sandwiched between two planes of chalcogen atoms, also in triangular lattices. Three main monolayer phases are found and their main difference is the coordination environments of TM atoms, which can be trigonal prismatic, octahedral, or distorted octahedral, and the stacking of these monolayers leads to the different bulk crystal polytypes. The trigonal prismatic coordination occurs in the bulk 2H phase,[31] which has monolayer stacking sequence AbA BaB, capital and lower case letters indicate the alignment of chalcogen and metal atomic planes, respectively. This phase is the lowest energy crystal structure of most group 6 TMDs, for instance MoS_2, WS_2 and $MoSe_2$.[31,34] The octahedral coordination is observed in the bulk 1T phase,[31] with stacking sequence AbC AbC. Notably, this is the lowest energy phase of group 4 TMDs, for example, TiS_2, ZrS_2, and $ZrSe_2$.[31,34] Monolayers of the distorted octahedral phase can be generated by reconstructions in the octahedral monolayer, mainly with displacements of metal atoms rows. This type of configuration is observed in the bulk 1T′ phase,[33] which is the ground state crystal structure of WTe_2.[34]

An important factor to determine which of the layered structural phases is adopted by a TMD is the d electron count of the TM atom. The different coordination environments and symmetries of each coordination environment generate differences in the electronic structure, particularly in the splitting of the d orbital levels.[31,33] As a consequence, the number of electrons that occupy these levels influences the relative energy of phases, which can explain why the 2H phase is favored for MoQ2 compounds but 1T is favored for TiQ_2. The structural diversity of TMDs leads to important consequences for their physical properties, and a single compound can have marked differences between different phases. For example, Mo dichalcogenides are semiconductors in the 2H phase and metals in the 1T phase,[35] whereas the 1T′ phase has attracted interest because of the possibility to obtain quantum spin Hall phases.[36] Therefore, the diversity of crystal structures also contributes to the wide range of chemical and physical properties found in 2D TMDs.

1.3 State of the art in the study of transition metal dichalcogenides

The intense research activity on 2D TMDs in the past decade has opened up several routes to understand and exploit the physical properties and phenomena observed in these materials, and consequently a wide range of topics within the study of 2D TMDs are currently relevant. Here, recent advances and open problems are reviewed, focusing on the topics related to the scope selected for this thesis, namely, TMDs nanoflakes, development of novel 2D materials based on TMDs, band gaps of vdW heterostructures, and interfacial charge carrier transfer in vdW heterostructures.

1.3.1 Transition metal dichalcogenides nanoflakes

Along with the advances in 2D TMDs, there have been also efforts focused on 2D TMDs nanostructures with small lateral size,[37] motivated by the capacity of tuning nanomaterials properties through the control of size. Typically, this classification encompasses nanostructures with lateral sizes below 100 nm,[37] termed nanoflakes, which preserve the attractive properties of the large 2D monolayers, and have some advantages derived from the enhancement of quantum confinements effects and active edge sites. For instance, the presence of dangling bonds at the edges with a high surface-to-volume ratio favors the application in photocatalysis,[38] and potential applications for TMDs nanoflakes also include chemical sensors,[39] cell imaging,,[40] and many other technologies for sensing, biomedicine, and energy sources.[37]

Because of the important role of the structural phase in the properties of 2D TMDs, including nanoflakes, there is great interest in developing strategies to control their phase stability. Several approaches have been employed to induce transitions between the semiconducting and metallic phases, such as exposure to chemical vapor of organic electron donors,[35] insertion of Li atoms,[41] and electron beam irradiation.[42] These strategies are based on modifying the electron count via transfer of electrons to the TMD sheets, but other strategies have been proposed, for instance, the application of strain, given the different energy response to stain of the different phases.[43] However, all these strategies have been explored in sheets with lateral sizes in the micrometer scale, and theoretical results on semi-infinite MoS_2 nanoribbons have shown that the nanoribbons width is correlated to the relative phase stability.[44] Therefore, the role of nanoflakes sizes on the relative stability of 2D TMDs phases, as well as the effects on the physical properties must be further investigated.

1.3.2 Development of novel 2D materials

With the surge in interest in 2D materials, various studies have been developed to screen vdW layered solids by searching and classifying crystals reported in databases of crystal structures.[12–14] This approach is useful to identify candidates for the obtention of novel 2D materials, by pointing out systems whose structural features and interlayer binding strength are favorable for the exfoliation of monolayers. These studies are limited to already known vdW layered solids, which does not cover all possibilities of finding 2D materials, since there has been success in the obtention of 2D sheets from crystals not characterized by vdW stacking of layers, such as Ga_2O_3[45] and Fe_2O_3.[46] Furthermore, theoretical studies have verified the fulfillment of conditions for thermodynamic and kinetic stability of monolayers for compounds not known in layered crystals, including TMDs[47] and the II-VI and III-V compositions of traditional 3D semiconductors.[48] Therefore, the search for novel 2D materials is not restricted to compounds that are known to adopt

layered crystal structures, and due to the diversity of physical and chemical properties of TMDs, the large scale exploration of these compounds is a viable path to identify 2D materials with interesting properties.

The dichalcogenides of Mo and W are the most common examples of 2D TMDs, and vdW layered TMD solids are also found for other TMs from groups 4 to 7 and and some of the compositions of group 10 TMs.[31] For other TMs, a small number of layered crystal structures have been reported, for example, $IrTe_2$ in the 1T structure,[49] but the majority of these compounds are traditionally known to adopt a variety of crystal phases not formed of stacked layers,[50] such as the pyrite[51] and marcasite[52] crystal structures of FeS_2. Theoretical studies on novel 2D TMDs have indicated the potential to synthesize stable monolayers with TMs of groups 8 to 11,[47,53] and obtained their electronic properties, but these investigations employed only isolated monolayers. Therefore, it is crucial to examine the interlayer interactions in these systems, to obtain a deeper understanding of the effects of layer stacking on the electronic properties and of the interlayer binding.

1.3.3 Band gap design of vdW heterostructures

Semiconductor heterojunctions of vdW heterostructures of 2D TMDs have been found promising to develop materials for various technological devices, such as nanotransistors,[54] photocatalysts,[55] and photovoltaic cells.[56] In this context, obtaining vdW heterostructures with suitable band gaps and band alignments is crucial. Depending on the band alignments, semiconductor junctions are usually classified into three cases, each of them possessing features that can lead to advantages for specific applications.[57] Type-I or straddling gap junctions, are the cases in which both valence band maximum (VBM) and conduction band minimum (CBM) are located at the same side of the junction, and they favor efficient recombination of charge carriers due to the spatial confinement, leading to enhanced photoluminescence and potential for application in light-emitting devices.[58] Type-II or staggered gap junctions have VBM and CBM located in different sides of the junction, which facilitates spatial separation of electrons and holes, and therefore, increases the lifetime of these charge carriers, a desirable property for solar cells and photocatalysts.[55] Type-III or broken gap junctions are the cases with no overlaps of band gaps, that is, the VBM of one side of the junction is above the CBM of the other, which has been employed for the development of tunnel diodes.[59]

Owing to the dominant role of vdW forces in the interlayer interactions, vdW heterostructures are expected to be well suited for a description of band alignments with Anderson's rule,[60] also termed electron affinity rule. Within this approximation, the band offsets at the interface are assumed to be equal to the natural band offsets of the materials that form the heterojunction, which also allows to evaluate the heterostructure band gap as the difference between the lowest CBM ad highest VBM among the materials.

This approximation corresponds to neglecting the effects of hybridization and charge redistribution at the interface, which is expected to be accurate for vdW heterostructures in the absence of interlayer chemical bonding. A good validity of this approach has been demonstrated, for instance, in experimental measurements of MoS_2/WS_2 and MoS_2/WSe_2 heterostructures.[61] In view of this, theoretical studies have widely employed Anderson's rule to predict band alignments and band structures of vdW heterobilayers.[29,53,57,62,63]

Although Anderson's rule is expected to have good validity in vdW layered systems, interlayer electronic coupling can play an important role in the electronic structure of these systems. This is notable in materials formed of identical stacked layers, such as observed in group 6 TMDs with the transition from direct band gap to indirect band gap going from monolayer to bulk, due to the interlayer coupling of band edge states,[30,64] and also in the strong dependency of PtS_2 band gap on layer number.[65] Similar behaviors have been reported for heterobilayers based on theoretical studies of systems composed of TMDs and tin dichalcogenides[66] and of IV-V monolayers,[67] where deviations from Anderson's rule are caused by interlayer hybridizations. In view of that, obtaining further understanding on the effects of interlayer coupling on the band gaps of TMDs vdW heterostructures is important to guide the design of these materials for application in technological devices.

1.3.4 Interlayer charge carrier transfer

The interfacial transfer of charge carriers in heterojunctions plays a fundamental role in semiconductor devices. Therefore, developing a deep understanding of this process is crucial for the development of functional junctions, which requires going beyond the description of band alignments and addressing other relevant aspects, such as the dynamics of the charge transfer process. In vdW heterostructures, the predominance of weak vdW interactions between monolayers might suggest that interlayer charge carrier transfer could be inhibited, however, ultrafast transfer has been experimentally observed in heterostructures based on TMDs.[68,69] These observations sparked interest in the understanding of the mechanisms that enable the surprisingly small time-scales of charge carrier transfer in vdW heterostructures.[70] Based on the simulation of photoexcited states in TMD heterobilayers, it has been proposed that dipole coupling across the interface is a significant factor to enable ultrafast charge transfer, which is therefore sensitive to the atomic arrangement at the interface.[71] The delocalization of photoexcited charge carrier states between the monolayers that form the heterojunction has also been pointed as a crucial feature that allows the ultrafast charge transfer in these systems.[72,73]

Most studies of interlayer charge transfer in TMDs vdW heterostructures have concentrated on type-II junctions, which is the most common band alignment type obtained with TMs from group 6, due to the common trends of valence and conduction band

offsets for these monolayers.[74] However, there is growing interest in exploring heterostructures with type-I junctions, motivated by their potential for application in photodetection and light-emitting devices.[75,76] In these systems, the band alignments favor the transfer of both holes and electrons to the same junction side, contrary to type-II junctions, and therefore, the mechanisms of charge carrier transfer deserve further investigation. Furthermore, the investigation of the dynamics of charge transfer between monolayers with dissimilar structural phases can shed more light into the role of the atomic arrangement at the interface in the mechanism of ultrafast charge transfer.

1.4 Objectives

1.4.1 General objectives

This thesis aims to contribute to the understanding of the physico-chemical properties of 2D TMDs. Among the wide range of currently interesting topics concerning these materials, this study focuses on a set of open problems related to the identification and understanding of major factors that can influence their properties, encompassing various types of systems, namely, nanoflakes, layered crystals, monolayers, and vertical heterobilayers. The main points addressed in the thesis are the role of size on the phase stability and electronic properties of nanoflakes, the characterization and screening of bulk and monolayer TMDs beyond usual compositions, the role of interlayer coupling on the electronic properties of vdW heterobilayers, and the study of interlayer charge carrier transfer in vdW heterobilayers. These topics are described in detail below, and the results related to each of them are discussed in separate chapters.

1.4.2 Specific objectives

- With $MoSe_2$ as example, study the structural properties of the different bulk and monolayer TMDs polytypes, and their relative stability. Obtain the relative energies of the trigonal prismatic and octahedral phases of $(MoSe_2)_n$ nanoflakes, with n ranging from 15 to 192, to investigate the role of nanoflake size on the phase stability, and to identify associated effects and consequences on the electronic properties.

- Obtain the equilibrium crystal structure configurations of the 36 MQ_2 compounds, with M = Fe, Ru, Os, Co, Rh, Ir, Ni, Pd, Pt, Cu, Ag, Au, and Q = S, Se, Te, for a set of layered and non-layered crystal phases reported for TMDs in the literature, and determine their relative stability based on the energy criterion. Characterize the interlayer binding of layered crystals, via the evaluation of the exfoliation energy and analysis of the electron density. Obtain the band gap of the lowest energy configurations of bulk and monolayers, and the band offsets of isolated semiconductor monolayers. Perform a preliminary screening of heterobilayers for application

in solar energy harvesting, based on an estimation of an upper limit for solar cell efficiency.

- Construct vertically stacked configurations for heterobilayers of MQ_2 monolayers, with $M =$ Mo, Ni, Pt, and $Q =$ S, Se, and evaluate equilibrium structural parameters and interlayer binding energies. Obtain the heterobilayer band gaps via Anderson's rule, based on the band offsets of isolated monolayers, and via the calculation of heterobilayers band structures. Compare the results to examine the validity of Anderson's rule, and investigate related effects by the analysis of band structures.

- Generate configurations for the 2H-MoS_2/1T-$PtSe_2$ vertical heterobilayer at different ionic temperatures, and identify the band edge states of MoS_2 for each configuration. Simulate the time evolution of a photoexcited system, corresponding to an electron excitation across the band gap of MoS_2, and evaluate the occupation of electrons and holes on each side of the heterobilayer interface. Identify mechanisms involved in the interlayer charge carrier transfer, through analysis of the features of wave functions and time evolution of electron states.

2 METHODOLOGY

This chapter summarizes the theoretical basis and developments of the methods employed in the studies discussed in this thesis, as well as the main aspects related the application of the methods. It is divided in: (2.1) Many-body problem; (2.2) Density functional theory; (2.3) Time-dependent density functional theory; (2.4) Periodic systems; (2.5) Basis sets; (2.6) Projector augmented-wave method; (2.7) Computational implementation.

2.1 Many-body problem

The quantum description of materials is fundamental for the understanding of their electronic properties and also allows to address several other aspects of the materials, such as obtaining structural properties and analyzing energy trends. Within this approach, the system is defined by the M nuclei and N electrons that compose it and their interactions, which can be described with the many-body Hamiltonian[77]

$$\begin{aligned}\hat{H} = &\sum_{i=1}^{N} -\frac{1}{2}\nabla_{\mathbf{r}_i}^2 + \sum_{\alpha=1}^{M} -\frac{1}{2M_\alpha}\nabla_{\mathbf{R}_\alpha}^2 + \sum_{i=1}^{N}\sum_{j=i+1}^{N}\frac{1}{|\mathbf{r}_i - \mathbf{r}_j|} + \\ &\sum_{\alpha=1}^{M}\sum_{\beta=\alpha+1}^{M}\frac{Z_\alpha Z_\beta}{|\mathbf{R}_\alpha - \mathbf{R}_\beta|} - \sum_{\alpha=1}^{M}\sum_{i=1}^{N}\frac{Z_\alpha}{|\mathbf{R}_\alpha - \mathbf{r}_i|} \ ,\end{aligned} \tag{2.1}$$

where atomic units were employed, i.e., electron mass, electron charge, reduced Planck constant, and $1/4\pi\epsilon_0$ have unit value. The first and second terms of the Hamiltonian correspond to the kinetic energy of electrons ($\hat{T}_e$) and nuclei ($\hat{T}_N$), respectively, and the third, fourth and fifth terms account for the Coulomb interactions between electrons ($\hat{V}_{ee}$), between nuclei ($\hat{V}_{NN}$), and between nuclei and electrons ($\hat{V}_{Ne}$), respectively.

Given the Hamiltonian of (2.1), the properties of the system are obtained via the wave function $\Psi(\{\mathbf{R}_\alpha\}, \{\mathbf{r}_i\})$, which is the solution of the time-independent Schrödinger equation

$$\hat{H}\Psi(\{\mathbf{R}_\alpha\}, \{\mathbf{r}_i\}) = E\Psi(\{\mathbf{R}_\alpha\}, \{\mathbf{r}_i\}) \ , \tag{2.2}$$

where $\{\mathbf{R}_\alpha\}$ and $\{\mathbf{r}_i\}$ denote the dependence on the sets of positions of nuclei and electrons, respectively, and E is the energy of the system.

The analytic solution of the Schrödinger equation is possible only for simple systems, such as hydrogen-like atoms and the quantum harmonic oscillator. Therefore, the solution of the many body problem requires the use of numerical methods, which can also benefit from approximations that simplify the description of the system. The Born–Oppenheimer (BO) approximation[78,79] consists in decoupling the dynamics of electrons and nuclei, and is widely used for calculations of atomic, molecular, and solid systems.

This approximation is based on the difference of the time scale of nuclear and electron dynamics, the latter being much smaller than the former, so that electrons can be considered to instantaneously adapt to changes in the atomic positions.

With the decoupling of the electronic motion and nuclear motions, the wave function can be written as the product of a nuclear and an electronic part

$$\Psi(\{\mathbf{R}_\alpha\},\{\mathbf{r}_i\}) = \chi_n(\{\mathbf{R}_\alpha\})\psi_n(\{\mathbf{R}_\alpha\}',\{\mathbf{r}_i\}) \ , \tag{2.3}$$

where $\{\mathbf{R}_\alpha\}'$ in the electronic function indicates that the dependence on the nuclear positions is parametric, that is, the electronic part is obtained for each set of fixed nuclear positions $\{\mathbf{R}_\alpha\}$. Consequently, equation (2.2) is separated in a nuclear part and an electronic part, which is written as

$$\hat{H}_{el}\psi_n(\{\mathbf{r}_i\},\{\mathbf{R}_\alpha\}') = \epsilon_n(\{\mathbf{R}_\alpha\})\psi_n(\{\mathbf{r}_i\},\{\mathbf{R}_\alpha\}') \ , \tag{2.4}$$

where the electronic Hamiltonian is given by $\hat{H}_{el} = \hat{T}_e + \hat{V}_{ee} + \hat{V}_{Ne}$. The total energy for the set of fixed positions of the nuclei includes the constant term of nuclear repulsion:

$$E_n(\{\mathbf{R}_\alpha\}) = \epsilon_n(\{\mathbf{R}_\alpha\}) + \sum_{\alpha=1}^{M}\sum_{\beta=\alpha+1}^{M}\frac{Z_\alpha Z_\beta}{|\mathbf{R}_\alpha - \mathbf{R}_\beta|} \ . \tag{2.5}$$

The nuclear equation is then given by

$$(\hat{T}_N + E_n(\{\mathbf{R}_\alpha\}))\chi_{nm}(\{\mathbf{R}_\alpha\}) = E_{nm}\chi_{nm}(\{\mathbf{R}_\alpha\}) \ , \tag{2.6}$$

that is, the energy $E_n(\{\mathbf{R}_\alpha\})$ defines a potential energy surface for the dynamics of the nuclei.

This approach has a good validity for a large variety of systems, but may fail in particular situations. For instance, such are the cases in which different electronic states are degenerate or near degenerate and strong coupling between electronic excitations and nuclear vibrations occur.[80] The properties that are investigated in Chapters 3 to 5 of this thesis can be studied based on the BO approximation.

2.2 Density functional theory

2.2.1 Hohenberg–Kohn theorems

Employing the N-electron wave function as the fundamental quantity to solve the electron system defined by the Schrödinger equation (2.4) can lead to high computational cost. In particular, in methods that include the necessary corrections to yield high quality results, the cost scales very rapidly with the number of atoms, which can make their application impractical for large systems. An alternative for these methods consists in basing the description of the many-electron system on the electron density. Such strategy is based on density functional theory (DFT), whose theoretical foundations are provided

by two theorems developed by Hohenberg and Kohn.[81] The first Hohenberg–Kohn (HK) theorem can be stated as: "For a system of an arbitrary number of electrons moving under the influence of an external potential, the same ground state electron density cannot be determined by two external potentials that differ by more than a simple additive constant." Therefore, there is a one-to-one correspondence of the ground state electron density and the external potential. The Hamiltonian of the system is the sum of purely electronic terms ($\hat{T}_e$ and $\hat{V}_{ee}$) and the term that originates from the external potential. Thus the external potential fixes the Hamiltonian, and it follows from the theorem that the ground state of the system is a unique functional of the ground state electron density. This legitimizes the use of the electron density as the fundamental quantity do describe the system.

The second HK theorem provides a variational approach to obtain the ground state electron density, by stating: "The energy functional of the electron density is minimized by the ground state electron density." That is, if the energy of the system is written as a functional of the electron density, $E[n(\mathbf{r})]$, as permitted by the first HK theorem, every trial electron density applied to the expression will result in an energy larger than or equal to the ground state energy, E_0:

$$E_0 \leq E[n(\mathbf{r})] \ , \tag{2.7}$$

where the equality holds only for the ground state electron density $n_0(\mathbf{r})$. Therefore, the correct ground state electron density can be obtained by minimization of the energy functional. Thus, combined with the constraint of the number of electrons in the system, the previous theorem requires that

$$\delta \left[E[n(\mathbf{r})] - \mu \left(\int n(\mathbf{r}) d^3r - N \right) \right] = 0 \ , \tag{2.8}$$

which yields

$$\mu = \frac{\delta F_{\mathrm{HK}}[n(\mathbf{r})]}{\delta n(\mathbf{r})} + v(\mathbf{r}), \tag{2.9}$$

where F_{HK} comes from $\hat{V}_{ee} + \hat{T}_e$, and is termed universal HK functional, as its form does not depend on the system under consideration. In the case of an external potential $v(\mathbf{r})$ describing ion-electron interactions ($\hat{V}_{Ne}$), it is obtained by

$$\hat{V}_{Ne}[n(\mathbf{r})] = \int \left(\sum_{\alpha=1}^{M} \frac{-Z_\alpha}{|\mathbf{R}_\alpha - \mathbf{r}|} \right) n(\mathbf{r}) d^3r = \int v(\mathbf{r}) n(\mathbf{r}) d^3r \ . \tag{2.10}$$

In principle, this method provides an exact solution to the electronic equation 2.4. However, an exact form for the universal HK functional is not known, mainly because of the difficulty to describe the kinetic energy. An approach to overcome this problem was developed by Kohn and Sham.

2.2.2 Kohn–Sham formalism

In the Kohn–Sham (KS) formalism,[82] the electron system is described in terms of an auxiliary system, a non-interacting electron gas with same ground state electron

density as the real system. In this approach, the HK functional is written as

$$F_{\mathrm{HK}}[n(\mathbf{r})] = \frac{1}{2}\int\int \frac{n(\mathbf{r})n(\mathbf{r}')}{|\mathbf{r}-\mathbf{r}'|}d^3r\ d^3r' + T_0[n(\mathbf{r})] + E_{\mathrm{xc}}[n(\mathbf{r})]\ . \tag{2.11}$$

The first term corresponds to the Coulomb inter-electronic repulsion, and the second term describes the kinetic energy of a non-interacting electron gas with same density as the real system. The last term, called exchange-correlation energy, contains contributions not yet considered by previous terms: (i) correction to the kinetic energy to describe the real interacting system; (ii) correction to the self-interaction energy that comes from the Coulomb term; (iii) exchange energy, a consequence of the exchange anti-symmetry required for the electron wave function; (iv) correlation energy, that accounts for the interdependence of electrons dynamics. The substitution of this expression in (2.9) gives

$$\mu = \frac{\delta T_0[n(\mathbf{r})]}{\delta n(\mathbf{r}))} + \int \frac{n(\mathbf{r}')}{|\mathbf{r}-\mathbf{r}'|}d^3r' + \frac{\delta E_{\mathrm{xc}}[n(\mathbf{r})]}{\delta n(\mathbf{r})} + v(\mathbf{r})\ , \tag{2.12}$$

which is the same equation that is obtained for a system of non-interacting electrons if it is under an effective potential

$$v_{\mathrm{ef}}(\mathbf{r}) = \int \frac{n(\mathbf{r}')}{|\mathbf{r}-\mathbf{r}'|}d^3r' + \frac{\delta E_{\mathrm{xc}}[n(\mathbf{r})]}{\delta n(\mathbf{r})} + v(\mathbf{r})\ , \tag{2.13}$$

where the second term on the right side is usually termed exchange-correlation potential, denoted by v_{xc}. Therefore, the ground state can be obtained from the solution of one-particle Schrödinger equation,

$$\left[-\frac{1}{2}\nabla^2_{\mathbf{r}} + v_{\mathrm{ef}}(\mathbf{r})\right]\phi_i(\mathbf{r}) = \epsilon_i\phi_i(\mathbf{r})\ . \tag{2.14}$$

The one-electron wave functions introduced by this method, $\phi_i(\mathbf{r})$, are termed KS orbitals and are used to construct the total wave function via a Slater determinant, and to obtain the ground state electron density via

$$n(\mathbf{r}) = \sum_{i=1}^{N}|\phi_i(\mathbf{r})|^2\ . \tag{2.15}$$

The total energy of the system, including the constant energy term of nuclei-nuclei interactions, can be written as

$$\begin{aligned} E_{tot} =& \sum_{i=1}^{N}\epsilon_i - \frac{1}{2}\iint \frac{n(\mathbf{r})n(\mathbf{r}')}{|\mathbf{r}-\mathbf{r}'|}d^3rd^3r' - \int v_{xc}(\mathbf{r})n(\mathbf{r})d^3r\ + \\ & E_{xc}[n(\mathbf{r})] + \sum_{\alpha=1}^{M}\sum_{\beta=\alpha+1}^{M}\frac{Z_\alpha Z_\beta}{|\mathbf{R}_\alpha-\mathbf{R}_\beta|}. \end{aligned} \tag{2.16}$$

Since the effective potential in the equation that must be solved to obtain the KS orbitals depends on the electron density, which in turn is obtained from KS orbitals, the solution of KS equations must be obtained self-consistently. Starting from a trial set of KS orbitals,

the electron density is obtained with (2.15) and consequently the effective potential can be calculated from (2.13), and is then used in (2.14) to obtain new KS orbitals, from which new electron density and effective potential can be obtained and restart the cycle. This cycle should be repeated until some previously defined convergence criterion is achieved, for instance, a variation of total energy smaller than a specified value.

2.2.3 Exchange-correlation functionals

2.2.3.1 Local and semi-local functionals

In principle, the KS scheme is able to provide an exact solution to a system of electrons under an arbitrary potential, but the exact form of E_{xc} is unknown. Therefore, approximations for this term, known as exchange-correlation functionals have been developed. The first level of approximation for E_{xc}, already proposed in the KS paper,[82] is the local density approximation (LDA), which considers only a dependence of the electron density at each point in space,

$$E_{\mathrm{xc}}^{\mathrm{LDA}} = \int d^3r n(\mathbf{r}) \epsilon_x^{\mathrm{LDA}}(n(\mathbf{r})) + \int d^3r n(\mathbf{r}) \epsilon_c^{\mathrm{LDA}}(n(\mathbf{r})) \ . \tag{2.17}$$

The expression for the exchange term $\epsilon_x^{\mathrm{LDA}}(n(\mathbf{r}))$ is obtained by applying the exact form of the Hartree–Fock (HF) exchange energy for a uniform electron distribution to each point in space,[83]

$$\epsilon_x^{\mathrm{LDA}}(n(\mathbf{r})) = -\frac{3}{4}\left(\frac{3n(\mathbf{r})}{\pi}\right)^{1/3} \ . \tag{2.18}$$

No exact expression is known for the correlation term, but asymptotic expressions for the homogeneous electron gas at the limits of high and low density are known.[84,85] Analytic expressions for the intermediate region are obtained by fitting numerical results of Monte Carlo calculations for the homogeneous electron gas,[86] such as the parametrizations proposed by Perdew and Zunger (PZ81)[87] and by Perdew and Wang (PW92).[88]

Another level of approximation for the exchange-correlation functionals is the generalized gradient approximation (GGA), in which a dependence of the functional on the gradient of electron density is also considered

$$E_{\mathrm{xc}}^{\mathrm{GGA}} = \int d^3r f(n(\mathbf{r}), |\nabla n(\mathbf{r})|) \ . \tag{2.19}$$

As with LDA functionals, there is no unique expression for GGA, and diverse functionals have been formulated. For instance, the functional proposed by Perdew and Wang (PW91)[89,90] was constructed in to order to satisfy several exact conditions. Later, Perdew, Burke and Ernzerhof simplified the derivation of the PW91 functional by satisfying only the energetically significant conditions, and formulated the PBE functional.[91] This functional is divided in two terms, the exchange and correlation functionals,

$$E_{\mathrm{xc}}^{\mathrm{PBE}} = E_{\mathrm{x}}^{\mathrm{PBE}} + E_{\mathrm{c}}^{\mathrm{PBE}} \ . \tag{2.20}$$

The PBE exchange functional has the form

$$E_{\mathrm{x}}^{\mathrm{PBE}} = \int d^3 r n(\mathbf{r}) \epsilon_x^{\mathrm{unif}}(n) F_X(n, |\nabla n|) \ , \tag{2.21}$$

where $\epsilon_x^{\mathrm{unif}}(n)$ is the exchange energy of the uniform electron gas given by (2.18). The PBE correlation functional is written as

$$E_{\mathrm{c}}^{\mathrm{PBE}} = \int d^3 r n(\mathbf{r}) [\epsilon_c^{\mathrm{PW}}(n) + H(n, |\nabla n|)] \ , \tag{2.22}$$

where $\epsilon_c^{\mathrm{PW}}(n)$ is the LDA–PW91 parametrization for the correlation energy.

2.2.3.2 Hybrid functionals

The calculation of band gaps of semiconductors and insulators from band structures of local and semi-local DFT presents difficulties, as band gaps are underestimated, and it has been observed that more realistic band gaps can be obtained with the use of hybrid functionals.[92] These exchange-correlation functionals contain a part of the exact Hartree-Fock (HF) exchange term, which is given by[83]

$$E_x^{\mathrm{HF}} = -\frac{1}{2} \sum_i \sum_j \int d^3 r \int d^3 r' \phi_i^*(\mathbf{r}) \phi_i(\mathbf{r}') \frac{1}{|\mathbf{r} - \mathbf{r}'|} \phi_j(\mathbf{r}) \phi_j^*(\mathbf{r}') \ , \tag{2.23}$$

where the sums run over occupied orbitals. This type of functional has its basis on the PBE0 functional,[93] which keeps the correlation term of the PBE functional and mixes the PBE exchange term with HF exchange in a 3:1 proportion,

$$E_{xc}^{\mathrm{PBE0}} = \frac{1}{4} E_x^{\mathrm{HF}} + \frac{3}{4} E_x^{\mathrm{PBE}} + E_c^{\mathrm{PBE}} \ . \tag{2.24}$$

This mixing proportion was derived based on perturbation theory from the adiabatic connection theorem, to optimize results for atomization energies of molecules.[93] An important drawback of the PBE0 functional is the large computational cost to evaluate the exchange term. To reduce this limitation, it has been observed that the long range contributions of PBE and HF exchange are similar and have low numerical values.[94] Based on that, Heyd, Scuseria and Ernzerhof proposed a range separated hybrid functional (HSE06) in which the Coulomb operator of the exchange term is separated in short range (SR) and long range (LR), and the LR exchange takes only PBE exchange. The range separation is written as

$$\frac{1}{r} = \frac{\mathrm{erf}(\omega r)}{r} + \frac{\mathrm{erfc}(\omega r)}{r} \ , \tag{2.25}$$

where $\mathrm{erf}(x)$ is the error function,

$$\mathrm{erf}(x) = \frac{1}{\sqrt{\pi}} \int_{-x}^{x} e^{-u^2} du \ , \tag{2.26}$$

which is equal to 0 for $x = 0$ and goes to 1 for $x \to \infty$, and $\mathrm{erfc}(x)$ is the complementary error function ($\mathrm{erfc}(x) = 1 - \mathrm{erf}(x)$). The first term on the right side of equation 2.25

composes the SR term, and the second term composes the LR term, with ω as a range separation parameter. Thus, the HSE06 exchange-correlation functional is

$$E_{xc}^{\mathrm{HSE06}} = \frac{1}{4}E_{x,\mathrm{SR}}^{\mathrm{HF}} + \frac{3}{4}E_{x,\mathrm{SR}}^{\mathrm{PBE}} + E_{x,\mathrm{LR}}^{\mathrm{PBE}} + E_{c}^{\mathrm{PBE}} \ . \tag{2.27}$$

It is readily noted that for $\omega = 0$ the PBE0 functional is recovered, and for $\omega \to \infty$ the PBE functional is obtained. Tests performed with different values for ω have shown that $\omega = 0.11$ bohr$^{-1} = 0.206\,\text{Å}^{-1}$ provides a good compromise between computational cost (time and less convergence problems) and accuracy of results for properties of atoms, molecules and solids, such as ionization potentials, electron affinities, bond lengths, lattice parameters, and band gaps.[95]

2.2.4 van der Waals Corrections

Standard local and semi-local exchange correlation functionals can also fail to provide a good description of long range electron correlation, which is related to vdW dispersion interactions. Because of that, the strength of binding is usually underestimated in systems in which these forces are important, such as molecular solids, or crystals with weakly bound layers, as in the case of TMDs.[96,97] To overcome this problem, some methods have been developed in order to improve the description of weak vdW within DFT calculations. In particular, a class of methods is based on the notion that these interactions have no significant direct effects on the ground state electron density, so that only a correction to the converged DFT total energy is added, keeping the electron density unchanged,

$$E = E_{\mathrm{tot}} + E_{\mathrm{vdW}} \ . \tag{2.28}$$

One of these methods is the D3 method developed by Grimme *et al.*,[98] in which the dispersion energy is composed of two- and three-body interactions terms for the atoms,

$$E_{\mathrm{vdW}} = -\sum_{n=6,8,10}\left[\sum_{\alpha}\sum_{\beta<\alpha} s_n \frac{f_{a,n}(R_{\alpha\beta})C_n^{\alpha\beta}}{R_{\alpha\beta}^n}\right] - \sum_{\alpha}\sum_{\beta<\alpha}\sum_{\gamma<\beta} f_{a,3}(R_{\alpha\beta\gamma})E^{\alpha\beta\gamma} \ , \tag{2.29}$$

where $R_{\alpha\beta}$ is the distance between atoms α and β, and in the three-body term, $R_{\alpha\beta\gamma}$ is the geometric mean of $R_{\alpha\beta}$, $R_{\beta\gamma}$ and $R_{\gamma\alpha}$, and the term $E^{\alpha\beta\gamma}$ depends on the distances between atoms and on the angles determined by lines joining these atoms.

It was shown that including the terms with $n > 8$ in the D3 correction can cause instabilities, without considerably enhancing the quality of results for common systems.[98] Beyond that, the inclusion of the three-body term can worsen the accuracy of lattice parameter results.[99] Therefore, in the implementation employed here, only the two-body terms with $n = 6$ and $n = 8$ are included. Furthermore, $f_{a,n}$ are damping functions, employed to avoid divergences for small bond lengths, and are given by

$$f_{a,n}(R_{\alpha\beta}) = \frac{1}{1 + 6(R_{\alpha\beta}/(s_{r,n}R_0^{\alpha\beta}))^{-\mu_n}} \ , \tag{2.30}$$

where $R_0^{\alpha\beta}$ are fixed for each pair of atoms between H and Pu, and the parameters $s_{r,8}$, μ_6, and μ_8 are fixed,[98] and $s_{r,6}$, as well as s_6 and s_8 are adjusted depending on the exchange correlation functional employed.[98] The $C_n^{\alpha\beta}$ coefficients, which determine the magnitude of the interactions, are determined both by the chemical species and the chemical environment within the material being calculated. Several reference coefficient values of C_6 for each chemical species were obtained for different hydride molecules. Then, the chemical environment is taken into account by geometrical considerations, as the $C_n^{\alpha\beta}$ coefficients are obtained by a weighted average of these reference values. In this average, the weights are proportional to the similarity between the effective coordination numbers of the respective atoms in the reference molecules and in the system being calculated.[98]

2.3 Time-dependent density functional theory

2.3.1 Runge–Gross theorem and time-dependent Kohn–Sham formalism

The study of dynamic processes, such as the transfer of charge carriers in semiconductor junctions, is inherently time-dependent and therefore, beyond the scope of DFT simulations. Considering the success of DFT to address several physical properties of materials and its computational efficiency, a time-dependent counterpart of DFT is a promising route to describe such phenomena. The theoretical foundations that allow the use of the density as the fundamental variable to describe time-dependent systems are provided by the Runge–Gross (RG) theorem,[100] an analog of HK theorem. The RG theorem can be stated as "Two particle densities $n(\mathbf{r})$ and $n'(\mathbf{r})$ that evolve from the same initial state are always different if they evolve under the influence of two different potentials (assumed to be expandable in a Taylor series about the initial time) that differ by more than a purely time-dependent function". Therefore, there is a one-to-one mapping between the time-dependent external potential and the particle density, and it is possible to use the density as the fundamental quantity to describe the system. Based on these results, an additional theorem provides a time-dependent analog of the KS formalism,[100] where the time-dependent density is obtained from

$$n(\mathbf{r},t) = \sum_{i=1}^{N} |\phi_i(\mathbf{r},t)|^2 \ , \tag{2.31}$$

and the orbitals $\phi_i(\mathbf{r},t)$ are solutions of

$$\left[-\frac{1}{2}\nabla_{\mathbf{r}}^2 + v_{eff}(\mathbf{r},t)\right]\phi_i(\mathbf{r},t) = i\frac{\partial\phi_i(\mathbf{r},t)}{\partial t} \ , \tag{2.32}$$

with effective potential given by

$$v_{eff}(\mathbf{r},t) = \int \frac{n(\mathbf{r}',t)}{|\mathbf{r}-\mathbf{r}'|}d^3r' + v_{\mathrm{xc}}[n](\mathbf{r},t) + v(\mathbf{r},t) \ . \tag{2.33}$$

In this scheme, it is usual to adopt the adiabatic local density approximation (ALDA) for the exchange-correlation potential $v_{\mathrm{xc}}[n](\mathbf{r},t)$. This approach employs the functional form of LDA functional for the time-dependent density, i.e. $v_{\mathrm{xc}}^{\mathrm{ALDA}}[n](\mathbf{r},t) = v_{\mathrm{xc}}^{\mathrm{LDA}}[n(\mathbf{r},t)]$.[101]

The RG theorem can be extended to multi-component systems,[102] and because of that, it can be applied to the many body state $\Psi(\{\mathbf{R}_\alpha\},\{\mathbf{r}_i\},t)$ of N electron and M nuclei, where there is a one-to-one mapping between the external potentials and the ionic and electronic densities. This allows to treat systems with the coupling of nuclear and electronic motions, beyond the BO approximation. Similarly to the case of the electron system, a set of coupled time-dependent KS equations analogous to the time-independent case are derived for coupled electron-nucleus system[101]

$$\left[-\frac{1}{2}\nabla^2_{\mathbf{r}} + v_s(\mathbf{r},t)\right]\phi_i(\mathbf{r},t) = i\frac{\partial\phi_i(\mathbf{r},t)}{\partial t} \ , \tag{2.34}$$

$$\left[-\frac{1}{2}\nabla^2_{\mathbf{R}} + V^\alpha_s(\mathbf{R},t)\right]\chi_\alpha(\mathbf{R},t) = i\frac{\partial\chi_\alpha(\mathbf{R},t)}{\partial t} \ , \tag{2.35}$$

where the effective potentials in the electronic and nuclear equations, $v_s(\mathbf{r},t)$ and $V^\alpha_s(\mathbf{R},t)$, respectively, are given by

$$v_s(\mathbf{r},t) = \int \frac{n(\mathbf{r}',t)}{|\mathbf{r}-\mathbf{r}'|}d^3r' - \sum_{\alpha=1}^{M}\int \frac{Z_\alpha n_\alpha(\mathbf{R},t)}{|\mathbf{r}-\mathbf{R}|}d^3R + v_{\rm xc}[n](\mathbf{r},t) + v_{\rm ext}(\mathbf{r},t) \ , \tag{2.36}$$

$$\begin{aligned} V^\alpha_s(\mathbf{R},t) = Z_\alpha \sum_{\beta=1}^{M}\int \frac{Z_\beta n_\beta(\mathbf{R}',t)}{|\mathbf{R}-\mathbf{R}'|}d^3R' - Z_\alpha\int\frac{n(\mathbf{r},t)}{|\mathbf{R}-\mathbf{r}|}d^3r + \\ V^\alpha_{\rm xc}[n_\alpha](\mathbf{R},t) \ + V^\alpha_{\rm ext}(\mathbf{R},t) \ , \end{aligned} \tag{2.37}$$

where the external potentials $v_{\rm ext}(\mathbf{r},t)$ and $V^\alpha_{\rm ext}(\mathbf{r},t)$ come from fields with source external to the system of electron and ions. In this formalism, the exchange-correlation functionals $v_{\rm xc}[n](\mathbf{r},t)$ and $V^\alpha_{\rm xc}[n_\alpha](\mathbf{R},t)$ are defined by the previous equations, and the potentials are functionals of the nuclear and electronic densities, which are given by

$$n(\mathbf{r},t) = \sum_{i=1}^{N}|\phi_i(\mathbf{r},t)|^2 \ , \tag{2.38}$$

$$n_\alpha(\mathbf{R},t) = \sum_{\alpha=1}^{M}|\chi_\alpha(\mathbf{R},t)|^2 \ . \tag{2.39}$$

2.3.2 Ehrenfest dynamics

The explicit treatment of the many-body system with the formalism defined by equations (2.34)-(2.39) can be very difficult, both in terms of computational effort and the definition of reliable formulations for exchange and correlation energy functionals for nucleus-electron and nucleus-nucleus. To simplify the task, a widely used approach consists in treating the nuclear motion classically.[101] Applying Ehrenfest theorem to equation 2.35, the classical trajectory of the α-th nucleus,

$$\mathbf{R}^{\rm cl}_\alpha(t) = \int \mathbf{R}n_\alpha(\mathbf{R},t)d^3R \ , \tag{2.40}$$

satisfies the equation of motion

$$M_\alpha \frac{d^2\mathbf{R}_\alpha^{\mathrm{cl}}(t)}{dt^2} = \mathbf{F}_\alpha(t) \tag{2.41}$$

with force given by

$$\mathbf{F}_\alpha(t) = -\int \chi_\alpha^*(\mathbf{R},t)\nabla_{\mathbf{R}} V_s^\alpha(\mathbf{R},t)\chi_\alpha(\mathbf{R},t)d^3R \ . \tag{2.42}$$

A natural approximation for the nuclear densities is to assume that the nuclei are localized at the classical trajectory $\mathbf{R}_\alpha^{\mathrm{cl}}(t)$, and therefore the density can be written as

$$n_\alpha(\mathbf{R},t) = \delta(\mathbf{R} - \mathbf{R}_\alpha^{\mathrm{cl}}(t)) \ . \tag{2.43}$$

Within this approximation, it is also reasonable to represent the potential $V_{\mathrm{xc}}^\alpha[n_\alpha](\mathbf{R},t)$ only with a self-interaction term, that is, neglecting contributions from correlation and reducing the exchange energy only to the self-exchange contribution, which corrects the self-interaction in the Coulomb term.[101] Therefore, the equation of motion for the α-th nucleus is written as

$$M_\alpha \frac{d^2\mathbf{R}_\alpha^{\mathrm{cl}}(t)}{dt^2} = -\nabla_{\mathbf{R}_\alpha^{\mathrm{cl}}}\left[Z_\alpha \sum_{\substack{\beta=1 \\ \beta\neq\alpha}}^{M} \frac{Z_\beta}{|\mathbf{R}_\alpha^{\mathrm{cl}} - \mathbf{R}_\beta^{\mathrm{cl}}|} - Z_\alpha \int \frac{n(\mathbf{r},t)}{|\mathbf{R}_\alpha^{\mathrm{cl}} - \mathbf{r}|} d^3r + V_{\mathrm{ext}}^\alpha(\mathbf{R}_\alpha^{\mathrm{cl}},t)\right] , \tag{2.44}$$

and the electronic time-dependent KS equation can be simplified to

$$\begin{aligned} i\frac{\partial\phi_i(\mathbf{r},t)}{\partial t} = & \Bigg[-\frac{1}{2}\nabla_{\mathbf{r}}^2 + \int \frac{n(\mathbf{r}',t)}{|\mathbf{r}-\mathbf{r}'|} d^3r' \sum_{\alpha=1}^{M} \int \frac{Z_\alpha}{|\mathbf{r} - \mathbf{R}_\alpha^{\mathrm{cl}}(t)|} + \\ & v_{\mathrm{xc}}[n](\mathbf{r},t) + v_{\mathrm{ext}}(\mathbf{r},t)\Bigg]\phi_i(\mathbf{r},t) \ . \end{aligned} \tag{2.45}$$

Therefore, equations (2.44) and (2.45) describe the time evolution of coupled electron-nucleus system. The electronic part is described within the TDDFT framework, and therefore its time evolution depends on the initial state and on the total potential, which includes a term to account for the Coulomb interaction with the moving nuclei. The method for the solution of the time-dependent KS equations are related to the adopted basis set, and because of that it is described in more detail in Section 2.5.2. The time dependent KS equations must be solved simultaneously with the Newton equations that describe the nuclear motion. This is in contrast with a dynamics based on the BO approximation, because the electronic ground state is not obtained for the updated positions of the nuclei. The approach employed in this thesis considers KS orbitals with fixed occupation during the simulation, and therefore does not account for electron transitions. Such limitation is not critical for a description of excited states if the initial stages after the excitation are simulated.

The initial state for a TDDFT simulation is determined by the solution of the KS equations at a given configuration of the nuclei, yielding the initial configuration for the

time-dependent KS orbitals $\{\phi_i(\mathbf{r},0)\}$. Besides the set of initial nuclei positions $\{\mathbf{R}_\alpha(0)\}$, this configuration is also fixed by the initial nuclei velocities $\{\mathbf{V}_\alpha(0)\}$, that determine the ionic temperature. At this point, electronic excitations can be modeled by changing the occupation of ground state KS orbitals that correspond to the excitation. The time-evolution of $\{\phi_i(\mathbf{r},t)\}$ is then obtained by the solution of equation (2.45), which yields an updated electron density for $t+\Delta t$, where the parameter Δt fixes the length of the time step in the simulation. Consequently, an updated set of forces $\{\mathbf{F}_\alpha(t)\}$ defined by equation (2.44) is obtained and with the updated forces, molecular dynamics (MD) can be applied to $\{\mathbf{R}_\alpha(t)\}$ and $\{\mathbf{V}_\alpha(t)\}$. Employing the velocity Verlet algorithm, this is done according to the equations[103]

$$\mathbf{R}_\alpha(t+\Delta t) = \mathbf{R}_\alpha(t) + \mathbf{V}_\alpha(t)\Delta t + \frac{1}{2}\frac{\mathbf{F}_\alpha(t)}{M_\alpha}\Delta t^2 \ , \tag{2.46}$$

$$\mathbf{V}_\alpha(t+\Delta t) = \mathbf{V}_\alpha(t) + \frac{\mathbf{F}_\alpha(t)+\mathbf{F}_\alpha(t+\Delta t)}{2M_\alpha}\Delta t \ . \tag{2.47}$$

The updated set of nuclei positions define a new KS hamiltonian to perform the time evolution of $\{\phi_i(\mathbf{r},t)\}$, restarting the cycle, which can be repeated to extend the simulated time. In practice, self-consistent operations are performed to accept the updated orbitals $\{\phi_i(\mathbf{r},t+\Delta t)\}$. In these operations, the time propagation is iterated for a given time step until a defined criterion is satisfied, for instance, a small variation of the total energy as in the KS cycle. This self-consistent loop is not related to the self-consistency in the solution of the KS equations, since the updated orbitals are not eigenfunctions of the updated hamiltonian, and the procedure is employed to improve the stability of the simulation.[103]

2.4 Periodic systems

All simulations performed within this work employed periodic boundary conditions, based on the periodicity of crystal solids. In crystals, a lattice is defined by a set of points that are equivalent under translations defined by $\mathbf{T} = n_1\mathbf{a}_1 + n_2\mathbf{a}_2 + n_3\mathbf{a}_3$, where n_i's are integers and $\mathbf{a}_i$ are called lattice vectors. The possible symmetry operations in three-dimensional space restricts the number of $\mathbf{a}_i$ vectors sets that can be used to define lattices, and 14 types of lattices can be obtained, which are called the Bravais lattices.[104] A crystal structure is completely defined by associating to each point of the Bravais lattice a set of atoms, called basis, such that the position of each atom in the basis can be written as, $\mathbf{u}_j = \alpha_j\mathbf{a}_1 + \beta_j\mathbf{a}_2 + \gamma_j\mathbf{a}_3$, where $0 \leq \alpha_j, \beta_j, \gamma_j \leq 1$, and these coordinates are referred to as direct (or relative) coordinates. The crystal is then generated by filling the three-dimensional space with repeating units, or cells, which can be defined in more than one way, and those with the least volume, which contain only one lattice point, are called the primitive or unit cells. Of the possible unit cells, the Wigner-Seitz cell is obtained by the following procedure: define segments that connect a lattice point to the

nearest lattice points and build planes normal to each of the segments that cut them in their midpoints; the volume enclosed by these planes is the Wigner-Seitz cell. Periodic boundary conditions were employed in all calculations discussed in this thesis. Therefore, to model systems which lack periodicity in one or more dimensions, such as monolayers and nanoflakes, large cells were employed to ensure vacuum distances of 15 Å between periodic images, in order to minimize the effect of unwanted interactions.

In the study of crystal solids, the concept of reciprocal lattice has great importance, for example to investigate crystal structures via X-ray diffraction or in the description of the electronic states in the crystal.[105] The reciprocal lattice is defined by a set of vectors $\mathbf{k}$ which define plane waves with the same periodicity of the Bravais lattice, that is, $e^{i\mathbf{k}\cdot(\mathbf{r}+\mathbf{T})} = e^{i\mathbf{k}\cdot\mathbf{r}}$. This condition is satisfied if the $\mathbf{k}$ vectors are written as linear combinations of reciprocal lattice basis vectors $\mathbf{b}_i$, given by

$$\mathbf{b}_1 = 2\pi\frac{\mathbf{a}_2 \times \mathbf{a}_3}{\mathbf{a}_1 \cdot \mathbf{a}_2 \times \mathbf{a}_3} \ , \quad \mathbf{b}_2 = 2\pi\frac{\mathbf{a}_3 \times \mathbf{a}_1}{\mathbf{a}_1 \cdot \mathbf{a}_2 \times \mathbf{a}_3} \ , \quad \mathbf{b}_3 = 2\pi\frac{\mathbf{a}_1 \times \mathbf{a}_2}{\mathbf{a}_1 \cdot \mathbf{a}_2 \times \mathbf{a}_3} \ . \tag{2.48}$$

In the reciprocal lattice, the Wigner-Seitz cell is often termed the First Brillouin Zone (FBZ), and the $\mathbf{k}$'s contained within this region are the essential wavevectors for the description of electronic states.

The use of the wavevectors $\mathbf{k}$ as quantum numbers for the electronic states in crystal solids emerges as an important consequence of the periodicity of the lattice, since the potential exerted on the electrons by the ion lattice has the same periodicity. According to Bloch's theorem, the wavefunctions of electrons under a periodic potential ($V(\mathbf{r}+\mathbf{T}) = V(\mathbf{r})$) can be written as,[104,105]

$$\psi_{i\mathbf{k}}(\mathbf{r}) = e^{i\mathbf{k}\cdot\mathbf{r}} u_{i\mathbf{k}}(\mathbf{r}) \ , \tag{2.49}$$

where $u_{\mathbf{k}}(\mathbf{r})$ is a function with the periodicity of the Bravais lattice. This form can be evidently employed for KS orbitals of periodic systems. The properties of reciprocal lattice vectors allow $\mathbf{k}$ to be confined to the FBZ, since any vector in the reciprocal space can be written as a sum of a vector in the FBZ plus a reciprocal lattice vector. Because of the dependence of the electronic states on the reciprocal space vectors $\mathbf{k}$, the evaluation of many quantities require integration in the FBZ. For instance, the electronic density is given by

$$n(\mathbf{r}) = \frac{1}{\Omega_{\mathrm{FBZ}}} \int_{\mathrm{FBZ}} \left(\sum_i |\phi_{i\mathbf{k}}(\mathbf{r})|^2 \right) d^3k \ , \tag{2.50}$$

where Ω_{FBZ} indicates the volume of FBZ and the sum runs over occupied KS orbitals. To perform these integrations numerically, a mesh of points is selected to sample the FBZ, and an appropriate choice for the density of this mesh is based on tests with increasing density until ensuring that the FBZ is well represented, typically called convergence tests.

2.5 Basis sets

2.5.1 Plane-waves

The application of (2.49) to the KS orbitals typically employs the expansion of the functions $u_{i,\mathbf{k}}(\mathbf{r})$ as a linear combination of a set of basis functions,

$$u_{i\mathbf{k}}(\mathbf{r}) = \sum_{p=1}^{B} c_{i\mathbf{k}p}\chi_p(\mathbf{r}) \ , \tag{2.51}$$

and the solution of the KS equations, both in static and time-dependent frameworks is based on determining the $c_{i\mathbf{k}p}$ coefficients. The choice of the basis set is an important aspect for calculations, because the properties of each set can lead to benefits for their application, depending on factors such as the features of the system under investigation and the computational cost. Given the periodicity of the systems, a plane-wave basis with wave vectors given by lattice vectors of the reciprocal space, $\mathbf{G}$, is a natural choice. In this approach, the KS orbitals are written as

$$\phi_{i\mathbf{k}}(\mathbf{r}) = \sum_{\frac{|\mathbf{G}+\mathbf{k}|^2}{2}<E_c} c_{\mathbf{k}}(\mathbf{G})e^{i(\mathbf{k}+\mathbf{G})\cdot\mathbf{r}} \ , \tag{2.52}$$

where the number of plane waves in the expansion is limited by the cutoff energy E_c, a parameter which specifies the maximum kinetic energy of the plane waves. This truncation at plane-waves at smaller wave vectors is based on the smooth variation of the wave function and electron density. In practice, an appropriate choice for E_c is based on convergence tests, in which increasing E_c, and consequently the number of plane-waves in the basis, is a systematic way to improve the quality of the basis. Including a very large number of plane-waves in the basis can lead to excessively large computational cost, and therefore, one of the main drawbacks in the use of this basis is due to the rapid oscillations of the electron wave functions near the atomic nuclei, which would imply the need of a very large number of plane waves to accurately describe these functions. Some strategies have been develop to overcome this difficulty, and the calculations with plane-wave basis set in this thesis employed the projector augmented-wave method, described in Section 2.6.

2.5.2 Linear combination of atomic orbitals

The use of the basis set expansion allows to change the KS equation (2.14) into a matricial form, i.e.,

$$H_{\mathrm{KS}} \sum_{p=1}^{B} c_{np}\chi_p(\mathbf{r}) = \epsilon_n \sum_{p=1}^{B} c_{np}\chi_p(\mathbf{r}) \ , \tag{2.53}$$

$$\sum_{p=1}^{B} \left(\int \chi_q^*(\mathbf{r}) H_{\mathrm{KS}} \chi_p(\mathbf{r}) d^3r \right) c_{np} = \epsilon_n \sum_{p=1}^{B} \left(\int \chi_q^*(\mathbf{r})\chi_p(\mathbf{r}) d^3r \right) c_{np} \ , \tag{2.54}$$

$$\Rightarrow \mathbf{H}\mathbf{c}_n = \epsilon_n \mathbf{S}\mathbf{c}_n \ , \tag{2.55}$$

where **H** and **S** are the hamiltonian and overlap matrices, respectively, with elements given by

$$H_{qp} = \int \varphi_q^*(\mathbf{r}) H_{\mathrm{KS}} \varphi_p(\mathbf{r}) d^3r \;\; ; \;\; S_{qp} = \int \varphi_q^*(\mathbf{r}) \varphi_p(\mathbf{r}) d^3r \; . \tag{2.56}$$

If these matrices are sparse, the computational cost of calculations can be decreased, and such property is fundamental, for instance, to develop methods whose cost scales linearly with the number of atoms.[106] The sparsity of the hamiltonian and overlap matrices can be ensured by using a basis set of confined functions, which have zero value beyond a cutoff radius r_c. This feature is present in the linear combination of atomic orbitals (LCAO) basis set, in which the basis functions are defined by a product of a radial function and a spherical harmonic,

$$\chi_{\alpha lmp}(\mathbf{r}) = \varphi_{\alpha lp}(r_\alpha) Y_{lm}(\hat{\mathbf{r}}_\alpha) \; , \text{ for } r < r_c \; , \tag{2.57}$$

where α denotes the atom, with $\mathbf{r}_\alpha = \mathbf{r} - \mathbf{R}_\alpha$, and l,m are the angular momentum labels. The label p indicates that several functions can be included for the same angular momentum, usually termed multiple-ζ basis.

In the LCAO basis that was employed in this thesis,[106] the minimal basis set (single-ζ) has a single radial function for each angular momentum which are obtained by the solution of a radial Schrödinger-like equation for the atom,

$$\left(-\frac{1}{2r} \frac{d^2}{dr^2} r + V_l(r) \right) \varphi_l^{1\zeta}(r) = (\epsilon_l + \delta\epsilon_l) \varphi_l^{1\zeta}(r) \; , \tag{2.58}$$

where α and p labels were omitted for simplicity. The energy shift $\delta\epsilon_l$ is defined to place the first node of the radial function at the chosen r_c, and usually this parameter is fixed as the same for all atomic species and angular momenta. The scheme adopted to increase the basis set size defines a split radius r_s, and a function that has the same tail of $\varphi_l^{1\zeta}(r)$ beyond r_s and is a polynomial $R^{2\zeta}(r) = r_s(a_l - b_l r^2)$ for $r < r_s$, with a_l and b_l determined to ensure continuity and differentiability at r_s. This split radius is set based on a the norm of $\varphi_l^{1\zeta}(r)$ for $r > r_s$, and therefore this split norm is an additional parameter to control the basis set. Then, the second orbital, which is confined within r_s, is defined as $\varphi_l^{2\zeta}(r) = A(\varphi_l^{1\zeta}(r) - R^{2\zeta}(r))$, where A is a normalization constant. Because of the formation of bonds and consequent deformation of wave functions, better results can be obtained by including polarization orbitals in the basis set. This is done by adding a shell with angular momentum $l + 1$ to polarize the last occupied orbitals (angular momentum l). The radial functions are obtained by solving a Schrödinger equation.[106] Therefore, the LCAO basis set is controlled by the choice of the energy shift and split-norm parameters, which define r_c and r_s, respectively, as well the number of basis orbitals, and the quality of results is improved with a larger basis set.

2.5.2.1 Solution of the time-dependent Kohn–Sham Equations

With the LCAO basis, the time-dependent KS equation (2.45) leads to

$$i\frac{\partial \mathbf{c}_i}{\partial t} = \mathbf{S}^{-1}\mathbf{H}\mathbf{c}_i \ , \tag{2.59}$$

where $\mathbf{H}$ corresponds to the the hamiltonian defined by the right side of equation (2.45). With a small time step Δt, the solution of this equation is given by[103]

$$\mathbf{c}_i(t+\Delta t) = \exp\{-i\Delta t\mathbf{S}^{-1}(t)\mathbf{H}(t)\}\mathbf{c}_i(t) \ . \tag{2.60}$$

Numerically, the exponential propagator can be approximated with the Crank–Nicholson method, and the equation is written in matricial form

$$[I + (i\Delta t/2)\mathbf{S}^{-1}(t)\mathbf{H}(t)]\mathbf{c}_n(t+\Delta t) = [I - (i\Delta t/2)\mathbf{S}^{-1}(t)\mathbf{H}(t)]\mathbf{c}_n(t) \ . \tag{2.61}$$

All TDDFT simulations discussed in this thesis employed this scheme to solve the time-dependent KS equations.

2.6 Projector augmented wave method

Strategies to enable an efficient use of plane-wave basis set have been developed based on the separation between core and valence regions, since wave functions vary more smoothly far from the nuclei. This distinction is based on contrasting features of the two types of electronic states: (i) the densities of core electrons are concentrated near the nuclei, but valence electronic density is spread to more external regions; (ii) the energy scales of the core and valence states can be clearly distinguished; (iii) core electrons are practically unaffected by the chemical environment or external perturbations, but valence electrons are responsible for the formation of chemical bonds.[107] Therefore, different approaches can be used to describe these two types of spatial regions, keeping the accuracy in the description of the wave function without the need for a high computational cost for the core regions. In the projector augmented-wave (PAW) method proposed by Blöchl,[107] the plane-waves expansion is simplified by the introduction of pseudofunctions, on which a linear transformation is applied to obtain the true orbitals. This linear transformation acts on spheres centered on each atom, termed augmentation regions, and therefore, the pseudofunctions match the real orbitals in the space outside the augmentation regions, termed intersticial region.

Within the augmentation regions, each true orbital $\phi(\mathbf{r})$ is obtained by a linear combination of partial waves $\psi_i(\mathbf{r})$, which can naturally be chosen as solutions of the Schrödinger equation for the isolated atom. Here, i denotes a simplified label for the atomic site, angular momentum, and the different states which share the same atomic site and the same angular momentum. For each partial wave, a pseudo-partial wave $\tilde{\psi}_i(\mathbf{r})$

is defined, such that it matches $\psi_i(\mathbf{r})$ in the intersticial region and has a smooth behavior within the augmentation region. As readily noted from the definitions, the true orbital within the augmentation regions is a linear combination of the pseudo-partial waves $\tilde{\psi}_i(\mathbf{r})$ with the same coefficients of the linear combination of partial waves $\psi_i(\mathbf{r})$. Therefore, each orbital $\phi(\mathbf{r})$ can be related to a pseudo-orbital $\tilde{\phi}(\mathbf{r})$ through

$$\phi(\mathbf{r}) = \tilde{\phi}(\mathbf{r}) - \sum_i c_i \tilde{\psi}_i(\mathbf{r}) + \sum_i c_i \psi_i(\mathbf{r}) \ . \tag{2.62}$$

To determine the c_i coefficients, projector functions $\tilde{p}_i(\mathbf{r})$ are defined, one for each $\tilde{\psi}_i(\mathbf{r})$ to satisfy the relation

$$\int \tilde{p}_i^*(\mathbf{r}) \tilde{\psi}_j(\mathbf{r}) d^3r = \delta_{ij} \ \text{, within the augmentation region} \ , \tag{2.63}$$

and as a result the coefficients are given by

$$c_i = \int \tilde{p}_i^*(\mathbf{r}) \phi(\mathbf{r}) d^3r \ . \tag{2.64}$$

Therefore, the relation between the orbital and pseudo-orbital is written as

$$\phi(\mathbf{r}) = \tilde{\phi}(\mathbf{r}) + \sum_i \left[\left(\int \tilde{p}_i^*(\mathbf{r}') \phi(\mathbf{r}') d^3r' \right) \left(\psi(\mathbf{r}) - \tilde{\psi}(\mathbf{r}) \right) \right] \ , \tag{2.65}$$

and this relation defines the linear transformation that maps the pseudo-orbitals to the real orbitals. Since the $\psi(\mathbf{r})$ and $\tilde{\phi}(\mathbf{r})$ are identical in the interstitial region, the transformation acts only within the augmentation regions. In the PAW method, the pseudo-orbitals $\tilde{\phi}(\mathbf{r})$ are the variational quantities which are expanded in the plane-wave basis, which requires smaller basis than the true orbitals due to the smoothness of the pseudo-orbitals. The states of core electrons are described in a similar way, and core orbitals are given by

$$\phi^c(\mathbf{r}) = \tilde{\phi}^c(\mathbf{r}) + \psi^c(\mathbf{r}) - \tilde{\psi}^c(\mathbf{r}) \ , \tag{2.66}$$

where no projector functions must be defined and the coefficients in the expansion are equal to 1. In the frozen core approximation, the states of core electrons are fixed to the isolated atoms for which the orbitals were generated.

2.7 Computational implementation

Several computational packages capable of performing DFT calculations are currently available and among their differences, those related to the approach for the solution of the KS equations can be highlighted, such as the employed basis set and the treatment of core electrons. The largest part of this thesis addresses static properties of materials within DFT, which correspond to the results discussed in Chapters 3, 4, and 5. For that, the calculations were performed with the Vienna *Ab initio* Simulation Package (VASP),[108–110] which is among the most popular and reliable DFT codes. In VASP, the KS

orbitals are expanded in a plane-wave basis set and the KS equations are solved with the PAW method within the frozen core approximation, for which optimized PAW projectors are available. The calculations with VASP employed the GGA-PBE exchange-correlation functional and D3 vdW correction (except where indicated otherwise). A set of calculations was performed with the hybrid functional HSE06 to obtain the band gaps discussed in Chapter 4. Due to the variety of systems investigated and to optimize computational efficiency along with accuracy, crucial parameters of the calculations, such as the energy cutoff of the plane-wave basis and the **k**-points mesh for integrations in the BZ, were defined separately for each part of the study, specifically for each chapter from 3 to 5. The detailed computational parameters are provided in Appendix A.

The last part of the thesis, presented in Chapter 6, addresses the dynamics of charge carriers in excited states employing TDDFT. The results discussed in this chapter were obtained with the code Spanish Initiative for Electronic Structure with Thousands of Atoms (SIESTA),[106] and The Time Dependent *Ab Initio* Package (TDAP),[103] an implementation of TDDFT coupled with molecular dynamics built on top of SIESTA, was employed to perform the TDDFT simulations. SIESTA employs a LCAO basis set for the KS orbitals, with the features discussed in Section 2.5.2, and these calculations employed the LDA-PZ81 exchange-correlation functional, which provides a satisfactory description of the structural properties of the studied systems. Further details on the employed basis set, and other computational parameters are given in Appendix A.

3 SIZE EFFECTS ON THE PROPERTIES OF TWO-DIMENSIONAL $MoSe_2$

Because of the immense potential of TMDs nanoparticles for diverse technological applications, there is great interest in understanding how to control their physico-chemical properties. This chapter addresses the role of nanoparticle size. It starts with a brief discussion of structural and energetic properties of bulk and monolayer $MoSe_2$, a prototype example of the widely studied TMDs of group 6. The discussion is focused on the comparison between the three most important layer polytypes (2H, 1T, and 1T′) and is followed by an analysis of finite-size 2D systems, herein termed nanoflakes. The role of nanoflake size in the relative phase stability is demonstrated, and the major factors that lead to this trend are examined, along with the electronic properties of the systems.

3.1 Structural and energetic properties of bulk $MoSe_2$

The most prominent structural phases of TMDs with TMs from group 6 (Mo, W) are the 2H, 1T, and 1T′ layered polymorphs,[31,33] which are depicted in Figure 1, and whose main features were described in section 1.2. With respect to crystal structures, the 2H polytype has hexagonal lattice and belongs to $P6_3/mmc$ space group, with 2 MQ_2 formula units (f.u.) in the unit cell ($Z = 2$);[112] the 1T crystal has hexagonal lattice, $P\bar{3}m1$ space group, and $Z = 1$,[112] whereas the 1T′ crystal structure is formed of an orthorhombic lattice, space group $Pnm2_1$, and $Z = 4$, which is the ground state structure of WTe_2.[113] The different coordination environments of the TM atoms within the layers are indicated by the polyhedra in the figure, namely trigonal prismatic, octahedral, and distorted octahedral for the 2H, 1T, and 1T′ polytypes, respectively. The displacement pattern of TM atoms rows that appears throughout the layers of the 1T′ polytype is also highlighted.

The equilibrium lattice parameters calculated for the 2H, 1T, and 1T′ phases of $MoSe_2$ are presented in Table 1. The results for the 2H phase can be compared with experimental data,[114] yielding relative differences of 0.9 % for a_0 and b_0, while b_0 is overestimated by only 0.2 %. This good agreement reinforces the importance of including the dispersion correction on top of the DFT-PBE calculation to describe layered solids, as c_0 (layer stacking direction) is overestimated by 11.7 % if no such correction is included, despite the good accuracy for a_0 and b_0 (relative error of 0.8 %). Such trends are expected, because vdW interactions are important for interlayer bonding, whereas intralayer interactions are dominated by chemical bonds.

The nearest neighbor distances within the hexagonal planes of Mo atoms are practically the same in 2H and 1T, and are given by the respective in-plane lattice parameters b_0. However, in 1T′, Mo–Mo distances differ from b_0 due to the displacements of Mo

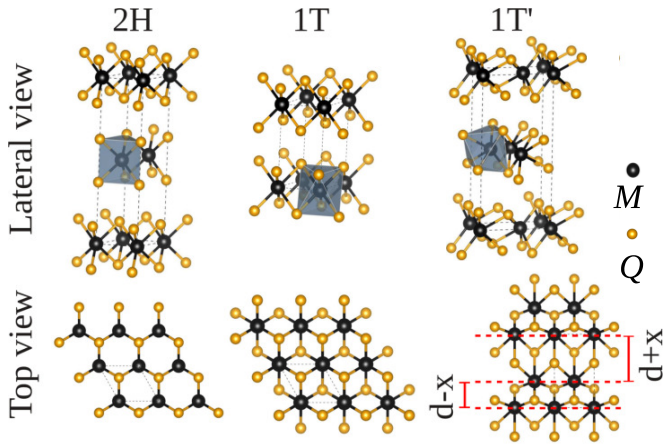

Figure 1 – Representation of bulk crystal structures of the 2H, 1T, and 1T′ polytypes of TMDs. For each polytype, the lateral view of stacked layers is shown in the top row and a top view of single layer is shown in the bottom row.

Source: Adapted from BESSE *et al.*[111]

atoms rows, and are 4.03 Å and 2.80 Å. A similar trend is observed for the vertical distance between Mo atoms planes, which is given by $c_0/2$ for 2H and 1T′, and by c_0 for 1T. This distance is very similar in 1T and 2H (difference of 0.03 Å), but in 1T′ it is 0.20 Å smaller than in 1T. Thus, the distortion in the layers allows reduced interlayer distances, because the corrugations generated in Se planes lead to smaller charge density overlap. The difference of coordination environments has little effect on the Mo–Se bond lengths, which do not change considerably from one structure to another: 2.53 Å in 2H, 2.55 Å in 1T, and an average of 2.56 Å in 1T′. Based on the relative total energy, the 2H phase is the most stable among the three polytypes, as expected from the well-known stability trend based on TM *d* electron count and orbital splitting induced by symmetry,[31,33] already discussed in Section 1.2. The 1T and 1T′ phases are higher in energy than 2H by 0.68 eV/f.u. and 0.34 eV/f.u., respectively.

Table 1 – Equilibrium lattice parameters of $MoSe_2$ in the 2H, 1T and 1T′ phases, calculated with PBE+D3.

Polytype	a_0(Å)	b_0(Å)	c_0(Å)	α(°)	β(°)	γ(°)
2H	3.28	3.28	12.96	120	90	90
1T	3.27	3.27	6.51	120	90	90
1T′	5.94	3.28	12.63	90	90	90

Source: BESSE *et al.*[111]

3.2 Relative stability of $MoSe_2$ monolayer phases

Isolated monolayers have essentially the same structural features of monolayers in the bulk crystals, for instance, Mo – Se bond lengths are increased by only 0.01 Å in 1T and 1T′, whereas in 2H it is increased by less than 0.005 Å. Likewise, the relative stability of monolayer phases has the same trend of the bulk phases, with very similar relative energies, namely 0.33 eV/f.u. and 0.70 eV/f.u. for 1T′ and 1T, respectively, relative to the ground state 2H. These results are expected because the interlayer interactions are dominated by weak vdW forces, and therefore, it can be expected that a good description of the two-dimensional systems, that is, without layer stacking, can be achieved without including the vdW dispersion correction in the total energy. In fact, bond lengths of monolayer structures optimized with PBE and without the D3 vdW correction differ from PBE+D3 results by less than 0.003 Å, and relative energies change by less than 13 meV/f.u. Thus, all remaining analyses of two-dimensional systems discussed in this chapter were safely performed without employing the D3 vdW correction.

The lower energy of the 1T′ phase in comparison with 1T can be described based on the Peierls transition.[115] This transition model was originally developed for a one-dimensional chain of atoms, demonstrating that the formation of dimers decreases the energy of the system, due to the breaking of degeneracies in energy levels and creation of a band gap, with a decrease in the energy of occupied electron states. A similar property is clearly demonstrated by the $MoSe_2$ octahedral monolayers. The 1T monolayer can be described with the same orthorhombic supercell of the 1T′ phase, as depicted in Figure 2(a), and the band structures for 1T and 1T′ monolayers across the Brillouin Zone of each corresponding orthorhombic cells are shown in Figure 2(b), along with the total density of states (DOS). In the band structure of 1T, there are degeneracies in the high symmetry point Y, which is on the edge of the reduced Brillouin zone. These degeneracies are broken by the structural distortions of the 1T′ monolayer, which consist mainly of the displacements of Mo atoms rows throughout the structure, causing a decrease in the energy of occupied electron states, analogous to the one-dimensional Peierls transition model. This is noted by comparing the band structures of Figure 2(b), for instance with the band gap of around 3 eV that is created at the Y point in the band structure of 1T′ and consequent decrease in the density of states at the Fermi level. Therefore, the decreased energy contribution from the electronic bands causes the energetical stabilization of the 1T′ phase in comparison with 1T.

The distortion mechanism of $MoSe_2$ octahedral monolayers causes the 1T phase to be unstable upon geometrical relaxations, as schematized in Figure 3(a). The 1T configuration is preserved after relaxation only if a 1×1 hexagonal unit cell is employed since the periodic boundary conditions of the lattice constrain the ions displacements and do not allow the formation of the pattern o distances between Mo rows. On the other hand,

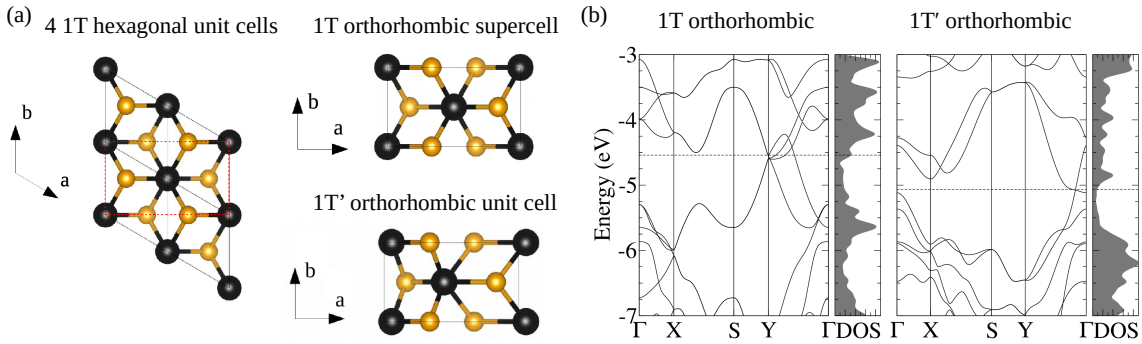

Figure 2 – (a) Schematics of the relation between the hexagonal unit cell of 1T monolayer and the orthorhombic unit cell of 1T′ monolayer, where an orthorhombic supercell for 1T is highlighted in the representation of four 1T hexagonal unit cells. (b) DFT-PBE band structures of the 1T and 1T′ monolayers with orthorhombic cell. Energy levels are aligned with respect to the vacuum level, and dashed horizontal lines indicate the Fermi energy.

Source: Adapted from BESSE *et al.*[111]

if hexagonal 2×2, hexagonal 3×3, and orthorhombic 2×1 supercells are employed for the 1T monolayer, a distorted configuration is obtained, in line with results reported for MoS_2 monolayers.[116] Due to the lattice constraints of each supercell, among the cases investigated, only the hexagonal 2×2 and orthorhombic 2×1 cells generate the same structural configuration and energy of the 1T′ monolayer. Since no analogous distortion mechanism exists for the trigonal prismatic structure, no structural distortions are observed in relaxed 2H monolayers.

3.3 Effect of nanoflake size on the relative phase stability

To study finite two-dimensional $MoSe_2$ systems and the role of size in their properties, $(MoSe_2)_n$ nanoflakes with n = 15, 63, 108, 130, 154, and 192 were constructed as carved fragments from 2H and 1T monolayers. These fragments have zigzag edges that are all Se-terminated in 1T, whereas in 2H-derived fragments both Mo-terminated and Se-terminated edges are found, as indicated in Figure 3(b) for the example of n = 108, whereas remaining sizes are shown in Figure 4. Due to the instability of 1T monolayers, 1T nanoflakes are strongly reconstructed after structural relaxations done by minimization of atomic forces. As can be seen in Figure 3(b) for n = 108, and in Figure 5 for the other sizes, the 1T-derived nanoflakes adopt the structural configuration of the 1T′ phase. Therefore, 1T monolayer fragments directly evolve to 1T′ nanoflakes, and there is no need to include further 1T′ nanoflakes built from fragments of 1T′ monolayer. As no such structural instability exists for the 2H monolayer, structural relaxations in 2H monolayer fragments cause no noticeable reconstructions in the core of the nanoflakes, but the Mo-terminated edges are strongly reconstructed. The Mo atoms are displaced to

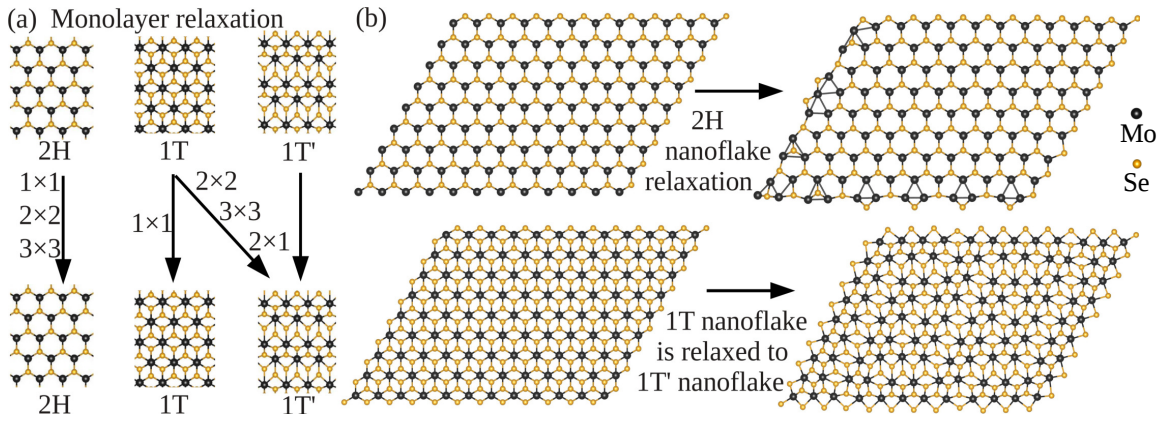

Figure 3 – (a) Effect of structural relaxation on 2H, 1T, and 1T′ monolayers for different cell sizes. (b) $(MoSe_2)_{108}$ nanoflakes before structural relaxation (2H and 1T monolayer fragments), and after relaxation (2H and 1T′ nanoflakes).

Source: Adapted from BESSE *et al.*[111]

the interior of the nanoflake and the closest Se atoms are displaced outwards. The same reconstruction pattern, which can be described as a self-passivation of metal atoms, has been reported from calculations of MQ_2 nanoribbons.[117] Therefore, hereafter, the carved fragments after relaxation of 2H and 1T monolayers will be referred to as 2H and 1T′ nanoflakes, respectively.

The relative total energies of relaxed 2H and 1T′ nanoflakes as a function of size are shown in Figure 6(a). It is observed that the relative energy between the phases is strongly affected by the nanoflake size, and that contrary to the bulk and monolayer results, the 1T′ phase has the lowest energy for nanoflakes with $n < 150$. Therefore, a 1T′ $\rightarrow$ 2H phase preference transition is shown to be induced by the increase of nanoflake size. To gain further insight into the effect of size on the relative stability of the phases, the relative energy of the relaxed nanoflakes as a function of size was fitted with a function of form $\Delta E_{2H-1T'} = (-0.32 + ae^{-bn})(\text{eV/f.u.})$, where $-0.32\,\text{eV/f.u.}$ is the energy difference between 1T′ and 2H monolayers, i.e. the function is constrained to converge to this value for $n \rightarrow \infty$. The coefficients obtained by the fitting were $a = 1.074\,\text{eV/f.u.}$ and $b = 0.008/\text{f.u.}$, and based on this, relative energies within a 10 % difference from the monolayer limit are obtained with $n > 420$ f.u. The relative energy of unrelaxed nanoflakes (2H and 1T monolayer fragments) were also evaluated, Figure 6(b), showing that 1T has the lowest energy only for $n = 15$. Therefore, the Peierls distortions play an important role to determine the relative energy trend among nanoflakes and the size-induced phase transition.

The effect of nanoflake size on the relative energy of the phases can be explained based on the difference of their edge formation energies since the relative contribution from edge energy to the total energy of the nanoflake decreases as n increases. Here, the edge

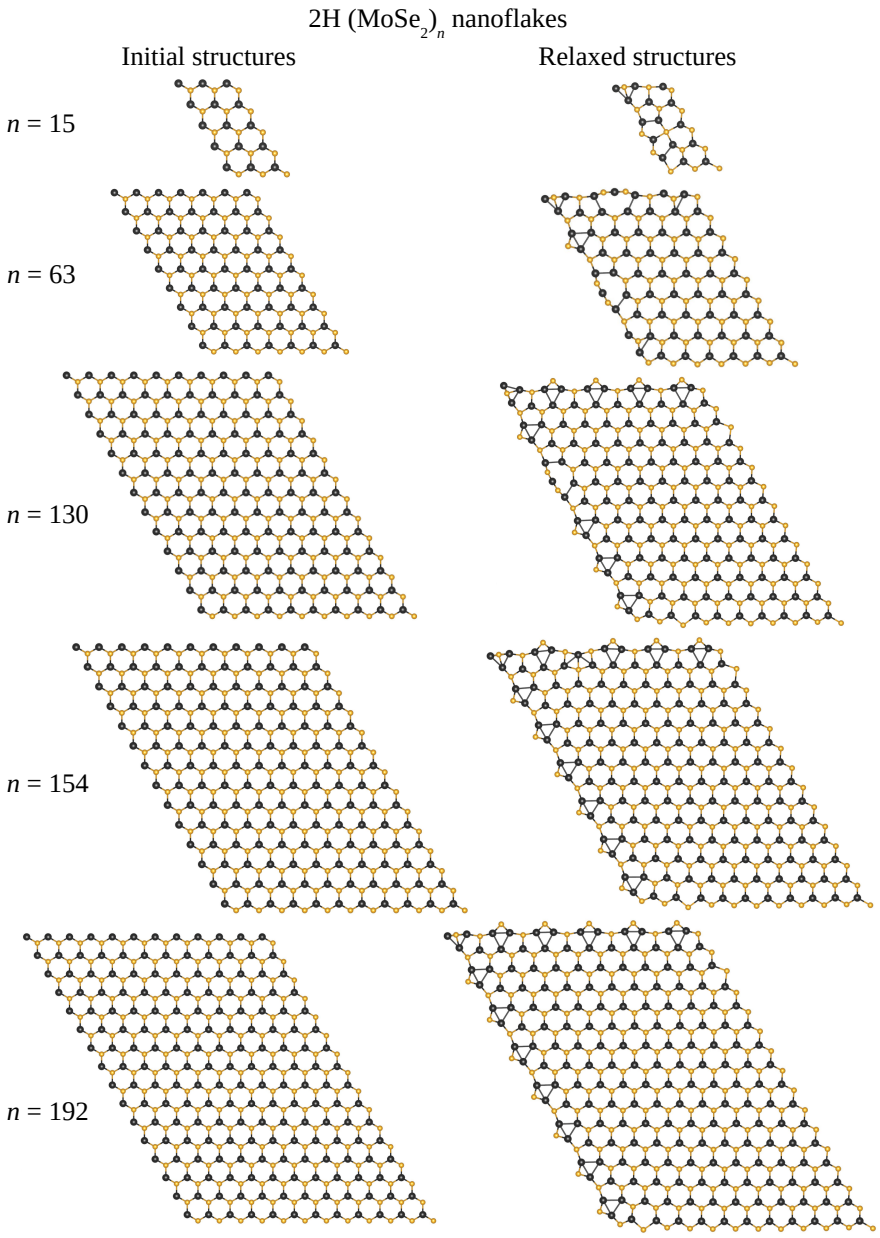

Figure 4 – Atomic structural configurations of the 2H-$(MoSe_2)_n$ nanoflakes with n = 15, 63, 130, 154, 192. On the left column, are shown the initial configurations, obtained as carved fragments of the 2H monolayer, and on the right are shown the resulting configurations after structural relaxation. Mo and Se atoms are represented by the black and yellow spheres, respectively.

Source: By the author.

energy per f.u. E_{edge} is estimated by comparing the total energy of the nanoflakes with the total energy of the monolayers, $E^n_{\text{edge}} = E^n_{\text{nanoflake}} - E_{\text{monolayer}}$, where $E^n_{\text{nanoflake}}$ is the total energy per f.u. of the relaxed nanoflake with n f.u. and $E_{\text{monolayer}}$ is the total energy per f.u. of the monolayer, in which 2H nanoflakes were compared with the 2H monolayer and 1T′ nanoflakes were compared with the 1T′ monolayer. The results obtained with this

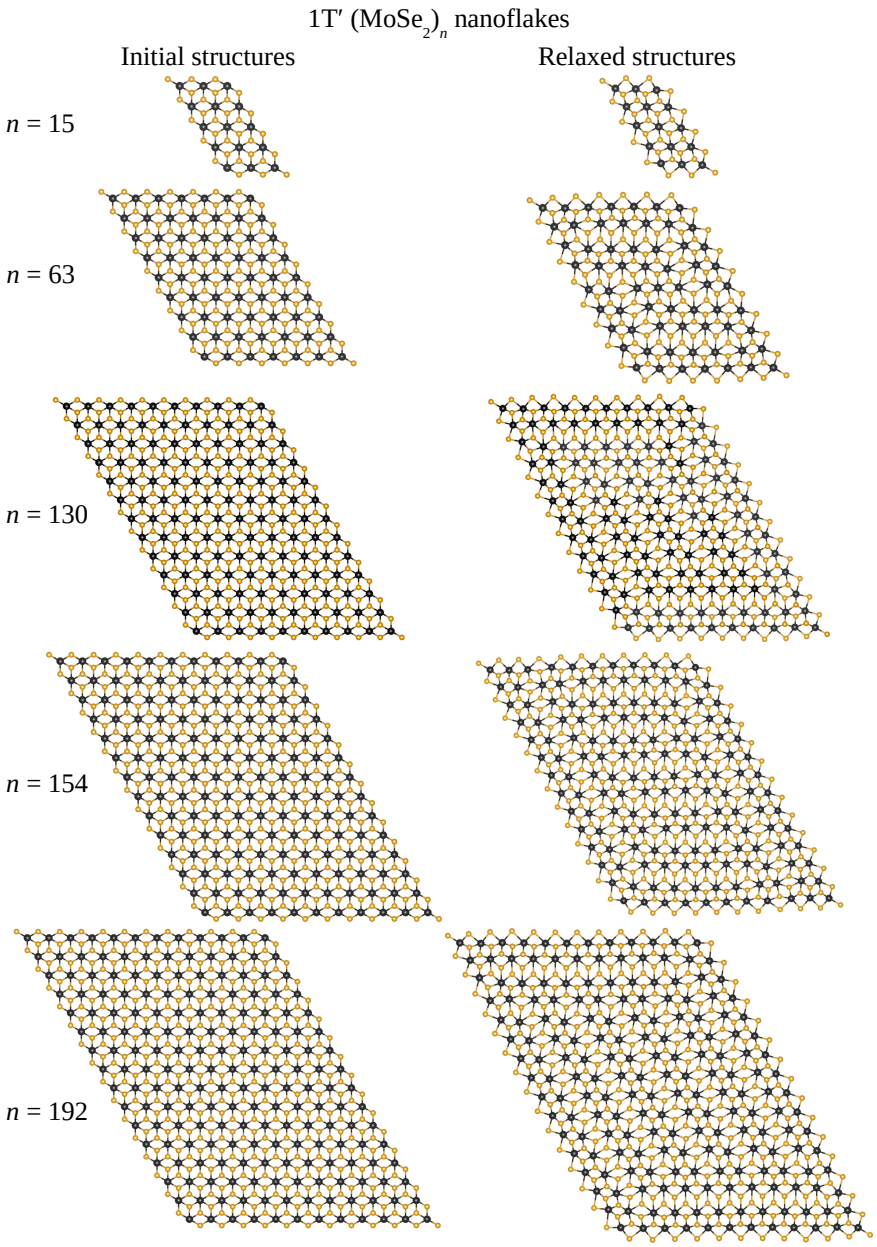

Figure 5 – Atomic structural configurations of the 1T- and 1T′-$(MoSe_2)_n$ nanoflakes with n = 15, 63, 130, 154, 192. On the left column, are shown the initial configurations, obtained as carved fragments of the 1T monolayer, and on the right are shown the resulting configurations after structural relaxation. Mo and Se atoms are represented by the black and yellow spheres, respectively.

Source: By the author.

analysis are shown in Figure 6(c) and show that 2H nanoflakes have higher E_{edge} than 1T′ nanoflakes, thus corroborating the role of difference of edge formation energy in the size-induced phase preference transition.

One of the major features of the structural phase diversity in 2D MoQ_2 is that these compounds are semiconductors in the 2H phase and metals in 1T and 1T′.[31] Therefore,

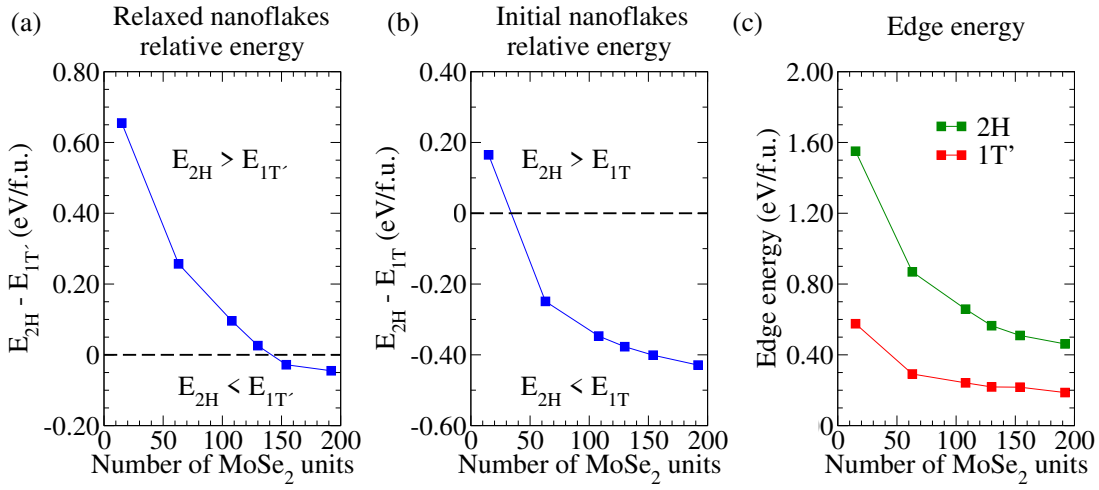

Figure 6 – (a) Relative total energies of 2H and 1T′ relaxed $(MoSe_2)_n$ nanoflakes as a function of n. (b) Relative energy between unrelaxed $(MoSe_2)_n$ nanoflakes (2H and 1T monolayer fragments) as a function of n. (c) Edge formation energy of 2H and 1T′ relaxed $(MoSe_2)_n$ nanoflakes as a function of n; the model employed to estimate the edge formation energy is described in the text.

Source: Adapted from BESSE *et al.*[111]

it is also important to investigate how the size effects influence the electronic properties of the nanoflakes. To perform this analysis the DOS of the systems were obtained, and results for some examples of nanoflakes sizes, as well as for 2H and 1T′ monolayers are shown in Figure 7. The absence of energy gap in 1T′ monolayer is also observed for the 1T′ nanoflakes, and the DOS of 1T′ nanoflakes have the same general characteristics as the 1T′ monolayer. On the other hand, although the 2H monolayer has a non-zero band gap, the 2H nanoflakes exhibit a metallic-like density of states, which is in contrast with the expected trend of band gap increase due to quantum confinement effects. This is caused by the existence of edges in the nanoflaes, which can be observed with the distinction of edge and core atoms adopted for the DOS analysis. The electronic states of 2H nanoflakes that are within the energy range of the 2H monolayer band gap are mainly derived from edge Mo *d*- and edge Se *p*-states. On the other hand, the contributions from core atoms are not very relevant in this energy range and are very similar to the DOS of the 2H monolayer.

3.4 Summary

The bond lengths and coordination environments of $MoSe_2$ in 2H, 1T, and 1T′ phases are essentially the same in bulk and monolayers because interlayer bonding is dominated by weak vdW interactions. Similarly, the relative stability between the phases is also not modified by layer stacking, with 2H as the ground state structure. The lower energy of the distorted 1T′ structure compared to 1T can be explained based on the

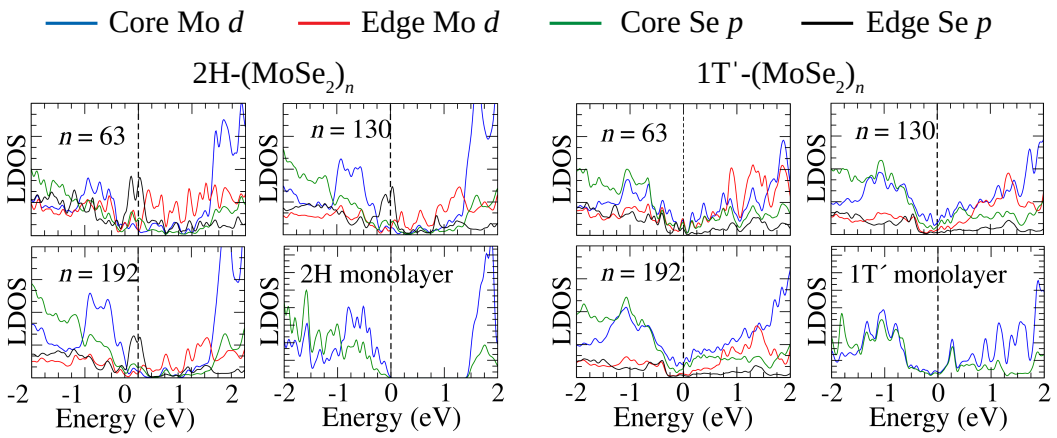

Figure 7 – Local density of states of 2H and 1T′ $(MoSe_2)_n$ nanoflakes, $n = 63$, 130, 192, and of 2H and 1T′ monolayers. The contributions are distinguished between core atoms and edge atoms. Here, edge atoms are defined as the atoms that form the outermost rows of each chemical species (Mo and Se). The energy of the occupied state with the highest energy is set to zero.

Source: Adapted from BESSE *et al.*[111]

Peierls transition mechanism because the displacements of Mo atoms rows throughout the 1T′ monolayer open a band gap in the edge of the Brillouin zone and reduce the density of states at the Fermi level. Carved fragments of 2H and 1T monolayers were employed to study $(MoSe_2)_n$ nanoflakes, and because of the instability of the 1T phase, octahedral nanoflakes naturally adopt the distorted 1T′ configuration upon structural optimization. In contrast to bulk and monolayer, 1T′ is the lowest energy phase for small size ($n < 150$) $(MoSe_2)_n$ nanoflakes, and therefore, the nanoflake size has an important effect on the relative stability of trigonal prismatic and octahedral phases. A size-induced phase preference transition was shown to occur around $n = 150$, which is influenced by the difference of edge formation energies of the two phases, as the 2H phase has larger edge energy than 1T′. The presence of edges in the 2H phase leads to the formation of metallic-like electronic states, whereas in the 1T′ no difference is observed between edge- and core-derived DOS, which both resemble the general features of the 1T′ monolayer DOS.

4 DICHALCOGENIDES OF Fe-, Co-, Ni-, AND Cu-GROUPS

Research on 2D TMDs has mostly focused on compounds with early TMs, specially Mo and W, because they are readily obtained in layered phases. However, novel 2D materials have been obtained beyond traditional layered solids, and there has been growing interest in TMDs based on other TMs. Therefore, the screening and understanding of the physical properties of 2D TMDs based on late TMs, can help to guide the design of novel 2D materials. Aligned with that, this chapter presents an exploration of the MQ_2 compounds with M = Fe, Ru, Os, Co, Rh, Ir, Ni, Pd, Pt, Cu, Ag, and Au, and Q = S, Se, and Te. The discussion addresses the structural properties and relative stability of several phases, the characterization of interlayer binding in layered phases, and the electronic band gaps of the materials, to understand the effects of structure dimensionality and the band offsets trends among monolayers.

4.1 Crystal structures

Beyond the layered polytypes discussed in Chapter 3 (2H, 1T, and 1T′), MQ_2 compounds with M from Fe-, Co-, Ni-, and Cu-groups can be found in other crystal structures, including phases that are not formed by the stacking of weakly interacting layers. To compare the stability and properties of layered and non-layered phases, a set of 11 crystal structures, represented in Figure 8, was employed. This set is composed of the 2H, 1T, and 1T′ polytypes, plus all crystal structures experimentally reported for any MQ_2 composition (with M = Fe, Ru, Os, Co, Rh, Ir, Ni, Pd, Pt, Cu, Ag, and Au, and Q = S, Se, and Te) in two crystal structure databases, the Inorganic Crystal Structure Database,[119] and Crystallography Open Database.[120] The layered phases in this set, hereafter termed 2D structures, also have the PdS2-type structure,[121] and the calaverite structure of $AuTe_2$.[122] The PdS2-type structure is composed of puckered MQ_2 layers formed of pentagonal rings with four $M-Q$ bonds and one $Q-Q$ bond. The calaverite structure can be described as a distorted 1T structure, where the angle of the lattice vector in the stacking direction slightly deviates from 90° and the bond lengths in the MQ_6 octahedra are not equal.

The crystal structures that are not formed by layer stacking are here referred to as 3D structures. The pyrite phase is widely observed among MQ_2 compositions with $3d$ metals from all the selected TM groups,[51] and it can be generated by reducing the interlayer distances of the PdS_2-type structure.[123] A distorted-pyrite configuration proposed for FeS_2[124] was also included in the set. The marcasite structure, also reported for several TMDs, such as FeS_2, $FeSe_2$ and $CuSe_2$,[52,125] has some similarities with pyrite, as both can be described in terms of MQ_6 octahedra with tetrahedrally coordinated sulfur atoms. However, pyrite has only corner-sharing MQ_6 octahedra, and marcasite has edge

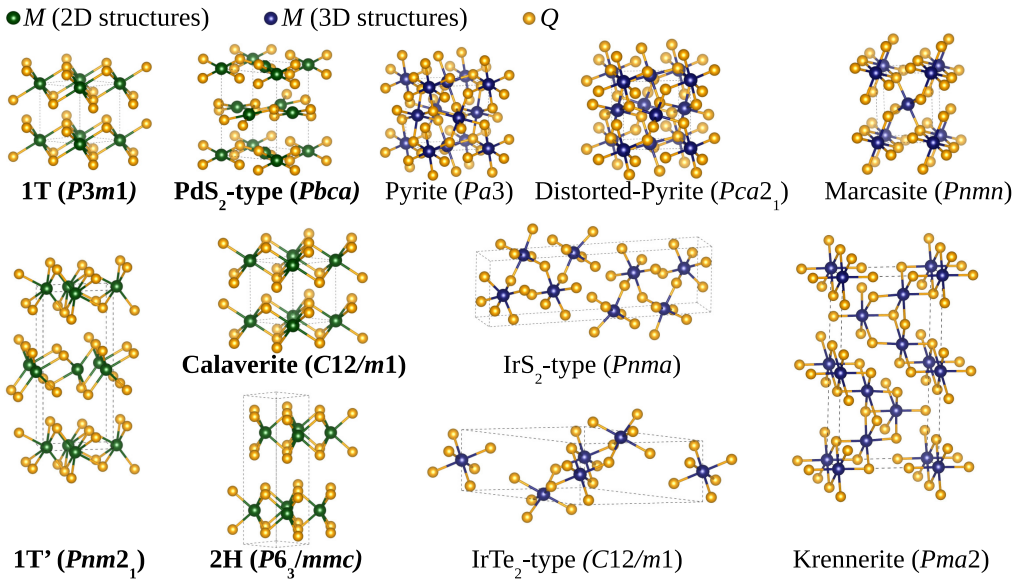

Figure 8 – Depiction of MQ_2 crystal structures, with space groups indicated in parentheses. Chalcogen atoms are represented by yellow spheres, and metal atoms are represented by green spheres in layered crystals and blue spheres in non-layered crystals. The dashed lines indicate the primitive cells.

Source: BESSE; LIMA; DA SILVA.[118]

sharing in one of the unit cell directions. The structures adopted by Ir dichalcogenides, IrS_2-type,[126] and $IrTe_2$-type,[127] have a framework of interconnected MQ_6 octahedra with low compactness, which is also a characteristic of the krennerite structure, found for of $AuTe_2$.[128]

4.2 Structural properties and relative phase stability

Systems were set up with the 36 MQ_2 compositions in the 11 crystal structures described in the previous section, and their equilibrium geometries were obtained by minimization of stress tensor and forces on atoms. In Appendix B, the equilibrium lattice parameters and relative energies of all phases are listed for all compositions, as well as available experimental lattice parameters. Compared to experimental results, all relative differences are lower than 3 %, except for 1T-$NiTe_2$, 1T-PtQ_2, and calaverite-$AuTe_2$, that have relative errors between 3 % and 9 %, mainly related to underestimated interlayer distances. On average, relative error is of 2.0 %, as commonly found with the employed level of calculation.

There are systems in which the structural optimization leads to significant modifications of the structural configurations, and the equilibrium geometries do not keep the general features of the prototypes shown in Figure 8. For instance, the PdS_2-type structure is unstable for most compositions and is relaxed to the pyrite structure through the

compression of interlayer spacing, except for PdS_2, PtS_2, $PtSe_2$, AuS_2 and $AuSe_2$. This trend can be understood based on the mechanism of stabilization of the PdS_2-type structure.[123] The formation of octahedral environments in the pyrite structure is favored by bonds with high ionicity and counterbalanced by the repulsion of orbitals from adjacent layers. Therefore, the layered phase in stabilized in the cases which have M d_{z^2} orbitals of larger spatial extension and lower ionicity. Another example is the 1T′ structure, which is preserved only in systems with M = Fe, Co, Ni, and the remaining cases adopt the 1T configuration. The 1T′ structure is not stabilized for all compositions because the Peierls mechanism related to the displacements of M atoms rows depend on the occupation of the electronic bands to effectively decrease the electronic energy, as discussed in Section 3.2. The equilibrium 1T and calaverite structures are virtually identical for the majority of compounds, because calaverite tilting angles deviate from 90° by less than 0.5° and energy differences are smaller than 10 meV/f.u, but exceptions are found among most of the compounds with M of the Cu-group. Furthermore, the distorted-pyrite model yields no considerable differences to the pyrite structure, as energy differences are smaller than 1 meV/f.u., and lattice parameters differ by less than 0.2 %.

The lowest energy structures of all compounds are shown in Figure 9. In agreement with experimentally reported crystal structures, the pyrite structure is the most common among the studied materials. Compounds with Fe and Au energetically favor the marcasite and krennerite phases, respectively, and those with M of Co-group have lowest energy in IrS_2- or $IrTe_2$-type structures. Layered phases are favored for Ni-group TMDs, as expected based on the experimentally reported phases for these compounds,[31,50,126] and 1T/calaverite geometry is the most common, as PdS_2-type occurs only for PdS_2. Besides these compounds, the calaverite structure is also the one with lowest energy for $CuTe_2$. The role of chemical composition on the bond lengths of the lowest energy phases was analyzed via the average weighted bond lengths (d_{av}),[129] and the results are summarized in Figure 10(a). As expected, the bond length increases as the chalcogen atomic radius increases.[130] However, the trends for M substitutions are not well defined, which can be understood based on the lower amplitude of atomic radii among the studied M compared to Q. For instance, reference atomic radii are 1.00 Å, 1.15 Å, and 1.40 Å for S, Se, Te, respectively, but among all TMs it varies only between 1.30 Å and 1.40 Å, except for Ag (1.60 Å).[130] Thus, bond length variations due to M substitutions can be more sensitive to other effects, such as the local coordination environment and charge transfer in the different phases.

To obtain further insights into the stability of 2D crystals, and to study their energetic and electronic properties and contrasts with the 3D structures, the lowest energy 2D and 3D structures of each compound were selected as examples. As discussed above, $CuTe_2$ and all compounds with M from Ni-group, except NiS_2, have 2D crystals as lowest energy crystal structures, which are PdS_2-type for PdS_2 and 1T/calaverite for the remain-

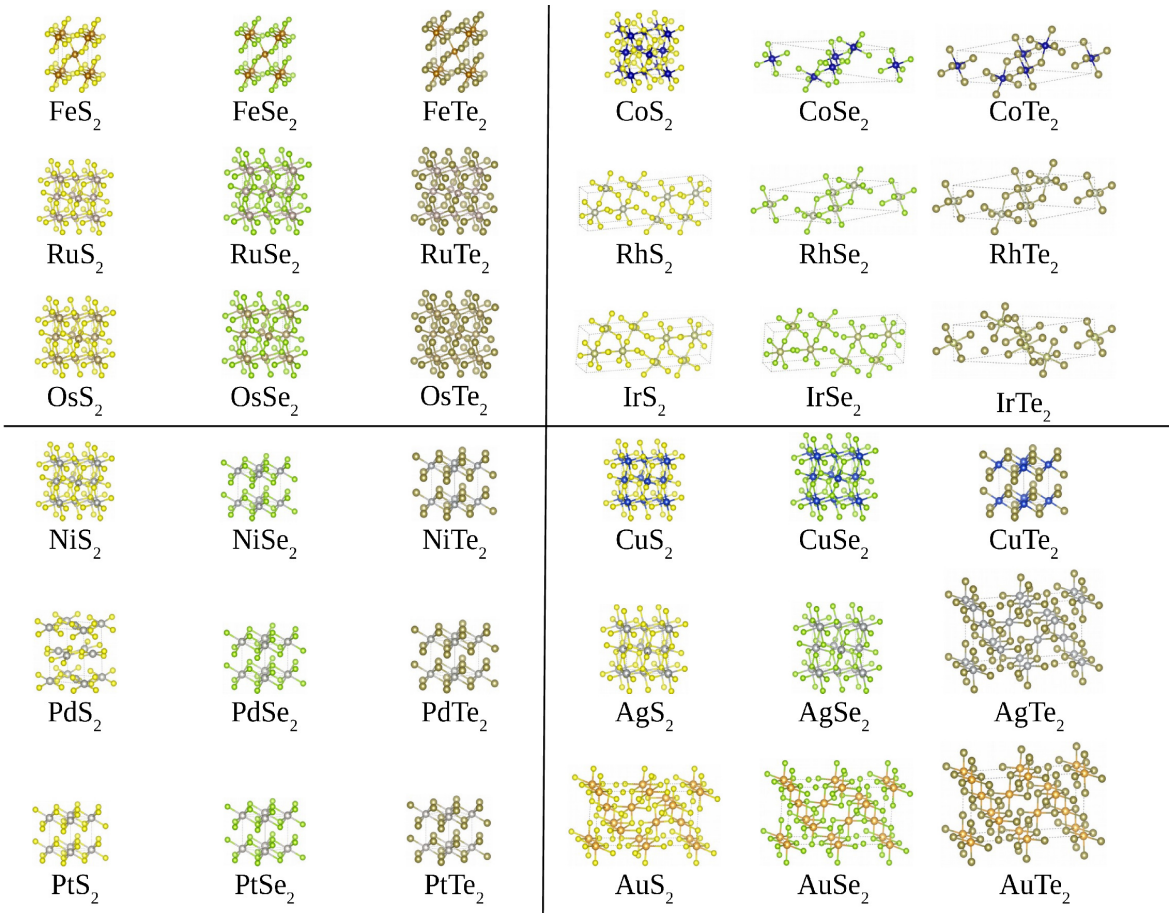

Figure 9 – Crystal structures with the lowest total energy for each compound: marcasite for FeS_2, $FeSe_2$, and $FeTe_2$; pyrite for RuS_2, $RuSe_2$, $RuTe_2$, OsS_2, $OsSe_2$, $OsTe_2$, CoS_2, NiS_2, CuS_2, $CuSe_2$, AgS_2, and $AgSe_2$; $IrTe_2$-type for $CoSe_2$, $CoTe_2$, $RhSe_2$, $RhTe_2$, and $IrTe_2$; IrS_2-type for RhS_2, IrS_2, $IrSe_2$; 1T for $NiSe_2$, $PdSe_2$, and $PtTe_2$; calaverite for $NiTe_2$, $PdTe_2$, PtS_2, $PtSe_2$, and $CuTe_2$; krennerite for $AgTe_2$, AuS_2, $AuSe_2$, and $AuTe_2$; PdS_2-type for PdS_2.

Source: BESSE; LIMA; DA SILVA.[118]

ing. For these compounds, the lowest energy structure among 3D crystals is $IrTe_2$-type for $NiSe_2$, $NiTe_2$ and PtS_2, pyrite for PdS_2 and $PdSe_2$, and krennerite for $PdTe_2$, $PtSe_2$, $PtTe_2$ and $CuTe_2$. The other compounds have the 3D structures of Figure 9 as the lowest energy structures, and their lowest energy 2D structures are 1T′ structure in the cases with M from Fe-group, and 1T/calaverite in the remaining compositions. All the lowest energy 2D structures have octahedral metal coordination environments, except PdS_2. Therefore, the intralayer trigonal prismatic coordination of TM atoms that occurs in the 2H phase, is not energetically favored in comparison with the octahedral coordination for the late TMs, which is in contrast with the MoQ_2 and WQ_2 materials.

The relative energies between the lowest energy 2D and 3D structures are displayed in Figure 10(b), which highlights the energetic preference for 2D structures in Ni-group

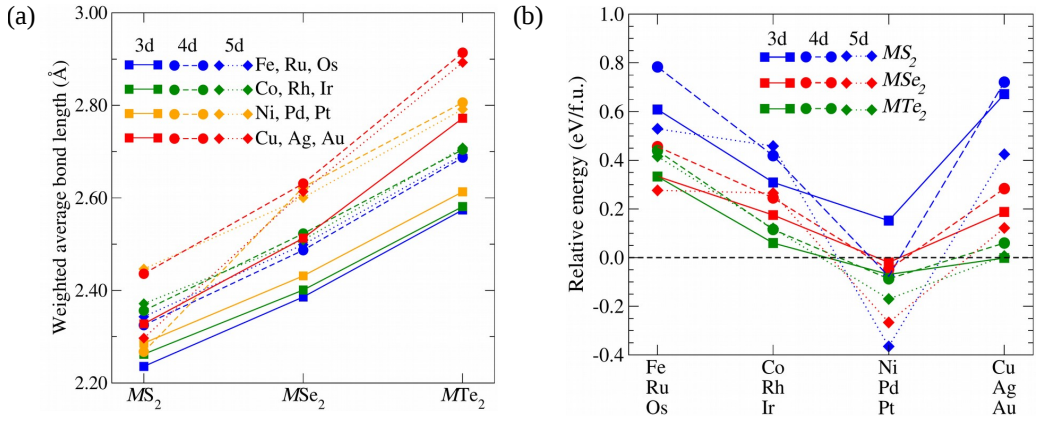

Figure 10 – (a) Average weighted bond lengths of the lowest energy crystal structures of MQ_2 compounds, as a function of the chalcogen species. The color and filling of symbols denote the transition metal species. (b) Relative energy between the lowest energy layered structure and the lowest energy non-layered structure of each MQ_2 compound. Symbol shape and color indicate the M period and Q species, respectively. Lines are drawn as guides to the eye, and their styles (solid, dashed, dotted) indicate the M period.

Source: Adapted from BESSE; LIMA; DA SILVA.[118]

compounds and $CuTe_2$. The 2D−3D relative energy decreases as Q is changed from S to Se to Te, mainly because of the decrease of bond strength as atomic radius increase, due to reduced ionic character. There is a trend of increased stabilization of 2D structures as M varies between Fe-, Co-, and Ni-groups, which is not followed as M goes from Ni-group to Cu-group. However, this trend must be understood beyond the simple distinction between 2D and 3D structures, because of the variety of crystal phases, specially among the 3D structures. For some compounds, the distinction provides an accurate picture, for instance, the FeQ_2 compounds, for which all 3D structures (except krennerite) have lower energy than all 2D structures, and PtQ_2, that has 2H as the only 2D structure higher in energy than the 3D structures. However, a different situation is observed for AuQ_2, for which krennerite is the unique 3D structure lower in energy than the 2D structures. Therefore, the energetic preference for a structural phase, more than the dimensionality of the structure framework (2D or 3D), is the determinant factor for the relative stability trends among the compounds and crystal phases investigated here.

4.3 Interlayer Binding

The main interest in layered solids in the context of this thesis is to investigate potential novel 2D materials. For that, characterizing the interlayer binding is of great importance, as it can help to assess the possibility to exfoliate ultrathin sheets from 2D crystals,[13,14] and the exfoliation energy (E_{exf}) is an important parameter, which measures the energy required to peel one layer of the crystal surface. It has been shown that E_{exf} can

Table 2 – Magnitude of exfoliation energies (E_{exf}) of the lowest energy MQ_2 layered crystals, obtained with PBE+D3.

Material	E_{exf}(meV/Å^2)	Material	E_{exf}(meV/Å^2)
1T′-FeS_2	24.5	1T-NiS_2	37.8
1T′-$FeSe_2$	31.0	1T-$NiSe_2$	47.8
1T′-$FeTe_2$	36.0	1T-$NiTe_2$	54.6
1T′-RuS_2	28.8	PdS_2-type-PdS_2	31.9
1T′-$RuSe_2$	32.0	1T-$PdSe_2$	49.4
1T′-$RuTe_2$	37.8	Calaverite-$PdTe_2$	58.0
1T′-OsS_2	29.9	Calaverite-PtS_2	34.5
1T′-$OsSe_2$	32.5	Calaverite-$PtSe_2$	39.8
1T′-$OsTe_2$	35.7	1T-$PtTe_2$	47.5
1T-CoS_2	58.3	Calaverite-CuS_2	104.8
1T-$CoSe_2$	56.4	Calaverite-$CuSe_2$	104.9
Calaverite-$CoTe_2$	55.2	Calaverite-$CuTe_2$	89.2
Calaverite-RhS_2	65.7	Calaverite-AgS_2	123.2
1T-$RhSe_2$	63.9	Calaverite-$AgSe_2$	111.8
Calaverite-$RhTe_2$	62.6	Calaverite-$AgTe_2$	96.4
1T-IrS_2	55.6	1T-AuS_2	75.6
1T-$IrSe_2$	60.2	Calaverite-$AuSe_2$	83.3
Calaverite-$IrTe_2$	63.0	Calaverite-$AuTe_2$	84.1

Source: By the author.

be assumed to have the same value of the interlayer binding energy,[15] that is, the energy difference between a monolayer in the crystal and an isolated monolayer. Therefore, E_{exf} was calculated using

$$E_{exf} = \frac{(E_{\text{cell}}^{\text{bulk}}/N) - E_{\text{monolayer}}}{S} \ , \tag{4.1}$$

where $E_{\text{cell}}^{\text{bulk}}$ is the total energy per unit cell, N is the number of layers per unit cell (1 for 1T and calaverite, and 2 for 1T′ and PdS_2-type), and $E_{\text{monolayer}}$ is the total energy of a single isolated monolayer. The E_{exf} of the lowest energy 2D crystals of each compound were evaluated and the results are shown in Table 2. In systems with weakly interacting layers, vdW forces play an important role in interlayer binding, however, no clear correlation was found between the magnitude of E_{exf} and the polarizability of the free atoms of M and Q in the composition,[131] which is in line with literature data for other layered crystals.[15] Furthermore, the wide range of observed E_{exf} values, from 24.5 meV/Å^2 to 111.8 meV/Å^2 indicates that other types of interactions also have important contribution to the magnitude of the exfoliation energy.

All studied materials have larger exfoliation energies than the layered TMDs of Ti-, V-, and Cr-groups for results obtained with the same methodology, which are all between 10 meV/Å^2 and 22 meV/Å^2.[132] Other theoretical studies of vdW layered crystals have employed different methods to address the dispersion interactions. It has been found that

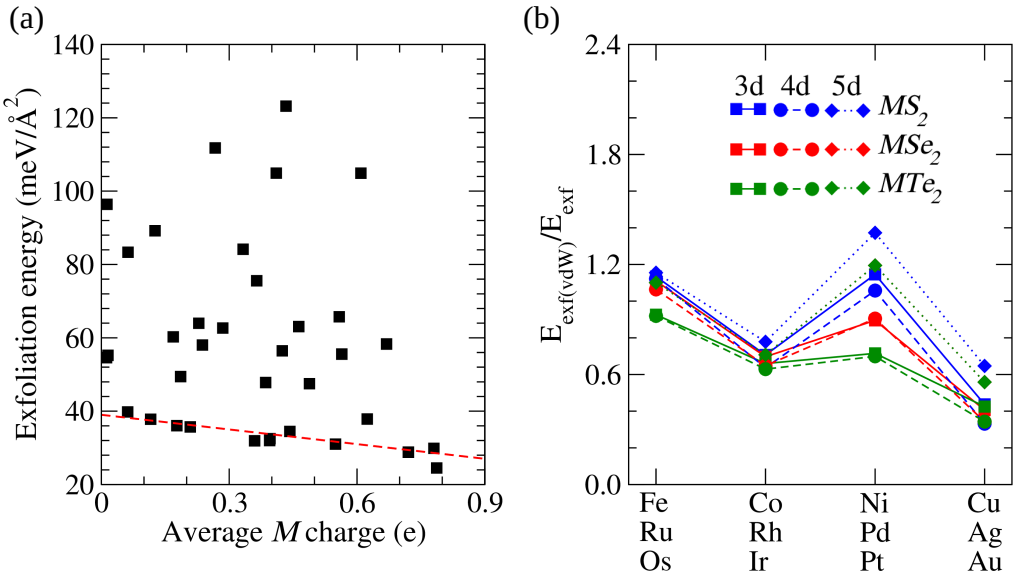

Figure 11 – (a) Magnitude of exfoliation energies of the lowest energy 2D structures of the MQ_2 compounds, as a function of the magnitude of average effective charge on the transition metal atoms. The dashed red line is a linear fit for materials with exfoliation energy below 40 meV/Å^2 ($R = 0.780$). (b) Ratio between the exfoliation energy calculated from dispersion energy term ($E_{exf((\mathrm{vdw})}$) and from the total energy (E_{exf}), as described in the text.

Source: Adapted from BESSE; LIMA; DA SILVA.[118]

E_{exf} is close to 20 meV/Å^2 for a set of experimentally reported materials.[15] A large scale screening of potential 2D crystals classified materials with E_{exf} up to 30 meV/Å^2 as "easily exfoliable" and up to 130 meV/Å^2 as "potentially exfoliable", based on the magnitude of change in interlayer distances caused by the use of vdW functionals.[14] However, the values of E_{exf} can vary greatly depending on the method adopted to describe the dispersion interactions. For instance, here it was found that PtS_2 has $E_{exf} = 34.5$ meV/Å^2, and literature data with other methods vary between 10.3 meV/Å^2 and 29.4 meV/Å^2.[15]

DFT results for layered TMDs with M from Ti-, V-, and Cr-groups have shown a correlation between E_{exf} and the magnitude of charge transfer between M and Q within the layers, which has been explained as an effect of interlayer Coulomb repulsion due to the accumulation of negative charge in the adjacent planes of Q atoms.[132] To investigate this property, Bader charge analysis[133] was employed to perform the charge partition in the systems listed in Table 2. In this approach, the space is divided in Bader volumes by surfaces of zero flux of the gradient of electron density $n(\mathbf{r})$, that is, at each surface point $\nabla n(\mathbf{r}) \cdot \hat{\mathbf{u}} = 0$, where $\hat{\mathbf{u}}$ is the unit vector perpendicular to the surface. Each Bader volume encloses a single electron density maximum associated with the position of an ion. Therefore, this scheme allows to decompose the electron density into contributions from each atom by integrating the density over the Bader volumes, yielding Bader charges of

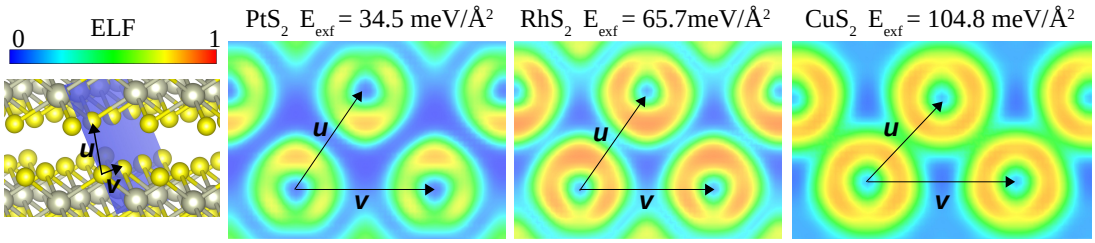

Figure 12 – Color map of the electron localization function in planes that contain Q atoms of adjacent layers in the calaverite structures of PtS_2, RhS_2, and CuS_2.

Source: Adapted from BESSE; LIMA; DA SILVA.[118]

the atoms, $Q_{B,i}$. The Bader charges in the heterobilayers were obtained with the Bader Charge Analysis code,[134] and effective charges Q^i_{eff} for each atom were obtained according to $Q_{eff,i} = Z_{val,i} - Q_{B,i}$, where $Z_{val,i}$ is the number of valence electrons included explicitly in the DFT calculation.

The results of E_{exf} and average effective charge on M for the lowest energy 2D crystals are plotted in Figure 11(a), where it can be seen that a correlation between the E_{exf} and charge transfer does not exist if all systems are considered. However, a linear decrease of E_{exf} with increasing magnitude of charge is observed in the subset of materials that have E_{exf} below $40\,\mathrm{meV/Å^2}$, which are mostly the materials with M from the Fe- and Ni-groups. This reinforces the notion that for the systems with high E_{exf} the interlayer binding has an important contribution from non-vdW interactions. The magnitude of charge transfer is directly related with the effect of interlayer repulsion only in systems with interlayer binding dominated by vdW interactions, which have low values of E_{exf}. The non-negligible contribution of chemical bonds to interlayer binding is also revealed by the analysis of $E_{exf(\mathrm{vdw})}$, defined as the value of exfoliation energy evaluated only from the D3 dispersion energy term ($E_{\mathrm{vdW}} = E_6 + E_8$, as described in Section 2.4). This value can be compared with E_{exf}, and the results for the ratio $f = E_{exf(\mathrm{vdw})}/E_{exf}$ are shown in Figure 11(b). The materials that have $E_{exf} < 40\,\mathrm{meV/Å^2}$ show f close to one, suggesting that interlayer binding comes predominantly from vdW interactions. In contrast, the large fraction of E_{exf} that comes from the pure DFT total energy in the remaining materials is likely associated with chemical bonds.

To obtain more insight into the interlayer binding, the bonds in selected systems were characterized via the analysis of the electron localization function (ELF). The definition of the ELF[135] is based on the conditional pair probability of finding an electron in the vicinity of another same-spin electron, given that a smaller probability of finding a second same-spin electron indicates an increased localization of the reference electron. The function is constructed to make $0 \leq \mathrm{ELF} \leq 1$, where values close to 1 corresponds to higher localization, as found in lone pairs. This approach is capable of providing a

useful tool for the visualization of key properties of atomic, molecular, and solid systems, such as the atomic shells and bonding electron pairs, and the analysis of the ELF topology can serve as guide to characterize bonding.[136] Three materials with calaverite crystal structure and diverse E_{exf} were selected as examples and their ELF plots are shown in Figure 12. Of these, PtS_2 has the lowest E_{exf} and belongs to the set of systems classified as having weakly interacting layers, based on the preceding discussion. The ELF plot of PtS_2 shows typical features of vdW layered TMDs, such as the peak corresponding to the electron lone pair of Q in the outermost region of the layer, and no marks of interlayer covalent bonds. However, as E_{exf} increases going to RhS_2 and CuS_2 the values of ELF in the interlayer region are raised, specially along the directions that connect adjacent Q atoms, suggesting some degree of interlayer chemical bonds.

4.4 Electronic band gaps and band offsets

The lowest energy 3D and 2D structures for each composition, and the respective monolayers, were selected as examples to study the electronic properties of the systems, as represented by the results for $RuSe_2$, shown in Figure 13, and the band structures for all the compositions are provided in Appendix B. The band structures were calculated with the HSE06 hybrid functional, keeping the geometries obtained with PBE+D3, employing **k**-paths in the FBZ according to definition proposed for a standardization of data in the literature.[137] The compositions that have non-zero in at least one of the structures are listed in Table 3, where all band gaps are indirect, with the exception of $IrTe_2$-type-PtS_2. The 3D structures with non-zero band gaps are mostly the compounds with M from Fe-group in the marcasite and pyrite structures. For 2D crystals and monolayers, the semiconductor systems are the 1T′ structures with M from Fe-group and 1T/calaverite for Ni-group TMDs. The identification of metals and semiconductors solids in these results agrees with experimental reports, except for NiS_2 and $PtSe_2$, and in these cases the underestimation of interlayer distances and corresponding broadening of electron states may be associated with the calculated zero band gap. As for monolayers, PtS_2 and $PtSe_2$ have been reported as semiconductors,[65,138] in line with the results.

An important property of 2D TMDs of group 6 (e.g. MoS_2), that played a fundamental role in the rise of interest in these materials, is the transition from indirect to direct band gap as the number of stacked layers is decreased to the monolayer limit.[30] This type of transition is not found in the studied systems, which can be explained by their crystal structure, since the direct to indirect band gap transition is associated with the orbital composition of band edge states in the 2H phase and their role in interlayer coupling effects.[64] As expected, there is a trend of band gap decrease due to layer stacking, and this leads to metallic to semiconductor transitions mainly in Ni-group materials. In these systems, layer stacking has a strong effect on the band gap, contrary to the Fe-group

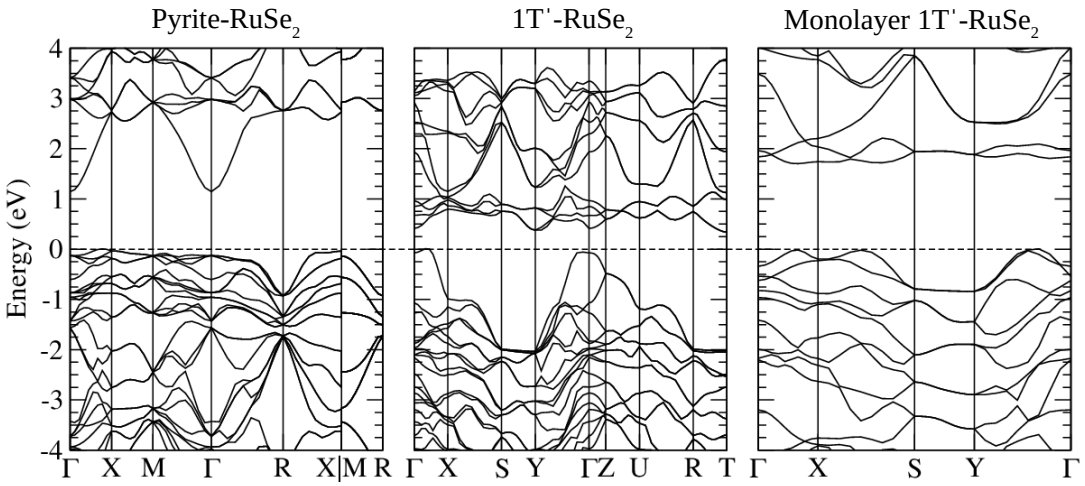

Figure 13 – Electronic band structures of the lowest energy 3D and 2D structures and corresponding monolayer of $RuSe_2$, calculated with the HSE06 functional. The top of the valence bands are shifted to zero energy.

Source: By the author.

materials and other TMDs, which has been reported for PtS_2,[65] and $PtSe_2$.[139]

A set of 17 semiconductor monolayers was found, which band gaps that range from 0.45 eV to 2.62 eV. These monolayers are the 1T′ monolayers of Fe-group, and the 1T/calaverite monolayers of the Ni-group, except for $NiTe_2$, which is a metal. The band offsets of these monolayers are depicted in Figure 14, where the VBM and and CBM were evaluated with respect to the vacuum level, which was measured as the local electrostatic potential at the middle of the vacuum distance in the simulation cell. The band offsets trends of these materials can be understood based on the orbital composition of the band edges, which are primarily of Q p-states and M d-states, where the latter predominates at the CBM and the former predominates at the CBM. As a consequence, both the VBM and CBM energies increase as the atomic number of Q increases for systems with same M, because of the increase in the energy of Q p-states and the amplification of level splitting that pushes VBM and CBM to higher energies, an effect that depends on the spatial overlap of states and on the energy difference.[74] As such, the upshift in the VBM is more significant, and consequently, the band gap decreases going from S to Te. For systems with same Q, a clear trend is also observed for the CBM offsets with the substitution of M, since M d energy levels become more shallow as the atomic number of M increases and this causes the CBM energy to increase. However, no clear trends are found for VBM offsets as a function of M for systems with same Q, suggesting a competition between the two major factors: the natural energy position of states and the role of bond lengths in the magnitude of level splitting. For Ni-group systems, the VBM goes down in energy as the atomic number of M is increased, showing that in these systems the dominant role is played by the decrease of level repulsion. As a consequence of the trends in VBM

Table 3 – Band gaps (in eV) calculated with HSE06 functional of the MQ_2 compounds in the lowest energy 3D and 2D crystals, and respective monolayers for the compositions with non-zero band gaps.

Compound	3D crystal	2D crystal	Monolayer
FeS_2	2.10	0.29	1.26
$FeSe_2$	1.52	0	1.00
$FeTe_2$	1.06	0	0.59
RuS_2	1.57	0.73	1.66
$RuSe_2$	1.14	0.33	1.65
$RuTe_2$	0.65	0	1.23
OsS_2	0.64	1.30	1.63
$OsSe_2$	0.45	0.89	1.65
$OsTe_2$	0.40	0	1.48
RhS_2	0.96	0	0
IrS_2	1.08	0	0
$IrSe_2$	0.67	0	0
NiS_2	0	0	1.11
$NiSe_2$	0	0	0.54
PdS_2	0	0.80	2.20
$PdSe_2$	0	0	1.10
$PdTe_2$	0	0	0.45
PtS_2	0.22	0.25	2.62
$PtSe_2$	0	0	1.91
$PtTe_2$	0	0	1.07
AuS_2	0.51	0	0

Source: BESSE; LIMA; DA SILVA.[118]

and CBM offsets, the band gap increases going from Ni to Pt. Notice that PdS_2 shows deviations from some trends because it is the only system with the PdS_2-type structure.

Based on the monolayers band offsets, the band alignments formed at monolayers junctions can be predicted assuming the validity of Anderson's rule. As discussed in Chapter 1, this approach adopts the same vacuum level for the monolayers upon the formation of the junction, and the heterobilayer band offsets are evaluated directly from the natural band offsets of isolated monolayers. Because of the weak interlayer interactions, this approximation is expected to have good validity in vertically stacked vdW heterostructures. Therefore, the band alignments of all pairs obtained by combinations of the semiconductor monolayers were determined according to the usual classification of semiconductor heterojunctions discussed in Section 1.3 (type-I, type-II, and type-III), as schematized in Figure 15, which also displays the results. The majority of band offsets trends discussed above lead to a simultaneous increase or decrease in the VBM and CBM energies, and therefore, the majority of junctions are classified as type-II. Type-I band alignment is more common if a monolayer with M from the Ni-group is present, because

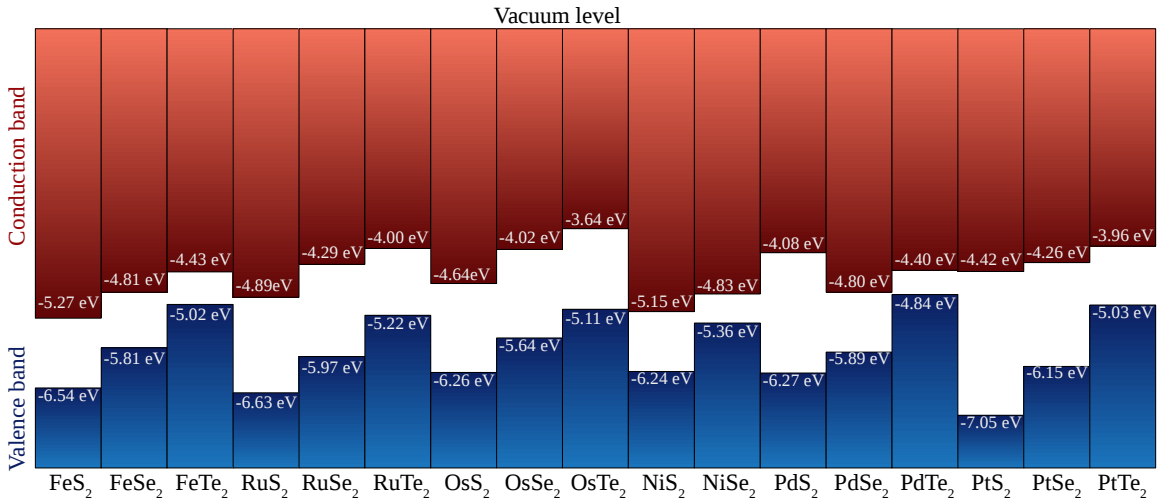

Figure 14 – Valence and conduction band offsets of the 17 semiconductor MQ_2 monolayers obtained with the HSE06 functional. The VBM and CBM values with respect to vacuum level are shown.

Source: BESSE; LIMA; DA SILVA.[118]

of the opposite trends in the VBM and CBM offsets found in these materials. Finally, type-III is the less common and occurs for 10 systems. The validity of Anderson's rule to describe band alignments and band gaps is vdW heterostructures is discussed more deeply in the next chapter.

4.4.1 Screening of monolayers for solar energy harvesting

TMD monolayers and vdW heterostructures are promising candidates to develop solar cells with high power per mass ratio.[55,140,141] Therefore, there is interest in finding novel candidate materials for this application, in particular semiconductor heterojunctions with type-II band alignments, because of the decreased recombination rate of charge carriers caused by spatial separation of electron and holes. To screen materials for use in photovoltaic devices, several properties must be taken into account, and here, as a first step to perform the screening on the studied TMD monolayers, the power conversion efficiency (PCE)[55] is the only parameter employed. The PCE of the type-II junctions was evaluated following a widely used approach for screenings of vdW heterostructures reported in the literature,[29,62] which estimates an upper limit for the PCE (η) by[142,143]

$$\eta = \frac{0.65(E_g^{\mathrm{d}} - \Delta E_{\mathrm{CBM}} - 0.30)\int_{E_g^{\mathrm{d}}}^{\infty} \frac{P(E)}{E} dE}{\int_0^{\infty} P(E) dE} \,. \tag{4.2}$$

In this expression, a value of 0.65 is adopted for the solar cell fill factor, based on measurements of optimized devices. The open-circuit voltage is estimated by the term in parentheses, where E_g^{d} is the band gap of the material with higher VBM (donor), ΔE_{CBM} is the conduction band offset, and 0.30 is an empirical factor that accounts for losses

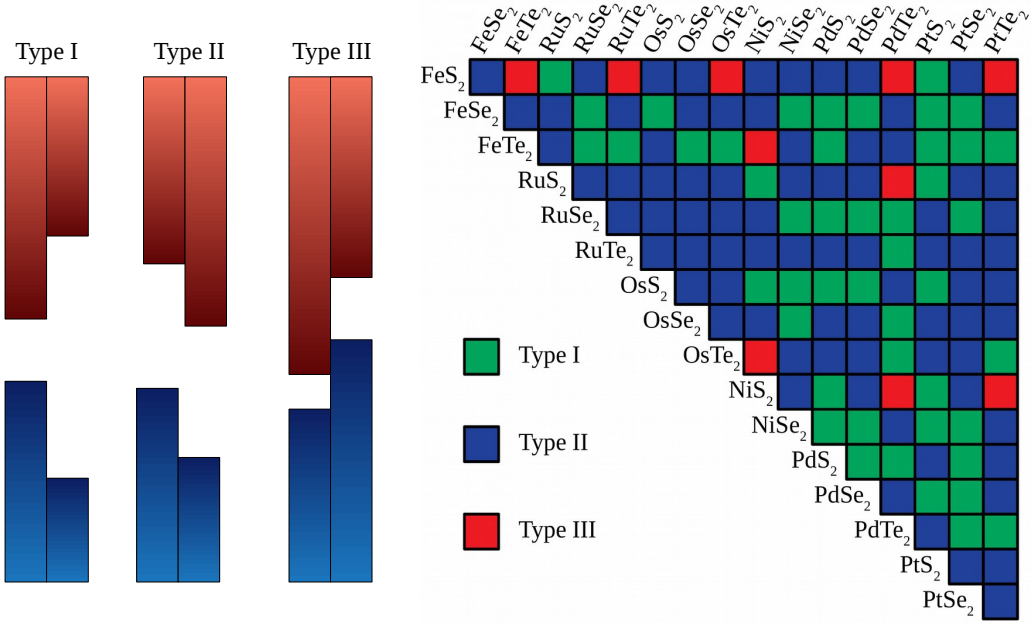

Figure 15 – Scheme indicating the types I, II, and III of semiconductor heterojunctions, and the classification of junctions formed with the semiconductor monolayers from Fe- and Ni-groups TMDs. The classification was performed based on Anderson's rule and employed the energy levels calculated with the HSE06 functional.

Source: Adapted from BESSE; LIMA; DA SILVA.[118]

due to energy conversion kinetics. The integral in the numerator gives the short circuit current, assuming 100 % external quantum efficiency, that is, all photons that shine on the solar cell generate charge carriers. $P(E)$ is the flux of energy from solar radiation, which is divided per energy in the integral to obtain the number of charge carriers, and its integration in the denominator results in the total incident solar power per area. This is a simple approach, where only the donor band gap and conduction band offset affect the PCE, and the purpose of its use here is mainly to compare the PCE results with those of other TMD systems whose performance in photovoltaic devices have been more deeply examined.

The PCE estimates for monolayers pairs with type-II junction are presented in Table 4, where only systems with $E_g^{\mathrm{d}} - \Delta E_{\mathrm{CBM}} > 0.30\,\mathrm{eV}$ are included. For instance, the highest value (22.9 %) is obtained for $RuTe_2$/OsSe2, due to the small conduction band offset (0.02 eV) and donor band gap in the optimal range for solar light absorption (1.22 eV). Photovoltaic cells with TMDs have been widely investigated with Mo- and W-dichalcogenides,[55] and employing the same model to estimate the PCE estimate for these materials with DFT-HSE06 band alignments found in the literature[74] results in efficiencies of 9 % to 20 %. Therefore, more than 30 of the studied systems fall within this PCE range or larger. This approach for PCE estimate can only serve as one preliminary criterion to

Table 4 – Power conversion efficiency (η) predicted for heterostructures of the MQ_2 monolayers with type-II band alignments, ordered in decreasing η. The model for calculation is discussed in the text, and employed band edge positions calculated with HSE06. Only heterojunctions with effective band gap higher than 0.30 eV are included.

Monolayers	η (%)	Monolayers	η (%)	Monolayers	η (%)
$RuTe_2/OsSe_2$	22.92	$PtTe_2/PtSe_2$	13.80	$NiSe_2/RuS_2$	7.46
$RuTe_2/PdS_2$	21.24	$PtSe_2/OsS_2$	13.43	$FeSe_2/FeS_2$	7.37
$PtTe_2/RuTe_2$	21.23	$PtTe_2/RuSe_2$	12.78	$RuTe_2/OsS_2$	7.19
$PtTe_2/OsSe_2$	20.78	$RuTe_2/PtS_2$	12.69	$OsSe_2/RuS_2$	7.18
$OsSe_2/PdS_2$	20.19	$PdSe_2/NiS_2$	12.64	$PtSe_2/FeS_2$	6.42
$PdSe_2/RuS_2$	20.16	$RuSe_2/RuS_2$	11.69	$RuSe_2/FeS_2$	5.96
NiS_2/FeS_2	19.36	$OsSe_2/OsS_2$	11.24	$PdTe_2/PtS_2$	5.38
$FeSe_2/RuS_2$	19.31	$FeSe_2/NiS_2$	11.17	$PdTe_2/FeTe_2$	5.08
$PtTe_2/PdS_2$	18.85	OsS_2/FeS_2	11.07	PdS_2/FeS_2	4.91
$RuSe_2/PtS_2$	18.72	PdS_2/PtS_2	10.88	$FeTe_2/OsS_2$	3.39
$OsSe_2/PtSe_2$	17.39	$OsTe_2/PtSe_2$	10.78	$OsTe_2/OsS_2$	3.35
OsS_2/RuS_2	17.22	$PtSe_2/RuS_2$	10.65	$RuTe_2/PdSe_2$	3.09
$RuTe_2/PtSe_2$	16.85	$OsTe_2/RuSe_2$	10.10	$OsSe_2/NiS_2$	2.98
$OsSe_2/RuSe_2$	16.83	$PdSe_2/FeS_2$	9.13	$RuTe_2/FeSe_2$	2.96
$RuTe_2/RuSe_2$	15.96	$PtTe_2/PtS_2$	9.02	$PtTe_2/OsS_2$	2.70
$PtSe_2/PtS_2$	15.83	$OsSe_2/PdSe_2$	8.63	$RuTe_2/NiSe_2$	2.32
$OsTe_2/RuTe_2$	15.76	$OsSe_2/FeSe_2$	8.54	$OsSe_2/FeS_2$	1.02
$RuSe_2/OsS_2$	15.46	$RuSe_2/NiS_2$	7.79	$RuTe_2/RuS_2$	0.82
$OsTe_2/OsSe_2$	15.46	$PtSe_2/NiS_2$	7.77	$OsTe_2/PdSe_2$	0.20
$OsSe_2/PtS_2$	14.74	PdS_2/RuS_2	7.59	$OsTe_2/FeSe_2$	0.09
$OsTe_2/PdS_2$	14.17	$OsTe_2/PtS_2$	7.58		

Source: By the author.

select 2D materials to design junctions for solar cells, because the PCE can be influenced by properties not taken into account in the model, such as light absorption coefficient, whose accurate evaluation requires the inclusion of many-body effects. Furthermore, other factors can affect the operation of devices, not to mention other relevant criteria for the selection of materials, such as availability, cost, and environmental impact. Therefore, further investigations are necessary in order determine the potential for application of the candidate materials.

4.5 Summary

Equilibrium geometries of the 36 MQ_2 TMDs compounds with M = Fe, Co, Ni, Cu, Co, Ru, Rh, Pd, Ag, Os, Ir, Pt, and Au; and Q = S, Se, and Te were obtained for 11 crystal structures with layered (2D) and non-layered (3D) frameworks. The analysis of the relative stability based on the total energy showed that layered structures are the most

stable among Ni-group TMDs. Among the 2D structures, the octahedral coordination is more energetically favored: distorted octahedral 1T′ geometry for the Fe-group compounds, and the 1T or calaverite geometry for the remaining compounds, plus the crystal structure of PdS_2. The analysis of interlayer binding of the lowest energy 2D structures indicated that Fe- and Ni-groups materials have the most easily exfoliable crystals due to low exfoliation energy, in which interlayer binding is dominated by weak vdW interactions. However, high exfoliation energies are found among the other materials, pointing to important role of chemical bond in interlayer interactions, as also evidenced by the analysis of the role of dispersion energy term in the exfoliation energy, and of the electron localization function. Among the lowest energy monolayers, 17 semiconductor monolayers were identified, namely the 1T′ monolayers of the Fe-group and the Ni-group TMDs, except $NiTe_2$, which are mostly 1T/calaverite monolayers. The band offsets trends of these monolayers can be understood based on the orbital composition of band edge states, and the mechanism of level repulsion. Based on the band offsets and assuming the validity of Anderson's rule, band alignments types were classified, and type-II junctions were selected for the screening of power conversion efficiency, and this parameter revealed several promising candidates for solar cells among the studied materials.

5 INTERLAYER COUPLING EFFECTS ON THE BAND GAP OF VAN DER WAALS HETEROBILAYERS

Studies for the theoretical design of vdW heterostructures have widely employed Anderson's rule to predict electronic band alignments and band gaps, because of the weak interlayer binding. However, the electronic structure of layered systems can be sensitive to interlayer coupling effects. Therefore, it is fundamental to develop a deep understanding of these effects to improve the description of band gaps in vdW heterostructures. This chapter discusses the structural, energetic, and electronic properties of vdW heterobilayers composed of TMD MQ_2 monolayers (M = Mo, Ni, Pt; Q = S, Se). The main interest is on the understanding of interlayer coupling effects on the heterobilayers band gap beyond Anderson's rule.

5.1 Structural and electronic properties of monolayers

For the study of heterobilayers, a single monolayer phase was selected for each MQ_2 compound, based on the lowest energy phases discussed in the previous chapters: the 2H phase was selected for the MoQ_2 compounds, and the 1T phase was selected for NiQ_2 and PtQ_2. The equilibrium lattice parameters, as well as the VBM and CBM with respect to vacuum level, and the band gap of these monolayers at the DFT-PBE level are presented in Table 5. All monolayers are semiconductors, with band gaps ranging from 0.14 eV to 1.79 eV, and their heterobilayers are also expected to have non-zero band gaps, based on the difference between the lowest CBM and the highest VBM of each pair of monolayers, except for NiS_2/$NiSe_2$, since the VBM of $NiSe_2$ is higher than the CBM of NiS_2. Therefore, the selected systems comprise an interesting set to examine the role of interlayer coupling on the heterobilayers band gaps.

The mechanisms of interlayer coupling are largely influenced by the features of the

Table 5 – Equilibrium structural and electronic properties of the MQ_2 monolayers (M = Mo, Ni, Pt; Q = S, Se) obtained with PBE+D3: lattice parameter (a_0), VBM and CBM with respect to vacuum level, and band gap (E_g).

Monolayer	a_0 (Å)	VBM (eV)	CBM (eV)	E_g (eV)
2H-MoS_2	3.17	−5.93	−4.19	1.74
2H-$MoSe_2$	3.30	−5.29	−3.77	1.52
1T-NiS_2	3.33	−5.77	−5.20	0.57
1T-$NiSe_2$	3.52	−4.96	−4.82	0.14
1T-PtS_2	3.56	−6.37	−4.58	1.79
1T-$PtSe_2$	3.72	−5.67	−4.32	1.35

Source: BESSE *et al.*[144]

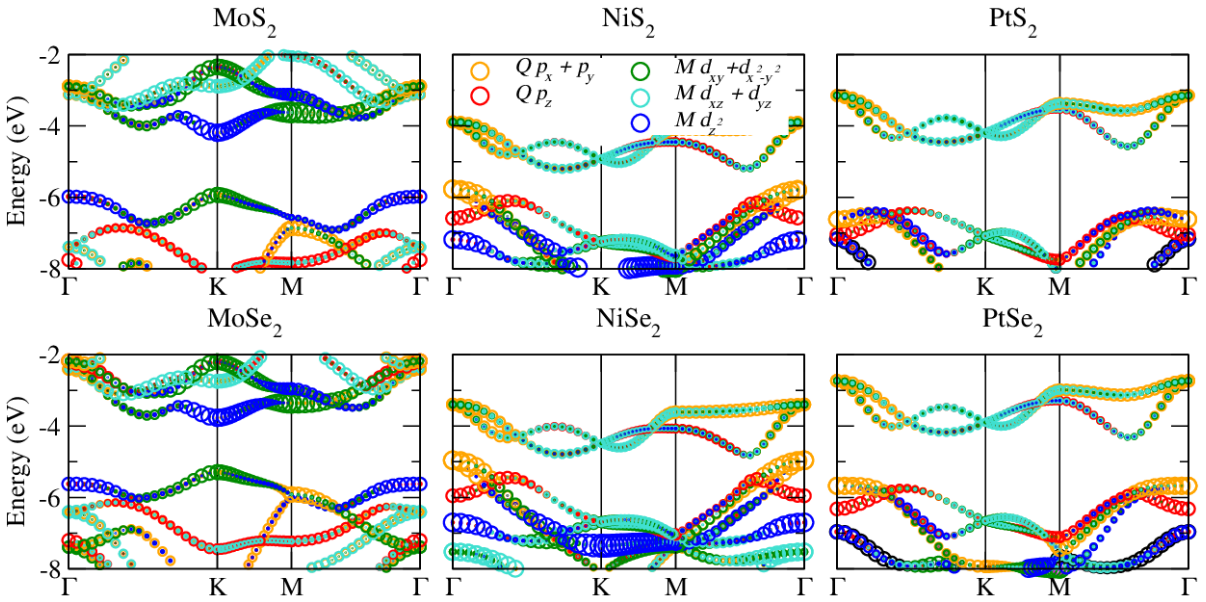

Figure 16 – Electronic band structures of the MQ_2 monolayers(M = Mo, Ni, Pt; Q = S, Se). The local projection onto angular momentum states is indicated by the size of the colored circles, and the vacuum level is adopted as energy reference.

Source: By the author.

monolayer wave functions, considering for instance the important role of p_z states, that are delocalized in the interlayer region.[64,65] The band structures of the MQ_2 monolayers are shown in Figure 16, where the local projection onto angular momentum states is indicated. Aside from the differences in the dispersion of the bands, the 2H and 1T monolayers also have important differences in the wave function features of band edges. For instance, in the 2H monolayers, there are two almost degenerated VBM states, one mostly composed of Mo d_{z^2}- and Q p_z-states at Γ, and one at K composed mainly of the in-plane Mo d_{xy}- and $d_{x^2-y^2}$-, and Q p_x- and p_y-states. On the other hand, in the 1T monolayers, the VBM at Γ is composed primarily of Q p_x- and p_y-states, and a lower-lying band at Γ, which is the topmost valence band in the Γ–K and Γ–M lines, has a high contribution from out-of-plane Q p_z-states. Given the important role of out-of-plane p_z states, such differences can influence the interlayer coupling upon heterobilayer stacking. Furthermore, in both monolayers phases, it can be seen that the VBM has predominant contribution of Q p_z-states, and the conduction band has a higher contribution from M d-states.

5.2 Heterobilayers equilibrium structural properties and interlayer binding

The representation of the structures of systems with periodic boundary conditions is an evident choice for crystals, but its application has some particularities for the vertically stacked vdW heterostructures. In these systems, the structures of different monolayers must be defined by the same set of lattice vectors. For two stacked monolayers

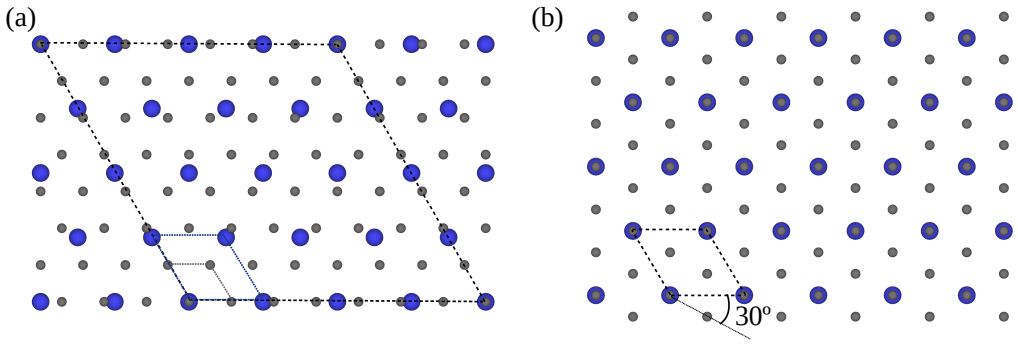

Figure 17 – (a) Depiction of two hexagonal lattices with a 4 : 3 lattice parameter ratio, distinguished by the color and size of circles that represent lattice points. The dashed lines indicate the cells, including a common supercell for both lattices. A common cell containing one unit of the larger cell can be obtained if a small strain is employed. (b) In this case, one of the lattices is rotated by 30°, allowing to obtain a smaller common supercell, with a strain of around 0.5 % in both lattices.

Source: By the author.

with same type of lattice, as in the systems studied herein, one first approach is applying strain on both monolayers so that both lattice parameters are made to coincide. However, large strains should be avoided, because the original electronic properties of the monolayers, such as band alignments and bands gaps, can be severely modified. Within the set of monolayers investigated, lattice parameters mismatches between monolayers range from 0.9 % to 17.3 %, which indicates that generating unit cells to model the heterobilayers by simply stacking strained monolayers unit cells is not a viable approach for all possible the 15 heterobilayers. As an alternative, lattice parameters a and b of monolayers A and B must be be commensurate, or forced to be so by application of strain, to allow the construction of a common unit cell with lattice parameter c such that $c = Pa = Qb$, with P and Q integers, as shown in Figure 17(a). One limitation of the approach is that depending on the magnitudes of the integers P and Q, the size of the supercell can be prohibitively large to perform the calculations. An additional degree of freedom to be introduced that can help to reduce the size of the commensurate cell is an interlayer twist between the two monolayer lattices, with a relative angle between the correspondent lattice vectors of each monolayer, as exemplified Figure 17(b).

The search for matching cells was performed with the *CellMatch* software,[145] which allows to systematically screen interlayer rotations and control the maximum number of atoms in the supercell and the largest strain in the monolayers. In the search, matching heterobilayer unit cells were allowed to have up to 100 atoms, and a maximum 1.5 % strain on each monolayer. This approach was adopted to obtain all heterobilayers cells, even though some pairs of monolayers have small lattice mismatches that would yield small

Table 6 – Matching monolayer supercells found for the vertical stacking of the MQ_2 monolayers (M = Mo, Ni, Pt; Q = S, Se). The relation between each monolayer supercell and the unit cell is presented in Wood's notation. The number of atoms in the heterobilayer unit cell (N_{at}), its lattice parameter (a) and corresponding strain in each monolayer lattice (ϵ_i) are presented.

L_1/L_2	Monolayer 1	Monolayer 2	N_{at}	a(Å)	ϵ_i(%)
$MoS_2/MoSe_2$	$(\sqrt{13}\times\sqrt{13})$R13.9°	$(\sqrt{12}\times\sqrt{12})$R30.0°	75	11.42	0.0
MoS_2/NiS_2	$(\sqrt{13}\times\sqrt{13})$R13.9°	$(\sqrt{12}\times\sqrt{12})$R30.0°	75	11.47	±0.5
$MoS_2/NiSe_2$	(3×3)	$(\sqrt{7}\times\sqrt{7})$R19.1°	48	9.40	∓1.1
MoS_2/PtS_2	(3×3)	$(\sqrt{7}\times\sqrt{7})$R19.1°	48	9.46	∓0.4
$MoS_2/PtSe_2$	(2×2)	$(\sqrt{3}\times\sqrt{3})$R30.0°	21	6.39	±0.9
$MoSe_2/NiS_2$	$(\sqrt{7}\times\sqrt{7})$R19.1°	$(\sqrt{7}\times\sqrt{7})$R19.1°	42	8.76	±0.5
$MoSe_2/NiSe_2$	$(\sqrt{13}\times\sqrt{13})$R13.9°	$(\sqrt{12}\times\sqrt{12})$R30.0°	75	12.03	±1.3
$MoSe_2/PtS_2$	(4×4)	$(\sqrt{13}\times\sqrt{13})$R13.9°	87	13.01	∓1.3
$MoSe_2/PtSe_2$	(2×2)	$(\sqrt{3}\times\sqrt{3})$R30.0°	21	6.52	∓1.1
$NiS_2/NiSe_2$	$(\sqrt{13}\times\sqrt{13})$R13.9°	$(\sqrt{12}\times\sqrt{12})$R30.0°	75	12.09	±0.7
NiS_2/PtS_2	$(\sqrt{13}\times\sqrt{13})$R13.9°	$(\sqrt{12}\times\sqrt{12})$R30.0°	75	12.17	±1.4
$NiS_2/PtSe_2$	(3×3)	$(\sqrt{7}\times\sqrt{7})$R19.1°	48	9.92	∓0.7
$NiSe_2/PtS_2$	$(\sqrt{7}\times\sqrt{7})$R19.1°	$(\sqrt{7}\times\sqrt{7})$R19.1°	42	9.36	±0.7
$NiSe_2/PtSe_2$	$(\sqrt{13}\times\sqrt{13})$R13.9°	$(\sqrt{12}\times\sqrt{12})$R30.0°	75	12.78	±0.9
$PtS_2/PtSe_2$	$(\sqrt{13}\times\sqrt{13})$R13.9°	$(\sqrt{12}\times\sqrt{12})$R30.0°	75	12.87	±0.2

Source: BESSE *et al.*[144]

strain with the simple 1×1 stacking of monolayers cells, such as $MoSe_2$ with $NiSe_2$, and $NiSe_2$ with PtS_2. This was done to enable a general description of the interlayer coupling throughout all heterobilayers, because, in contrast with the 1×1 cells, the generated vertical stacking configurations are not restricted to symmetric stackings, which exhibit the strongest interlayer coupling for specific TMD systems.[146] The heterobilayers matching cells are described in detail in Table 6, where Wood's notation[147] is used to denote the relation between monolayers supercells and unit cells, e.g., $(\sqrt{13}\times\sqrt{13})$R13.9° means that the cell has lattice parameter $\sqrt{13}$ times larger than the original unit cell and is rotated by 13.9° with respect to it.

The equilibrium structural configurations of the heterostructures were obtained by minimization of the stress tensor, allowing relaxation of in-plane lattice parameters cells, and of forces on every atom. Structural parameters are presented in Table 7 along with corresponding monolayer strains, which have magnitudes no larger than 1.8 %. Lattice parameters were only slightly affected by the relaxation, with changes smaller than 0.5 % in all systems, except for $NiS_2/NiSe_2$, in which the change was of 1.08 %. In light of the weak interlayer binding, these variations can be attributed merely to a redistribution of strain among the monolayers, since the initial configuration had strains with the same magnitude in both monolayers, but they have different energy responses to strain. To better describe

Table 7 – Equilibrium lattice parameters of heterobilayers (a_0), strains in the two monolayer lattices (ϵ_i), equilibrium interlayer distances (d), interlayer binding energies (E_b), lattice parameters that minimize strain energy (a_s), and monolayer effective charges (Q_i) obtained with Bader charge analysis. The results were obtained from calculations with PBE+D3.

L_1/L_2	a_0(Å)	ϵ_1(%)	ϵ_2(%)	d(Å)	E_b(meV/Å^2)	a_s(Å)	Q_1 (e/f.u.)	Q_2 (e/f.u.)
$MoS_2/MoSe_2$	11.41	−0.1	0.0	3.33	24.20	11.41	−0.01	0.01
MoS_2/NiS_2	11.47	0.5	−0.5	3.18	16.16	11.46	0.00	0.00
$MoS_2/NiSe_2$	9.44	−0.7	1.5	3.26	22.39	9.43	−0.01	0.01
MoS_2/PtS_2	9.47	−0.3	0.5	3.22	21.93	9.47	0.00	0.00
$MoS_2/PtSe_2$	6.38	0.7	−1.1	3.24	22.72	6.37	−0.01	0.01
$MoSe_2/NiS_2$	8.76	0.5	−0.5	3.27	22.95	8.76	0.01	−0.01
$MoSe_2/NiSe_2$	12.00	1.0	−1.5	3.27	23.58	12.00	0.00	0.00
$MoSe_2/PtS_2$	13.03	−1.1	1.5	3.22	23.40	13.03	0.01	−0.01
$MoSe_2/PtSe_2$	6.53	−0.9	1.4	3.28	23.96	6.53	0.00	0.00
$NiS_2/NiSe_2$	12.22	1.8	0.3	2.38	32.29	12.08	−0.05	0.05
NiS_2/PtS_2	12.20	1.7	−1.1	2.96	21.31	12.18	−0.01	0.01
$NiS_2/PtSe_2$	9.95	−0.3	1.1	2.92	23.57	9.92	−0.02	0.03
$NiSe_2/PtS_2$	9.39	1.0	−0.3	3.04	22.85	9.37	0.01	−0.01
$NiSe_2/PtSe_2$	12.84	1.3	−0.4	2.89	24.97	12.79	−0.01	0.01
$PtS_2/PtSe_2$	12.88	0.3	−0.1	3.00	22.65	12.86	−0.01	0.01

Source: BESSE *et al.*[144]

the role of strain energy in the equilibrium lattice parameters of heterobilayers, the relative energies of the monolayers unit cells were calculated with strain ranging from −1.0 % to 1.0 %. In this range, the energy as a function of the lattice parameter can be well fitted by a quadratic relation $\Delta E = \alpha_i(a - a_{0i})^2$, where a_{0i} is the equilibrium lattice parameter, as displayed in Figure 18(a). Thus, the energy contribution from strain in a heterobilayer can be written as

$$E_{strain}(a) = \alpha_1(a - a_1)^2 + \alpha_2(a - a_2)^2 \ , \tag{5.1}$$

where a is the lattice parameter of the heterobilayer cell, and a_1 and a_2 are the equilibrium lattice parameters of the monolayers, in the supercells listed in Table 6. With this expression, the number of formula units from each monolayer (N_i) is already taken into account, since the parameters are related by $a_i = l_i a_{0i}$, and $N_i = l_i^2$. Therefore, the redistribution of strain in the monolayers is such that E_{strain} is minimized, as follows,

$$\left.\frac{dE_{strain}}{da}\right|_{a=a_s} = 0 \Rightarrow a_s = \frac{\alpha_1 a_1 + \alpha_2 a_2}{\alpha_1 + \alpha_2} \ . \tag{5.2}$$

The lattice parameters a_s obtained by this approach are close to the equilibrium lattice parameters a_0, as shown in Table 7, with mean absolute deviation of 0.02 Å, and a significant difference (0.14 Å) is observed only for $NiS_2/NiSe_2$. All subsequent analyses of

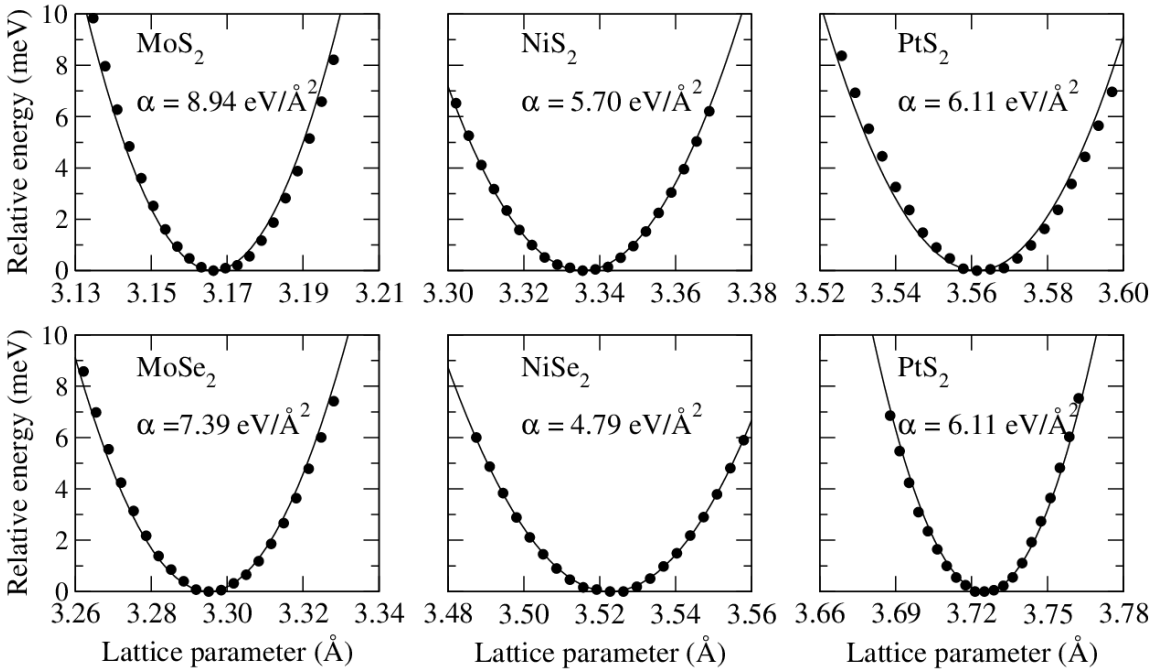

Figure 18 – Relative energy of the monolayers due to strain as a function of the lattice parameter, with strain data ranging from $-1.0\,\%$ to $1.0\,\%$ in intervals of $0.1\,\%$. The solid lines are fittings of the data by $\Delta E = \alpha_i(a - a_{0i})^2$, and the α_i coefficients are provided.

Source: By the author.

the interlayer binding and electronic properties employed the equilibrium parameters a_0 obtained via structural optimization.

The analysis of the role of the strain energy in the equilibrium lattice parameters supports the notion that the interlayer binding is ruled majorly by weak interactions, since intralayer bonds are virtually unaffected by it. This is also evidenced by the equilibrium interlayer distances (d) and interlayer binding energies (E_b) of Table 7: d ranging from 2.89 Å to 3.33 Å, and E_b from 16 meV Å^{-2} to 25 meV Å^{-2}, typical values for vdW heterostructures.[67,148,149] As occurred in the comparison between a_0 and a_s, the single system that has E_b significantly larger than the remaning is NiS_2/$NiSe_2$, which has $d = 2.38$ Å and $E_b = 32.29$ meV Å^{-2}, indicating stronger interlayer binding in this system. The contrast of NiS_2/$NiSe_2$ with the other heterobilayers can be explained by considering the band alignments, since NiS_2/$NiSe_2$ is the only system in which natural band offsets of monolayers indicate a type-III band alignment, see Table 5. This feature points to the energy overlap of occupied states in $NiSe_2$ with empty states in NiS_2, which contributes to increase interlayer charge transfer, leading to the stronger binding observed in this system. This also leads to the difference between a_0 and a_s observed in this system, because, in contrast with the remaining heterobilayers, the change of lattice parameter upon relaxation is not primarily ruled by minimization of strain energy. To obtain more information on

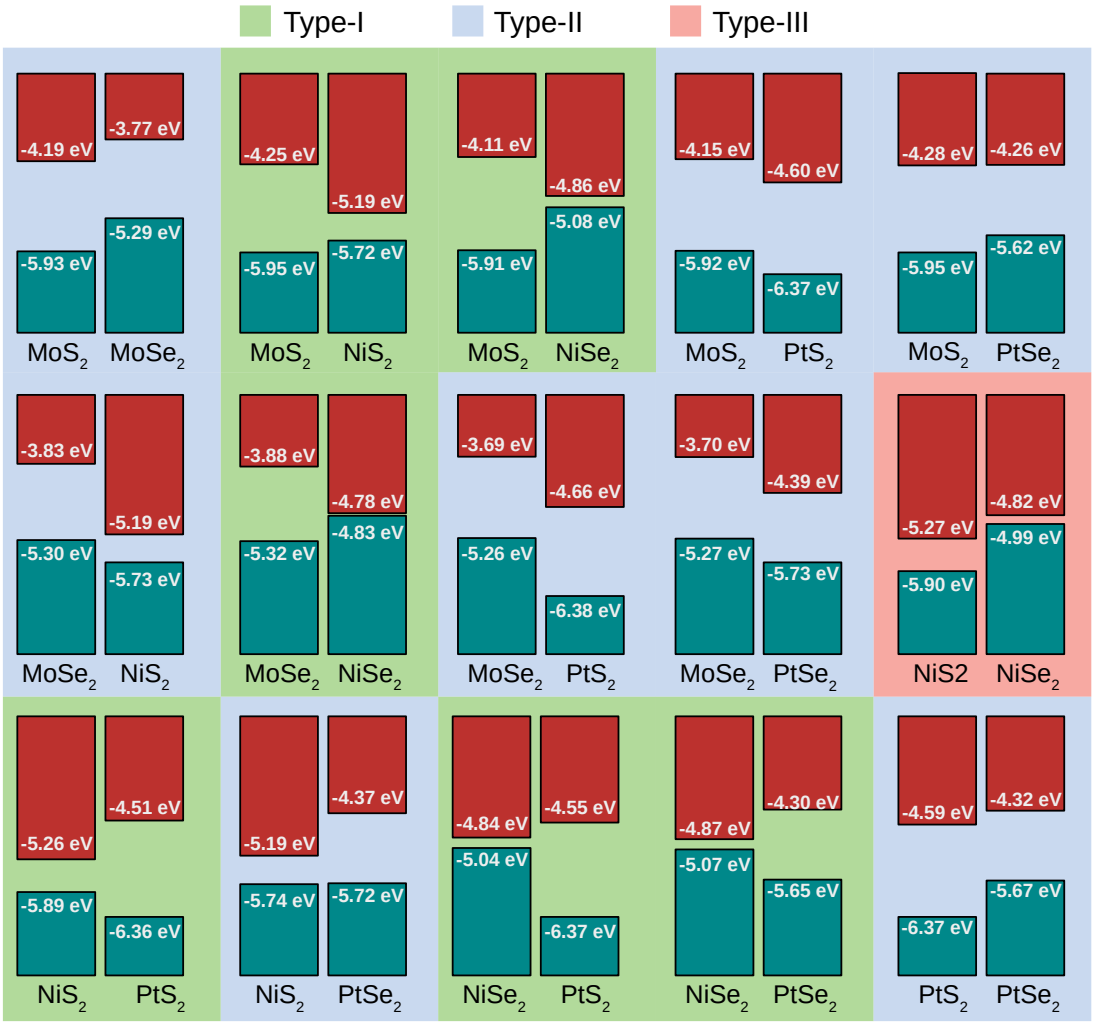

Figure 19 – PBE+D3 VBM and CBM of the MQ_2 monolayers (M = Mo, Ni, Pt; Q = S, Se), where in each pair the monolayers have the same strain they of the respective equilibrium heterobilayer configuration. Background colors indicate the junction type that results from Anderson's rule.

Source: By the author.

the interlayer charge transfer, Bader charge analysis was employed to perform the charge partition in the systems (see Section 4.3 for the description of the method). The monolayers effective charges, shown in Table 7, are the sums of the $Q_{eff,i}$ of all atoms of each monolayer. As expected, monolayer effective charges are small, and the largest magnitude of interlayer charge transfer occurs in $NiS_2/NiSe_2$, namely $0.05\,e$/f.u., in comparison with all remaining values that are at most $0.03\,e$/f.u.

5.3 Heterobilayers band gaps via Anderson's rule and direct calculation

The band edge positions of the monolayers with respect to the vacuum level, displayed in Table 5, can be employed to predict the band alignments of heterobilayers, according to Anderson's rule, as discussed in Chapter 1. However, to better describe the

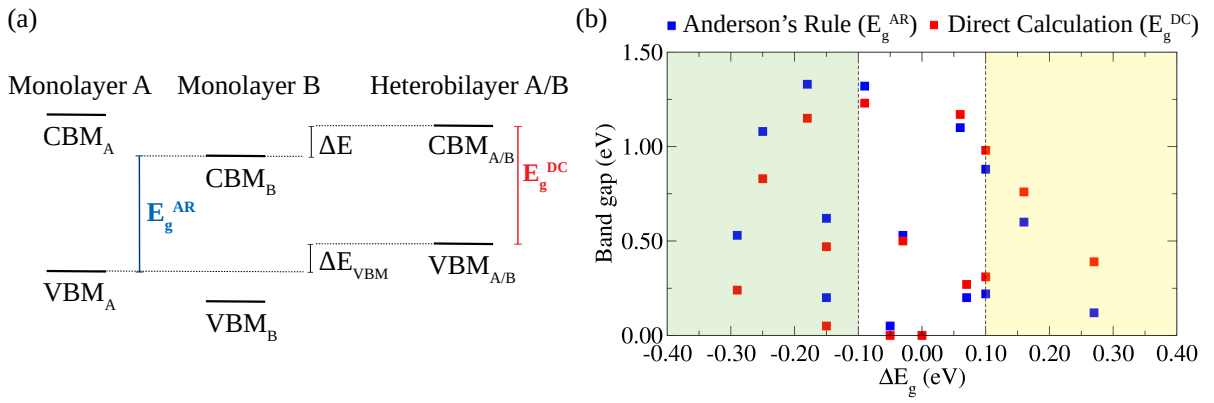

Figure 20 – (a) Representation of the band edge positions for isolated monolayers A and B, the corresponding A/B heterobilayers, and the definition of heterobilayer band gap evaluated with Anderson's rule (E_g^{AR}) and by direct calculation of the heterobilayer band structure (E_g^{DC}), which differ by shifts in the VBM (ΔE_{VBM}) and CBM (ΔE_{CBM}). (b) Values of E_g^{AR} and E_g^{DC}, as a function of $\Delta E_g = E_g^{\mathrm{DC}} - E_g^{\mathrm{AR}}$, where the color regions indicate systems for which $\Delta E_g < -0.10\,\mathrm{eV}$ on the left (green), and systems for which $\Delta E_g > 0.10\,\mathrm{eV}$ on the right (yellow).

Source: Adapted from BESSE *et al.*[144]

heterobilayers configurations, the strain on the monolayers should also be considered. Therefore, Figure 19 shows the VBM and CBM with respect to vacuum level of the monolayers pairs with the same strain of the equilibrium configuration of the respective heterobilayers. These results can be compared with those displayed in Table 5, showing that band edge shifts of up to 0.13 eV are caused by strain. However, the band alignment classifications, indicated by the background color in Figure 19, are not changed by strain, except for $MoS_2/PtSe_2$, which changes from type-I to type-II, due to the small conduction band offset between the monolayers. Type-I band alignment is found in 6 systems, type-II in 8, and type-III occurs only in $NiS_2/NiSe_2$.

With the monolayers band offsets displayed in Figure 19, band gaps of heterobilayers can be calculated based on Anderson's rule. Assuming the same vacuum level alignment for both monolayers, Anderson's rule band gap (E_g^{AR}) is given by the difference between the lowest CBM and highest VBM among both monolayers, as depicted in Figure 20(a). For systems with type-I band alignment, the band gap is the same as one of the monolayers, and type-II band alignment yields an interlayer band gap. These band gap values can be contrasted with E_g^{DC}, obtained from direct calculations of the heterobilayers band structures, which are all shown in Appendix C. The E_g^{AR} and E_g^{DC} for the 15 heterobilayers are listed in Table 8, and the comparison between them is displayed in Figure 20(b). It is observed that for 7 heterobilayers both values differ by less than 0.10 eV, but in the other systems, represented in the regions with colored background in

Table 8 – Heterobilayers band gaps evaluated employing Anderson's Rule (E_g^{AR}), for isolated monolayers with same strain as in heterobilayers, and via the direct calculation of heterobilayers band structures (E_g^{DC}).

Heterobilayer	E_g^{AR} (eV)	E_g^{DC} (eV)
$MoS_2/MoSe_2$	1.10	1.17
MoS_2/NiS_2	0.53	0.50
$MoS_2/NiSe_2$	0.22	0.31
MoS_2/PtS_2	1.32	1.23
$MoS_2/PtSe_2$	1.33	1.15
$MoSe_2/NiS_2$	0.12	0.39
$MoSe_2/NiSe_2$	0.05	0.00
$MoSe_2/PtS_2$	0.60	0.76
$MoSe_2/PtSe_2$	0.88	0.98
$NiS_2/NiSe_2$	0.00	0.00
NiS_2/PtS_2	0.62	0.47
$NiS_2/PtSe_2$	0.53	0.24
$NiSe_2/PtS_2$	0.20	0.27
$NiSe_2/PtSe_2$	0.20	0.05
$PtS_2/PtSe_2$	1.08	0.83

Source: BESSE *et al.*[144]

the figure, the difference between the two values, $\Delta E_g = E_g^{\mathrm{DC}} - E_g^{\mathrm{AR}}$, can have magnitude of up to 0.28 eV.

The results show that although Anderson's rule can describe the band gap of some heterobilayers with fairly good accuracy, interlayer coupling can play a significant role, and therefore, it is not negligible in general. As indicated in Figure 20(a), the role of interlayer coupling in the band gap can be linked to effects on valence or conduction band edges. Furthermore, the heterobilayers with significant ΔE_g can be divided into two subgroups, as indicated by the colored regions in Figure 20(b), that is, systems for which $\Delta E_g < -0.10$ eV, and systems for which $\Delta E_g > 0.10$ eV. Such contrasting trends suggest that different mechanisms may participate in the total effect of interlayer coupling on the band gap. The evaluations of E_g^{AR} employed monolayers with the same strain as in the equilibrium configuration of heterobilayers, so that the interlayer coupling effects on ΔE_g can be investigated separately from possible effects of strain.

5.4 Interlayer hybridizations

The systems for which $\Delta E_g < -0.10$ eV are mostly those composed of two 1T monolayers, that is, the heterobilayers with M = Ni and Pt, except for $NiS_2/NiSe_2$ and $NiSe_2/PtS_2$. Figure 21(a) shows the electronic band structures of the constituent monolayers and of the heterobilayer for the representative 1T-NiS_2/1T-PtS_2 system. The band

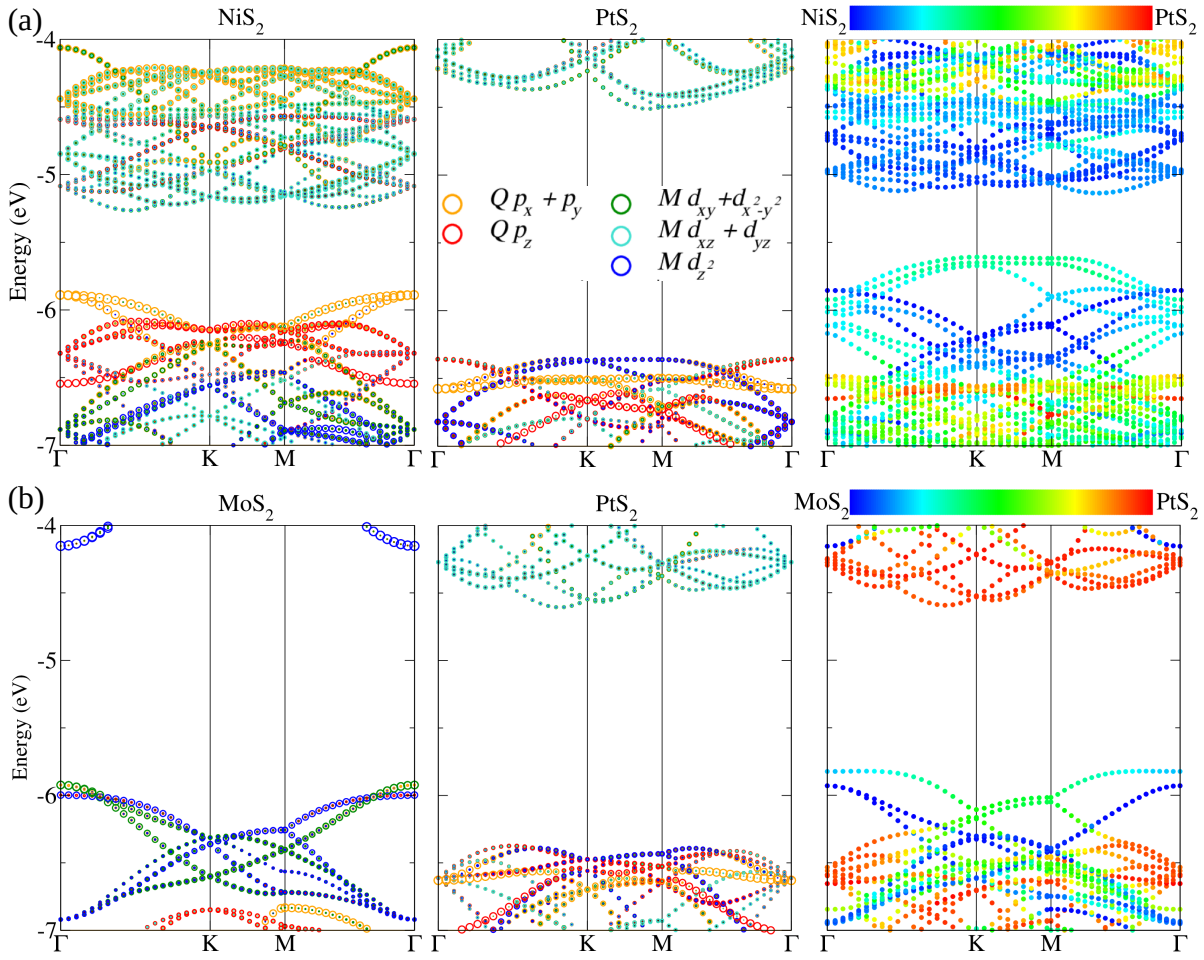

Figure 21 – (a) Band structures of the (a) 1T-NiS_2/1T-PtS_2 and (b) 2H-MoS_2/1T-PtS_2 heterobilayers, and of the respective isolated monolayers in the same supercell of the heterobilayers. For the monolayers, local projection onto angular momentum states is indicated by the size of the colored circles, and energy is given with respect to the vacuum level. For the heterobilayers, the color scale denotes the local projection onto each monolayer, and the zero energy level is adopted as the average of the vacuum electrostatic potential on the two sides of the cell.

Source: Adapted from BESSE *et al.*[144]

structures of monolayers correspond to the same supercell of the heterobilayer, to enable a direct comparison between them. From the top of the valence band, it is clear that the heterobilayer band structure differs from a superposition of the monolayers band structures. The VBM of the heterobilayer is located along the K-M line of the Brillouin zone, and has a different dispersion in comparison with the monolayers. Furthermore, the heterobilayer VBM is located above the original VBMs of the monolayers, visible in the heterobilayer band structure, and is delocalized over the two monolayers, as can be seen by the color scale in the plot, which measures the local projection of electron states onto each monolayer. These features suggest that the heterobilayer VBM arises from the

hybridization of lower-lying states of the monolayers, in particular, the bands composed primarily of anion p_z-states, whereas the original NiS_2 VBM is primarily composed of in-plane Q p_x- and p_y-states. Therefore, the negative deviation of the band gap in comparison with Anderson's rule can be attributed to the VBM upshift caused by interfacial hybridizations.

A similar picture can be observed in the 2H-MoS_2/1T-PtS_2 heterobilayer, shown in Figure 21(b). Here, a VBM upshift occurs primarily at the Γ point of the Brillouin zone and arises from the interaction of the hybridized Mo d_{z^2}- and S p_z-states close to the VBM of MoS_2, and lower-lying S p_z-states of PtS_2. Thus, the examples of 1T-NiS_2/1T-PtS_2 and 2H-MoS_2/1T-PtS_2 illustrate the role of the interfacial hybridizations in ΔE_g, which can be summarized by the scheme of Figure 22(a). Since Q p_z-states extend into the out-of-plane direction, they have the strongest effect upon layer stacking, and in the 2H phase the topmost Q p_z-states are hybridized with M d_{z^2}-states. The band splittings that occur due to these interfacial hybridizations can lead to a VBM upshift and corresponding decrease of the band gap, provided that the splitting (E_s) is larger than the energy distance (α) of the interacting states to the original VBM of the monolayers, which is generally composed of in-plane states, that do not show significant interlayer interactions.[64,65] The magnitude of the band splitting is influenced by the energy difference of interacting states (ΔE) resembling the energy splitting relation of molecular orbital theory,[150] $E_s = 1/(a + b\Delta E)$, as displayed in Figure 22(b). The ΔE and E_s parameters in this plot were measured at the M point for 1T/1T heterobilayers, and at Γ point for 2H/2H and 2H/1T, since these are the points where splittings are more noticeable, due to the location of the interacting p_z states in the Brillouin zone.

In contrast with the important effect of interfacial hybridizations on the VBM upshift, the conduction bands of the heterobilayers are not as strongly affected by the interlayer coupling. This can be attributed to the predominance of the contribution of M d-states in the monolayers conduction bands, as discussed in Section 5.1, because these states are mostly localized far from the interfacial region and are weakly influenced by interlayer coupling. A significant effect on the conduction band, with downshift of the CBM, was found only in PtS_2/$PtSe_2$, the 1T/1T heterobilayer with the smallest conduction band offset of the monolayers (0.27 eV). Therefore, interfacial hybridizations mainly influence ΔE_g by the effect on the valence band. However, the VBM upshift, given by $E_s - \alpha$ as seen in Figure 22(a), corresponds to ΔE_g in few systems, namely MoS_2/PtS_2, NiS_2/PtS_2, and $NiSe_2$/$PtSe_2$, within a 0.02 eV margin. Thus, this effect does not account entirely for ΔE_g in all systems and other effects can play an important role, as evident by the cases in which $\Delta E_g > 0$, particularly the heterobilayers with $\Delta E_g > 0.10$ eV, namely $MoSe_2$/NiS_2 and $MoSe_2$/PtS_2, as shown in Figure 20(b).

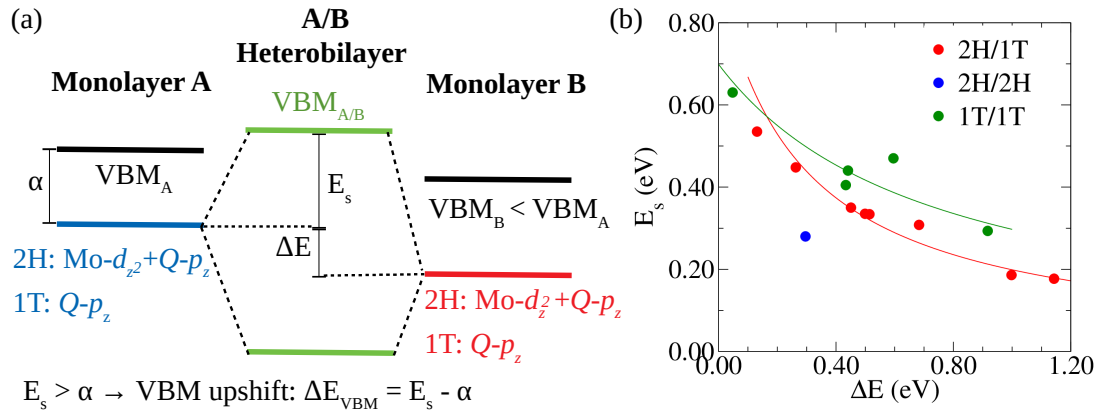

Figure 22 – (a) Schematic representation of the valence band upshift due to interlayer hybridization, where the states associated with hybridizations of each monolayer phase are indicated. (b) Values of ΔE and E_s, evaluated at the M point for 1T/1T heterobilayers, and at the Γ point for 2H/1T and 2H/2H. Solid lines are fittings with form $E_s = 1/(a + b\Delta E)$ for each set of points.

Source: Adapted from BESSE *et al.*[144]

5.5 Interfacial dipole

Beyond interlayer hybridizations, ΔE_g also has contributions from the interfacial electric dipole formed by the contact of two monolayers. The dipole causes a relative shift between levels localized in different monolayers, and therefore, it leads to a contribution to ΔE_g in systems with type-II band alignments, since intralayer band gaps, which define E_g in systems with type-I junction, are not changed by the dipole. Thus, in type-II junctions, the total ΔE_g is the result of contributions from interfacial hybridization and dipole. This can be understood based on the scheme of Figure 20(a): as the shift due to hybridization (ΔE_{VBM}) is measured with respect to the original VBM of monolayer A, in the absence of hybridization effects in the conduction band, ΔE_{CBM} is the shift of the CBM of monolayer B with respect to this level, given by the dipole induced shift (D). Therefore, it is expected that

$$\Delta E_g = D - \Delta E_{\mathrm{VBM}} \ , \tag{5.3}$$

for heterobilayers with type-II junction. The dipole term in ΔE_g comes from Anderson's rule assumption of the same vacuum level alignment on both sides of the junction. The approximation may keep some degree of validity for weakly interacting systems if the interfacial dipole is small.

To verify if (5.3) is satisfied, D was measured as the step of the electrostatic potential in the vacuum region of cell, introduced to correct the asymmetry of the electrostatic potential in the periodic systems.[151] The results are displayed in Figure 23, which show that the expected relation has good validity, except for $PtS_2/PtSe_2$, due to the hybridization effect on the CBM, as previously discussed. Although the band offsets of Figure 19

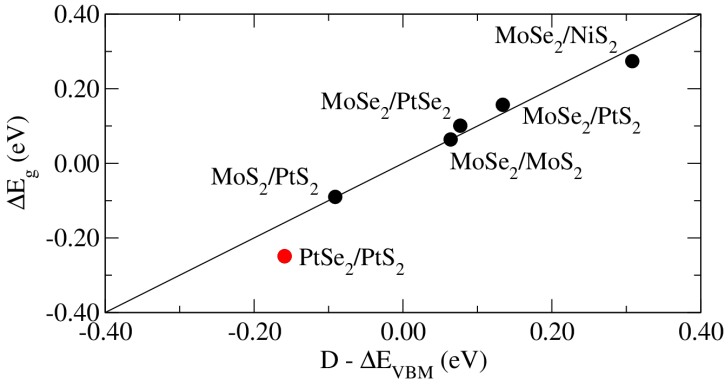

Figure 23 – Band gap deviation from Anderson's rule versus the difference between the energy shift due to the interfacial dipole and valence band upshift caused by interlayer hybridization, for systems with type-II band alignment. In the A/B nomenclature of each monolayer, the CBM is on monolayer B.

Source: Adapted from BESSE *et al.*[144]

indicate that $MoS_2/PtSe_2$ and $NiS_2/PtSe_2$ form type-II junctions, they have small offsets of conduction bands and valence bands, respectively, with differences of 0.02 eV. Because of that, with the shift introduced by the interfacial dipole, they adopt type-I band alignment, and their $\Delta E_g < 0$ comes entirely from the VBM upshift caused by hybridization.

The previous analysis shows a significant magnitude of energy shift due to the interfacial dipole, despite the weak interlayer binding. To describe the origin of the electric dipole across the interface, a simple model can be proposed, assuming that, in view of the weak interlayer coupling, the dipole arises solely from a perturbation of the charge density outside the monolayers upon the formation of the contact. Here, the charge density is described by a single band edge state in a potential barrier, such as depicted in Figure 24(a) for monolayer A. The wave function decays exponentially, with decay constant $k = \sqrt{2(E-V)}$, where E is the energy of the electron state and V is the potential in the region. In the case of the isolated monolayer A, V is the vacuum potential and $E - V$ is the difference between VBM of A and the vacuum level, or the ionization potential of A (ϕ_A), and $\psi_A(z) \propto e^{-z\sqrt{2\phi_A}}$, on both sides of the monolayer. In contact with the other monolayer, the potential outside monolayer A changes to the energy of the lowest available state, which is the CBM of B, and thus V in this case is the electron affinity of monolayer B (χ_B), yielding $\psi'_A(z) \propto e^{-z\sqrt{2(\phi_A-\chi_B)}}$. This change in the wave function corresponds to a change in the charge density, and the difference between the two configurations can be integrated to obtain the resulting electric dipole,

$$\begin{aligned} m_A &= -C\int_0^\infty z(e^{-2z\sqrt{2(\phi_A-\chi_B)}} - e^{-2z\sqrt{2\phi_A}})dz = -C\left(\frac{1}{\phi_A-\chi_B} - \frac{1}{\phi_a}\right) \\ &= -C\frac{\chi_B}{\phi_A(\phi_A-\chi_B)}\ , \end{aligned} \tag{5.4}$$

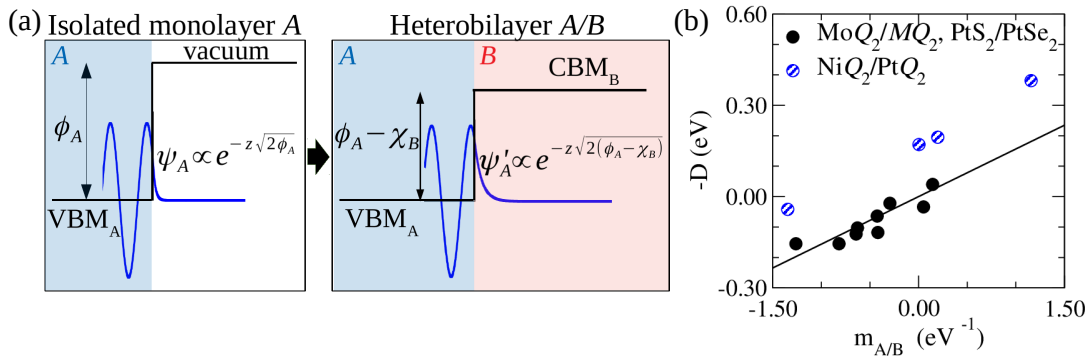

Figure 24 – (a) Schematic depiction of the change in the tail of wave function of monolayer A due to the contact with monolayer B. (b) Dipole moment factor of (5.5) versus the step of electrostatic potential in the vacuum region of the heterobilayer cells.

Source: Adapted from BESSE *et al.*[144]

where C is a positive constant. Similarly for monolayer B, $m_B = C'(\chi_A/(\phi_B(\phi_B - \chi_A)))$, and assuming $C = C'$, it follows that the total dipole moment is proportional to,

$$m_{A/B} = \frac{\chi_A}{\phi_B(\phi_B - \chi_A)} - \frac{\chi_B}{\phi_A(\phi_A - \chi_B)} \ . \tag{5.5}$$

To evaluate the magnitude of the interfacial electric dipole in the heterobilayers, the same parameter D that gives the dipole induced energy shift can be employed since it is proportional to the dipole in the cell.[151] Thus, with the same definition for the positive sign of D used in Figure 23, it is expected that $m_{A/B}$ is linearly correlated to $-D$ by a positive constant. As shown in Figure 24(b), where ϕ and χ values were obtained for strained monolayers, the linearly relationship is shown to be largely followed, irrespective of the junction type. The set of NiQ_2/PtQ_2 heterobilayers shows a slight systematic shift from the trend displayed by the remaining systems, suggesting additional electron accumulation on the NiQ_2 side, which can be attributed to the interlayer hybridizations.

Two of the heterobilayers are not included in the plot of Figure 24(b), and have large deviations from the model predictions, namely $MoSe_2/NiS_2$ and $NiS_2/NiSe_2$, for which ($m_{A/B}$,$-D$) are (-8.55,-0.32) and (-4.53,0.48), respectively. In the latter, the discrepancy is a consequence of the enhanced charge transfer of this system, as discussed in Section 5.2. As for $MoSe_2/NiS_2$, the model fails because it assumes that the wave function can be described with a single decay constant, since it describes the monolayers with semi-infinite thickness. However, $\phi_{MoSe_2} - \chi_{NiS_2}$ is very small (0.11 eV), which leads to a large decay length of charge density, and a large predicted dipole, much larger than the observed one.

5.6 Summary

The structural and electronic properties of a set of 15 heterobilayers formed of MQ_2 monolayers (M = Mo, Ni, and Pt; Q = S, Se) were studied to investigate the role of interlayer coupling on these properties. The stacked heterobilayer configurations were obtained by a search of matching monolayer supercells, allowing interlayer rotations to minimize strain and the size of the cells. Relaxation of the cells had minor effect on the lattice parameters, which can be traced to a redistribution of strain among the monolayers to minimize strain energy, because of the weak binding interlayer binding, as also suggested by the interlayer binding energies. The exception is $NiS_2/NiSe_2$, in which the type-III band alignment leads to enhanced interlayer charge transfer. Despite the weak interlayer binding, interlayer coupling effects lead to important effects on the electronic properties of the heterobilayers, as indicated by the band gap deviations of up to 0.27 eV in comparison with Anderson's rule. Two main mechanisms were found to influence the band gap deviation: (i) interfacial hybridizations that mainly involve chalcogen p_z orbitals lead to band splittings in the valence band and VBM upshifts that decrease the band gap, and (ii) the formation of the interfacial electric dipole with the monolayers contact causes a relative shift of band edges located at different sides of the interface, which affects the band gap in type-II junctions. A simple model was proposed to describe the origin of the interfacial dipole, based on the perturbation of charge density decay upon the formation of the contact. This model was able to account for a correlation between the magnitude of the interfacial dipole and the band edge positions of monolayers.

6 INTERLAYER CHARGE CARRIER TRANSFER IN $MoS_2/PtSe_2$ VERTICAL HETEROBILAYER

Because of the importance of the interfacial charge transfer process in semiconductor junctions, it is fundamental to advance in the understanding of this process, going beyond the description of band alignment and addressing other aspects such as the dynamics of charge transfer. In this chapter, the dynamics of interlayer transfer of charge carriers in excited states of vdW heterostructures is investigated with the example of the 2H-MoS_2/1T-$PtSe_2$ heterobilayer. The structural and electronic properties of the system are discussed, and based on the electronic band structure, an excitation is chosen to study the time-evolution of charge carriers occupation in the excited state and the mechanisms of interlayer transfer of electrons and holes.

6.1 Ground state configuration of $MoS_2/PtSe_2$

Based on the monolayer band offsets discussed in Chapter 5, the 2H-MoS_2 and 1T-cePtSe2 monolayers are expected to form a type-I junction, with CBM and VBM located in the $PtSe_2$ side. Therefore, an excitation across the band gap of MoS_2 is expected to induce the transfer of both electrons and holes to $PtSe_2$. The same type of band offset results from the calculations employed here, for which the VBM of $PtSe_2$ is higher than that of MoS_2 by 0.49 eV, and the CBM is lower by 0.42 eV . Equilibrium lattice parameters are also similar to the results listed in Chapter 5, and are 3.18 Å and 3.77 Å for MoS_2 and $PtSe_2$, respectively, with relative differences of 0.3 % and 1.3 % compared to the results listed in Chapter 5. To model the vertically stacked heterobilayer, a matching supercell was searched following the same procedure discussed in Chapter 5. However, the method employed to carry out the TDDFT simulations is restricted to the Γ-point of the FBZ, and because of that, a large unit cell should be employed as way to ensure that a BZ sampling with only Γ-point is adequate. Therefore, the chosen matching supercell corresponds to $(3\sqrt{3} \times 3\sqrt{3})$ MoS_2 and $(\sqrt{19} \times \sqrt{19})$ $PtSe_2$, with ± 0.4 % strain in the monolayers. Since the results of structural relaxation of the supercells discussed in Section 5.2 show that the lattice parameters are only slightly modified, in this case only the atomic positions were allowed to relax by minimization of forces, to obtain the equilibrium interlayer distance.

The electronic band structure of the heterobilayer is shown in Figure 25, which shows the VBM upshift effect discussed in Chapter 5, that is, the heterobilayer VBM is higher in energy than the original VBM of $PtSe_2$ and is delocalized among the two monolayers. This feature does not modify the expected trend of transfer of both electrons and holes from MoS_2 to $PtSe_2$, since in the heterobilayer band structure there are still valence states located in $PtSe_2$ with higher energy than the VBM of MoS_2 and also conduction band states primarily confined to $PtSe_2$ with lower energy than the CBM of

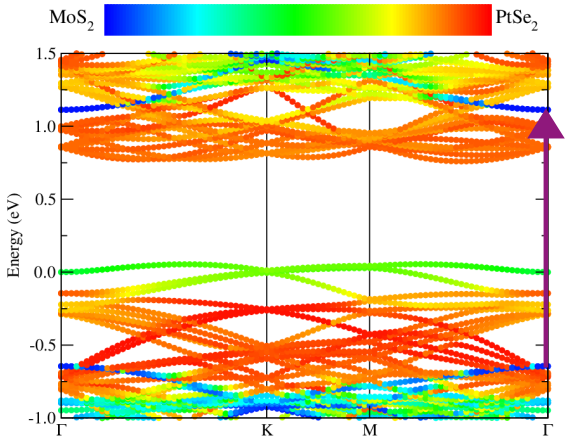

Figure 25 – Electronic band Structure of the 2H-MoS_2/1T-$PtSe_2$ vertical heterobilayer with a $(3\sqrt{3} \times 3\sqrt{3})$ MoS_2 / $(\sqrt{19} \times \sqrt{19})$ $PtSe_2$ matching, obtained with DFT-LDA. Color scale indicates local projection of the electronic states onto each layer. Zero energy is set at the valence band maximum at Γ point. The vertical purple arrow indicates an excitation across the direct band gap of MoS_2

Source: By the author.

MoS_2. Therefore, the photoexcitation across the direct band gap of MoS_2, denoted by the purple arrow in Figure 25, is expected to lead to the transfer of electrons and holes to $PtSe_2$. Due the large size of the employed supercell, there are enough bands sampled in the Γ-point and the bands have low dispersion. Furthermore, although the band edges of the heterobilayers are located out of the Γ-point, energy differences to the respective band edges at the Γ-point are only 0.05 eV and 0.09 eV for the VBM and CBM, respectively.

6.2 Time evolution of charge carriers occupations

To model the initial stages of the dynamics of an excited state of the heterobilayer, a photoexcitation across the direct band gap of MoS_2 was modeled by inverting the occupation of the VBM and CBM states of MoS_2. Although in the simulations the system is not in thermal equilibrium and therefore temperature is undefined, as discussed in Section 2.3, TDDFT formalism depends on the initial state. Thus, to obtain initial configuration for the system, ion positions and velocities were obtained from constant energy MD simulations at ground-state to thermalize the system at target temperatures T_i, which define the initial configurations. Two different T_i were employed to evaluate the role of electron-phonon coupling in the charge transfer, namely $T_i = 77$ K and 300 K. The time-evolved orbitals of the VBM and CBM of MoS_2 correspond to the wave functions of electrons and holes, and have fixed occupation along the simulation. Therefore, the occupations of electrons and holes in $PtSe_2$ were evaluated by population analysis via the projection of the electron and hole orbitals onto the localized basis functions of atoms

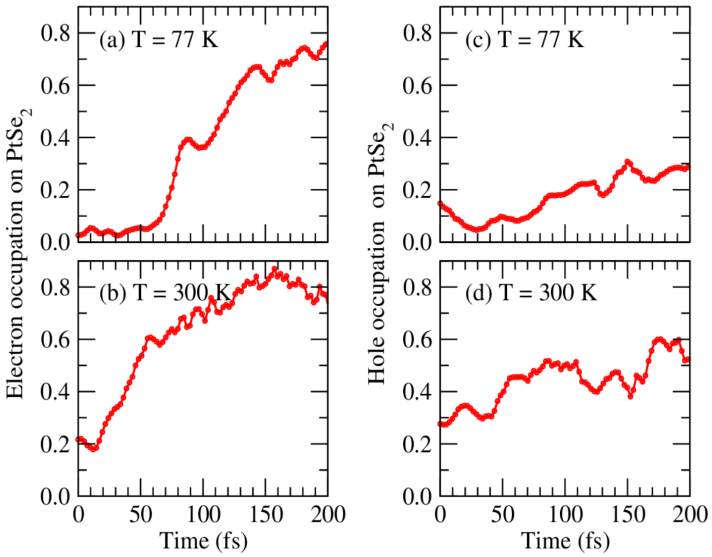

Figure 26 – Occupation of electron (left column) and hole (right column) on the $PtSe_2$ layer for the initial ionic temperatures of 77 K (top row) and 300 K (bottom row).

Source: By the author.

that belong to the $PtSe_2$ monolayer. In this approach, the occupation of the charge carrier with orbital $\phi_i(\mathbf{r};t)$ is given by

$$\rho_i = \sum_{\mu} \left[|c_{i\mu}|^2 + \sum_{\nu \neq \mu} \mathrm{Re}\left(c^*_{n\mu} c_{n\nu} S_{\mu\nu} \right) \right] \ , \tag{6.1}$$

where $c_{i\alpha}$ are the coefficients of the expansion of $\phi_i(\mathbf{r};t)$ onto the atomic orbital basis, μ is restricted to atomic orbitals of the atoms that belong to the $PtSe_2$ monolayer, and ν runs over are all the atomic orbitals.

The time evolution of electron and hole occupations in $PtSe_2$ are shown in Figure 26, for the two T_i. The expected trends of charge carrier transfer are verified, that is, the occupations of both charge carriers in $PtSe_2$ increase, although electron transfer occurs at a greater magnitude than hole transfer. The initial occupations are larger than zero because of the delocalization of the MoS_2 band edge states across the interface, which is increased by the atomic displacements from the equilibrium, as seen by the effect of T_i. The ultrafast transfer of carriers is also observed, especially for electrons, with almost complete transfer within the simulated time scale of 200 fs. These results can be contrasted with the interlayer transfer of holes reported for the MoS_2/WS_2 heterobilayer, within the theoretical framework.[71] By simulating a photoexcitation across the band gap of MoS_2, the hole occupation on WS_2 shows periodic oscillations, which were found to be induced by the dipole coupling of states across the interface and the enhancement caused by interfacial dipole built-up with hole transfer. No analogous of the charge oscillations of hole occupation was observed here, which can be attributed to weaker interlayer dipole

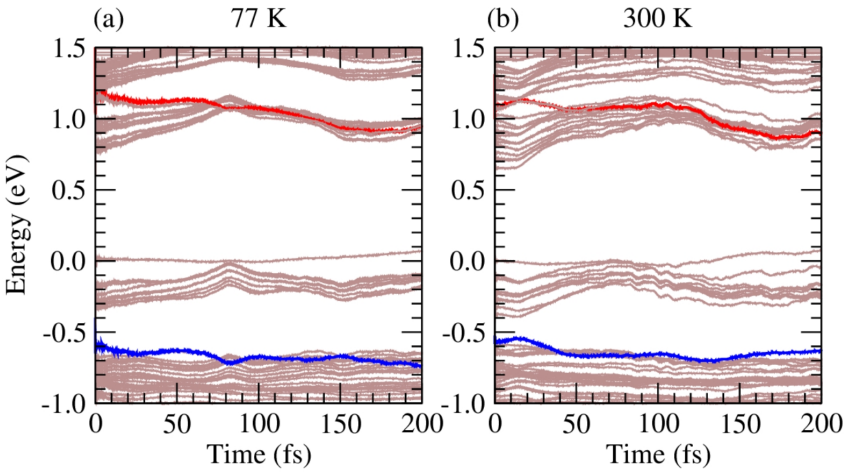

Figure 27 – Time evolution of Γ–point energy states for (a) $T_i = 77\,\mathrm{K}$ and (b) $T_i = 300\,\mathrm{K}$. Zero energy is set to the Γ–point VBM at $t = 0$. The blue and red lines denote the states of hole and electron, respectively, and the remaining (brown) lines are the nearby states.

Source: By the author.

coupling, because of the important role played by the spatial overlap of wave functions, which strongly depends on the stacking configuration.[71] In $MoS_2/PtSe_2$, the monolayers do not share the same structural phase, which limits spatial overlap of wave functions and hinders the strong coupling required for the charge oscillations. Similarly, the difference between monolayers phases has also been proposed as the cause for the slow charge carrier transfer experimentally observed in 2H-MoS_2/1T′-ReS_2.[75]

6.3 Mechanisms of interlayer charge carrier transfer

Further insights into the mechanisms of interlayer transfer of electron and hole, can be obtained by the analysis of the time evolution of the energy states, Figure 27. These plots show the energy of the time-evolved states, which are not the eigenstates of the ionic configurations of each time step. For $T_i = 77\,\mathrm{K}$, the marked change in the rate of increase of electron occupation on $PtSe_2$ at around 60 fs corresponds to the level crossing of the electron orbital with lower energy conduction band states that are predominantly located at the $PtSe_2$ side. Therefore, the fast electron transfer can be attributed to the level crossing with direct intermixing of states,[152] since before the level crossing only a slow increase in the electron population in $PtSe_2$ is observed, which is related to electron transfer to lower energy empty $PtSe_2$ states, likely via slow electron-phonon coupling process. The key role of electron-phonon coupling do initiate the transfer of charge carriers is revealed by the absence of variations in hole and electron occupation for simulations performed with clamped ions ($T_i = 0\,\mathrm{K}$). The level crossing is enabled by the energy decrease of the electron state due to the gain of spectral weight from $PtSe_2$ states with

lower energy. Another source is the build-up of negative charge on the $PtSe_2$ side, which generates an interfacial dipole and promotes relative energy shift of states spatially confined at different sides of the junction. The accumulation of negative charge on $PtSe_2$ arises from the imbalance of electron and hole transfer, since in the initial stages of the simulation the hole occupation in the $PtSe_2$ layer is virtually unchanged before 50 fs.

The transfer of holes is slow because the hole relaxation to states with lower energy (higher electron energy), which are predominantly located at $PtSe_2$, is hindered by the larger energy gap between these bands and the hole state. For instance, in the equilibrium configuration, Figure 25, the energy gap between the MoS_2 CBM and lower conduction band states, that reside in $PtSe_2$, is of 0.11 eV, and the gap between MoS_2 VBM and higher energy valence band states of $PtSe_2$ is of 0.36 eV. Indeed, the time-evolution of the energy of the hole state, Figure 27, shows that the hole transfer to $PtSe_2$ is related to occupation of $PtSe_2$ states below the MoS_2 VBM. This is corroborated by the projection of the hole state onto the eigenstates of the ionic configurations along the simulation, which show that, the contribution of hole occupation from $PtSe_2$ states above the MoS_2 VBM is virtually none. A level crossing is also observed to facilitate hole transfer for $t > 150$ fs, but the energy of valence band states below the hole state are not as sensitive to the electric dipole induced by imbalanced charge transfer as the conduction band states. This indicates a higher interlayer delocalization of states in the valence band, in agreements with the conclusions of Chapter 5, that could to some degree limit the effect of level crossing.

The role of electron-phonon coupling in the charge carrier transfer can be analyzed based on the results for $T_i = 300$ K. In this case, because the ions are more displaced from their equilibrium positions, the broadening of electronic states is more pronounced. In consequence, the initial electron and hole states have a significant degree of mixing with $PtSe_2$ states, as evident by the electron and hole occupations on $PtSe_2$ for $t = 0$, both larger than 20%, as shown Figure 26 b,d. This intermixing might also contribute to the slight increase in the energy of the electron state during a short time in the initial 15 fs, since the electron state also gains spectral weight from neighboring higher energy $PtSe_2$ states. The increased contribution of the transfer process by electron-phonon coupling causes a rapid increase in the electron occupation on $PtSe_2$ since the start of the simulation, in contrast with the results for $T_i = 77$ K. Because of that , no marked change in the rate of interlayer electron transfer is observed at the level crossing of the electron state and lower energy empty states. The more intense contribution of electron-phonon coupling mechanism due to higher T_i is not sufficient to cause hole relaxation to the $PtSe_2$ states above the MoS_2 VBM, and because of that the hole transfer is still small in comparison with electron transfer.

6.4 Summary

The interlayer transfer of charge carriers in the excited state was studied in the 2H-MoS_2/1T-$PtSe_2$ heterobilayer, which was selected because its band alignment allows to investigate the simultaneous interlayer transfer of electrons and holes created by a photoexcitation across the direct gap of MoS_2. Fast electron transfer has been observed, similar to reports for other TMD heterobilayers in the literature, in contrast with the small hole transfer across the interface. This reveals a mechanism of effective charge separation, due to the imbalance of charge carrier transfer, despite a type-I band alignment suggested by the natural band offsets. One leading factor for the imbalance is the weak coupling of the hole state created in MoS_2 with the higher energy valence states of $PtSe_2$ close to the VBM. The mixing of states promoted by the level crossing that is induced by the electric dipole was found to play an important role in the fast charge carrier transfer process, especially for weak electron-phonon coupling at low ionic temperature.

7 CONCLUSION

This thesis presented a contribution to the knowledge of 2D TMDs by studying various types of systems, such as bulk crystals, monolayers, nanoflakes, and vdW heterostructures, and a wide range of physical properties of this materials, as summarized with the main findings of the thesis in Figure 28. This variety of topics was designed to address relevant open problems in the very active research field of 2D TMDs. To perform the investigations, a theoretical approach was adopted, employing calculations based on DFT to obtain structural, energetic, and electronic properties of the systems. The dynamics of excited states in heterobilayers was studied by means of calculations with a combined TDDFT and MD framework.

Starting with a prototypical vdW layered TMD, $MoSe_2$, energetic and structural properties of the bulk crystal were obtained. It was shown that the weak vdW bonding between stacked layers in the three polytypes (2H, 1T, and 1T′) leads to a similarity of bond lengths and coordination environments between bulk and isolated monolayers, and also of the relative stability of phases, that is not affected by layer stacking. The role of the Peierls transition mechanism in the relative stability of 1T′ and 1T phases was demonstrated, and this effect causes nanoflakes of the octahedral phase to naturally adopt the distorted 1T′ configuration upon structural relaxation. It was found that the size of $(MoSe_2)_n$ nanoflakes plays a crucial role in the relative phase stability, and 1T′ is the lowest energy structure for small sized nanoflakes, in contrast with the monolayer limit, with a transition occurring for n close to 150. The difference of edge formation energy between the phases is an important factor for the transition, because the 2H phase has larger edge energy than 1T′. The nanoflake size also influences electronic properties of the systems, and in contrast with the semiconductor 2H monolayer, the nanoflakes of this phase have metallic-like electronic states in the energy range of the monolayer band gap, which are mainly derived from edge atoms.

To extend the exploration of novel 2D materials for TMDs based on Fe-, Co-, Ni-, and Cu-groups, the equilibrium geometries of 11 crystal structures were obtained for the 36 MQ_2 compounds (M = Fe, Co, Ni, Cu, Ru, Rh, Pd, Ag, Os, Ir, Pt, Au; Q = S, Se, Te). The set of crystal structures was defined based on experimental reports for any of the studied compositions and included layered and non-layered structures. The layered crystal structures were shown to be more energetically favored for the Ni-group TMDs. Among the lowest energy layered crystals of each composition, the Fe- and Ni-groups materials have the lowest magnitude of exfoliation energies. In these systems, interlayer binding is dominated by vdW interactions which suggests they can be more easily exfoliated into mono- and few-layer sheets. The large exfoliation energies of the remaining systems,

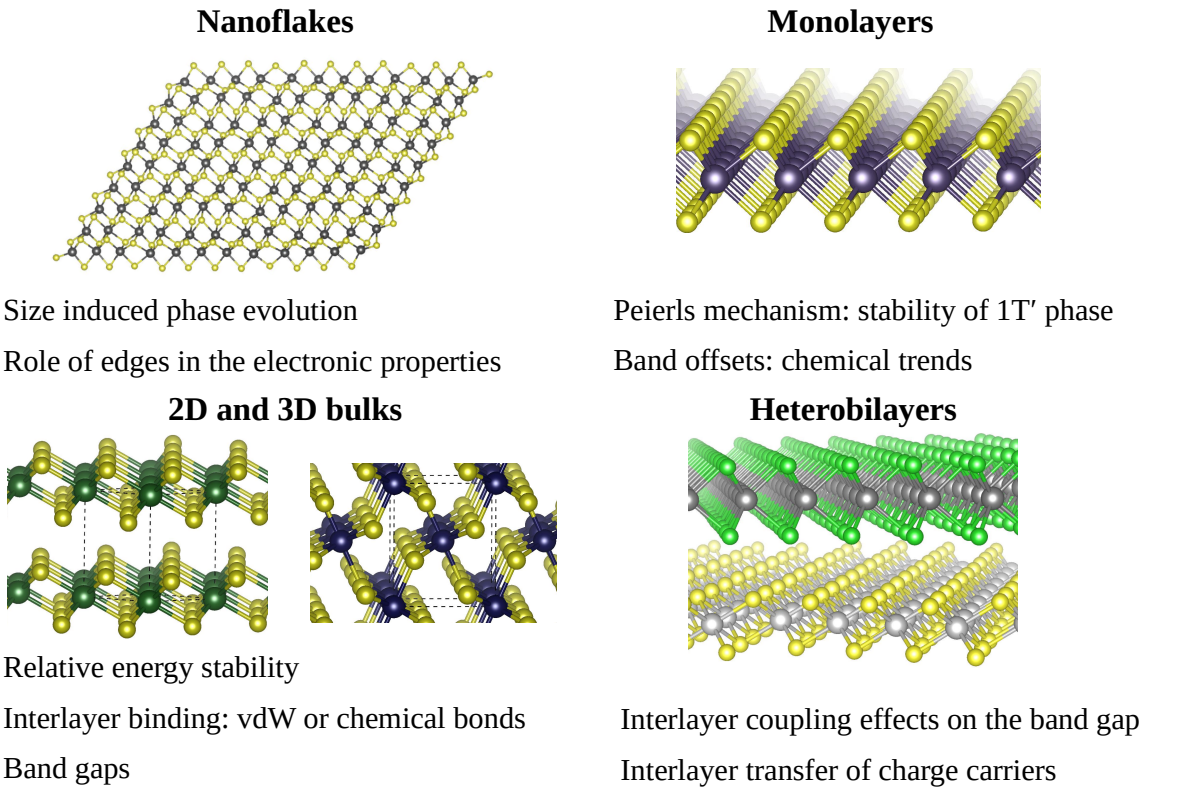

Figure 28 – Graphic summary of the systems studied in the thesis and the main findings.

Source: By the author.

combined with the low contribution of dispersion energy and the features of the ELF, indicates a strong contribution of chemical bonds to the interlayer binding. The lowest energy layered structures of each compound were also selected to screen the electronic properties of monolayers, and a total of 17 semiconductors were found, namely, the Fe-, and Ni-groups materials. The band offsets trends for these monolayers are determined by the orbital composition of band edge states and level repulsion mechanism. These results were employed to predict band alignments within Anderson's rule approximation and to estimate PCE for heterobilayers with type-II junctions, and based solely on this parameter, promising candidates to develop heterojunctions for photovoltaic devices were found.

The role of interlayer coupling effects on the electronic properties of vdW heterostructures and accuracy of Anderson's rule to describe the band gaps were investigated in the 15 heterobilayers of MQ_2 (M = Mo, Ni, Pt; Q = S, Se). The equilibrium geometries and interlayer binding of the systems were obtained, showing the features expected by weak interlayer binding, such as low magnitudes of interlayer charge transfer and interlayer binding energy, and negligible effect of stacking on the intralayer chemical bonds. Despite the weak interlayer binding, non-negligible deviations of band gaps from Anderson's rule were observed, and two sources of the deviations were identified: (1) band gaps

can be decreased due to valence band upshifts that are caused by interlayer hybridization of electron states, specially p_z-states of the Q atoms; (2) in type-II junctions, the formation of interfacial electric dipole contributes to increase the band gap. Because of the weak interlayer binding, the formation of the interfacial dipole can be explained by the change in the decay length of charge density tails outside the monolayers due to the contact. This model describes a correlation between the magnitude of the interfacial dipole and band edge positions of the constituent monolayers, irrespective of junction type.

The dynamics of interlayer charge carrier transfer in van der Waals heterostructures was studied for the case of the 2H-MoS_2/1T-$PtSe_2$ heterobilayer. The band alignment of this system indicates that simultaneous transfer of both electrons and holes to the $PtSe_2$ side should occur following an excitation across the direct band gap of MoS_2, a characteristic of type-I junctions. The fast transfer of electrons was observed, but hole transfer occurs at a slower rate, and the transfer of both charge carriers is enhanced by level crossings promoted by the interfacial electric dipole formed due to the imbalance in charge transfer. A crucial factor for the different rate of charge carriers transfer is the stronger coupling of the MoS_2 CBM with lower energy $PtSe_2$ states in the conduction band, due to the smaller energy difference, when compared to the coupling of MoS_2 VBM and valence band edge states of $PtSe_2$. Interestingly, as a consequence of the imbalance in charge carrier transfer, an effective charge separation was observed, despite the type-I band alignment.

7.1 Papers and manuscripts

The findings discussed in this thesis have been reported in three published papers and one manuscript under preparation. During the period of the PhD studies, the author also collaborated in other seven published papers, and two manuscripts are under preparation. All published papers and manuscripts are listed below.

7.1.1 Published papers

- BESSE, R.; SILVEIRA, J. F. R. V.; JIANG, Z.; WEST, D.; ZHANG, S.; DA SILVA, J. L F. Beyond the Anderson rule: importance of interfacial dipole and hybridization in van der Waals heterostructures. **2D Materials**, v. 8, p. 041002, 2021.

- SILVEIRA, J. F. R. V.; BESSE, R.; DA SILVA, J. L. F. Stacking order effects on the electronic and optical properties of graphene/transition metal dichalcogenide van der Waals heterostructures. **ACS Applied Energy Materials**, v. 3, n. 4, p. 1671-1680, 2021.

- CATURELLO, N. A. M. S.; BESSE, R.; SILVEIRA, J. F .R. V.; LIMA, M. P. DA SILVA, J. L. F. First-principles insights into the role of edges in the binding

mechanisms of Au_4 clusters on $MoSe_2$ nanoflakes. **Physica E**: Low Dimensional Systems and Nanostructures, v. 126, p. 114472, 2021.

- OZÓRIO, M. S.; SRIKANTH, M.; BESSE, R.; DA SILVA, J. L. F. The role of the A-cations in the polymorphic stability and optoelectronic properties of lead-free $ASnI_3$ perovskites. **Physical Chemistry Chemical Physics**, v. 23, n. 3, p. 2286-2297, 2021.

- LIMA, M. P.; BESSE, R.; DA SILVA, J. L. F. Ab initio investigation of topological phase transitions induced by pressure in trilayer van der Waals structures: the example of h-BN/SnTe/h-BN. **Journal of Physics**: Condensed Matter v. 33, n. 2, p. 025003, 2020.

- BESSE, R.; LIMA, M. P.; DA SILVA, J. L. F. First-principles exploration of two-dimensional transition metal dichalcogenides based on Fe-, Co-, Ni-, and Cu-Groups and their van der Waals Heterostructures. **ACS Applied Energy Materials**, v. 2, n. 12, p. 8491-8501, 2019.

- BASTOS, C. M. O.; BESSE, R.; DA SILVA, J. L F.; SIPAHI, G. M. Ab initio investigation of structural stability and exfoliation energies in transition metal dichalcogenides based on Ti-, V-, and Mo-group elements. **Physical Review Materials**, v. 3, n.4, p. 044002, 2019.

- DA SILVA, A. C. H.; CATURELLO, N. A. M. S.; BESSE, R.; LIMA, M. P.; DA SILVA, J. L. F. Edge, size, and shape effects on WS_2, WSe_2, and WTe_2 nanoflake stability: design principles from an ab initio investigation. **Physical Chemistry Chemical Physics**, v. 21, n. 41, p. 23076-23084, 2019.

- CATURELLO, N. A. M. S.; BESSE, R.; DA SILVA, A. C. H.; GUEDES-SOBRINHO, D.; LIMA, M. P.; DA SILVA, J. L. F. Ab initio investigation of atomistic insights into the nanoflake formation of transition-metal dichalcogenides: the examples of MoS_2, $MoSe_2$, and $MoTe_2$. **Journal of Physical Chemistry C**, v. 122, n. 47, p. 27059-27069, 2018.

- BESSE, R.; CATURELLO, N. A. M. S.; BASTOS, C. M. O.; GUEDES-SOBRINHO, D.; LIMA, M. P.; SIPAHI, G. M.; DA SILVA, J. L. F. Size-induced phase evolution of $MoSe_2$ nanoflakes revealed by density functional theory. **Journal of Physical Chemistry C**, v. 122, n. 35, p. 20483-20488, 2018.

7.1.2 Manuscripts under preparation

- BESSE, R.; WANG, H.; WEST, D.; DA SILVA, J. L. F.; ZHANG, S. Charge separation in photoexcited carriers in type-I $MoS_2/PtSe_2$ van der Waals heterobilayer.

- SILVEIRA, J. F. R. V.; BESSE, R.; DIAS, A. C.; CATURELLO, N. A. M. S.; DA SILVA, J. L F. Tailoring properties of MX_2/MX_2, MXY/MX_2, and MXY/MXY bilayers by stacking effects (M = Mo, W; X, Y = S, Se).
- INUI, G. K.; SILVEIRA, J. F. R. V.; DIAS, A. C.; BESSE, R.; DA SILVA. J. L. F. Ab initio screening of stable two-dimensional MQ_x materials (M = Cu, Ag; Q = S, Se, Te; x = 0.5, 1.0, 1.5, 2.0).

REFERENCES

1 NOVOSELOV, K. S. *et al.* Electric field effect in atomically thin carbon films. **Science**, v. 306, n. 5696, p. 666–669, 2004. DOI: 10.1126/science.1102896.

2 NOVOSELOV, K. S. *et al.* Two-dimensional atomic crystals. **Proceedings of the National Academy of Sciences**, v. 102, n. 30, p. 10451–10453, 2005. DOI: 10.1073/pnas.0502848102.

3 GEIM, A. K.; NOVOSELOV, K. S. The rise of graphene. **Nature Materials**, v. 6, n. 3, p. 183–191, 2007. DOI: 10.1038/nmat1849.

4 DEAN, C. R. *et al.* Boron nitride substrates for high-quality graphene electronics. **Nature Nanotechnology**, v. 5, n. 10, p. 722–726, 2010. DOI: 1038/nnano.2010.172.

5 WANG, Q. H. *et al.* Electronics and optoelectronics of two-dimensional transition metal dichalcogenides. **Nature Nanotechnology**, v. 7, n. 11, p. 699–712, 2012. DOI: 10.1038/nnano.2012.193.

6 VOGT, P. *et al.* Silicene: compelling experimental evidence for graphenelike two-dimensional silicon. **Physical Review Letters**, v. 108, n. 15, p. 155501, 2012. DOI: 10.1103/PhysRevLett.108.155501.

7 XIA, F.; WANG, H.; JIA, Y. Rediscovering black phosphorus as an anisotropic layered material for optoelectronics and electronics. **Nature Communications**, v. 5, n. 1, p. 4458, 2014. DOI: 10.1038/ncomms5458.

8 NAGUIB, M. *et al.* Two-dimensional nanocrystals produced by exfoliation of Ti_3AlC_2. **Advanced Materials**, v. 23, n. 37, p. 4248–4253, 2011. DOI: 10.1002/adma.201102306.

9 DU, K.-z. *et al.* Weak van der Waals stacking, wide-range band gap, and Raman study on ultrathin layers of metal phosphorus trichalcogenides. **ACS Nano**, v. 10, n. 2, p. 1738–1743, 2016. DOI: 10.1021/acsnano.5b05927.

10 SHI, E. *et al.* Two-dimensional halide perovskite nanomaterials and heterostructures. **Chemical Society Reviews**, v. 47, n. 16, p. 6046–6072, 2018. DOI: 10.1039/C7CS00886D.

11 LEBÈGUE, S. *et al.* Two-dimensional materials from data filtering and ab initio calculations. **Physical Review X**, v. 3, n. 3, p. 031002, 2013. DOI: 10.1103/PhysRevX.3.031002.

12 CHOUDHARY, K. *et al.* High-throughput identification and characterization of two-dimensional materials using density functional theory. **Scientific Reports**, v. 7, n. 1, p. 5179, 2017. DOI: 10.1038/s41598-017-05402-0.

13 ASHTON, M. *et al.* Topology-scaling identification of layered solids and stable exfoliated 2D materials. **Physical Review Letters**, v. 118, n. 10, p. 106101, 2017. DOI: 10.1103/PhysRevLett.118.106101.

14 MOUNET, N. *et al.* Two-dimensional materials from high-throughput computational exfoliation of experimentally known compounds. **Nature Nanotechnology**, v. 13, n. 3, p. 246–252, 2018. DOI: 10.1038/s41565-017-0035-5.

15 BJÖRKMAN, T. *et al.* van der Waals bonding in layered compounds from advanced density-functional first-principles calculations. **Physical Review Letters**, v. 108, n. 23, p. 235502, 2012. DOI: 10.1103/PhysRevLett.108.235502.

16 DESAI, S. B. *et al.* MoS_2 transistors with 1-nanometer gate lengths. **Science**, v. 354, n. 6308, p. 99–102, 2016. DOI: 10.1126/science.aah4698.

17 TAO, H. *et al.* Two-dimensional nanosheets for electrocatalysis in energy generation and conversion. **Journal of Materials Chemistry A**, v. 5, n. 16, p. 7257–7284, 2017. DOI: 10.1039/C7TA00075H.

18 ZHANG, G.; ZHANG, Y.-W. Thermoelectric properties of two-dimensional transition metal dichalcogenides. **Journal of Materials Chemistry C**, v. 5, n. 31, p. 7684–7698, 2017. DOI: 10.1039/C7TC01088E.

19 COLEMAN, J. N. *et al.* Two-dimensional nanosheets produced by liquid exfoliation of layered materials. **Science**, v. 331, n. 6017, p. 568–571, 2011. DOI: 10.1126/science.1194975.

20 BHIMANAPATI, G. R. *et al.* Recent advances in two-dimensional materials beyond graphene. **ACS Nano**, v. 9, n. 12, p. 11509–11539, 2015. DOI: 10.1021/acsnano.5b05556.

21 ZHOU, J. *et al.* A library of atomically thin metal chalcogenides. **Nature**, v. 556, n. 7701, p. 355–359, 2018. DOI: 10.1038/s41586-018-0008-3.

22 GEIM, A. K.; GRIGORIEVA, I. V. Van der Waals heterostructures. **Nature**, v. 499, n. 7459, p. 419–425, 2013. DOI: 10.1038/nature12385.

23 NOVOSELOV, K. S. *et al.* 2D materials and van der Waals heterostructures. **Science**, v. 353, n. 6298, p. aac9439, 2016. DOI: 10.1126/science.aac9439.

24 VU, Q. A. *et al.* Tuning carrier tunneling in van der Waals heterostructures for ultrahigh detectivity. **Nano Letters**, v. 17, n. 1, p. 453–459, 2017. DOI: 10.1021/acs.nanolett.6b04449.

25 LIU, C.-H. *et al.* Nanocavity integrated van der Waals heterostructure light-emitting tunneling diode. **Nano Letters**, v. 17, n. 1, p. 200–205, 2017. DOI: 10.1021/acs.nanolett.6b03801.

26 CUI, W. *et al.* Triphasic 2D materials by vertically stacking laterally heterostructured 2H-/1T′-MoS_2 on graphene for enhanced photoresponse. **Advanced Electronic Materials**, v. 3, n. 7, p. 1700024, 2017. DOI: 10.1002/aelm.201700024.

27 LEE, G. *et al.* Two-dimensionally layered p-black phosphorus/n-MoS_2/p-black phosphorus heterojunctions. **ACS Applied Materials & Interfaces**, v. 10, n. 12, p. 10347–10352, 2018. DOI: 10.1021/acsami.7b19334.

28 SCHAIBLEY, J. R. *et al.* Directional interlayer spin-valley transfer in two-dimensional heterostructures. **Nature Communications**, v. 7, n. 1, p. 13747, 2016. DOI: 10.1038/ncomms13747.

29 LINGHU, J. *et al.* High-throughput computational screening of vertical 2D van der Waals heterostructures for high-efficiency excitonic solar cells. **ACS Applied Materials & Interfaces**, v. 10, n. 38, p. 32142–32150, 2018. DOI: 10.1021/acsami.8b09454.

30 MAK, K. F. *et al.* Atomically thin MoS_2: a new direct-gap semiconductor. **Physical Review Letters**, v. 105, n. 13, p. 136805, 2010. DOI: 10.1103/PhysRevLett.105.136805.

31 CHHOWALLA, M. *et al.* The chemistry of two-dimensional layered transition metal dichalcogenide nanosheets. **Nature Chemistry**, v. 5, n. 4, p. 263–275, 2013. DOI: 10.1038/nchem.1589.

32 SUSARLA, S. *et al.* Quaternary 2D transition metal dichalcogenides (TMDs) with tunable bandgap. **Advanced Materials**, v. 29, n. 35, p. 1702457, 2017. DOI: 10.1002/adma.201702457.

33 YANG, H. *et al.* Structural and quantum-state phase transition in van der Waals layered materials. **Nature Physics**, v. 13, p. 931–937, 2017. DOI: 10.1038/nphys4188.

34 MANZELI, S. *et al.* 2D transition metal dichalcogenides. **Nature Reviews Materials**, v. 2, n. 8, p. 17033, 2017. DOI: 10.1038/natrevmats.2017.33.

35 FRIEDMAN, A. L. *et al.* Evidence for chemical vapor induced 2H to 1T′ phase transition in MoX_2 (X = Se, S) transition metal dichalcogenide films. **Scientific Reports**, v. 7, n. 1, p. 3836, 2017. DOI: 10.1038/s41598-017-04224-4.

36 QIAN, X. *et al.* Quantum spin Hall effect in two-dimensional transition metal dichalcogenides. **Science**, v. 346, n. 6215, p. 1344–1347, 2014. DOI: 10.1126/science.1256815.

37 LI, B. L. *et al.* Emerging 0D transition-metal dichalcogenides for sensors, biomedicine, and clean energy. **Small**, v. 13, n. 31, p. 1700527, 2017. DOI: 10.1002/smll.201700527.

38 ZHAO, X. *et al.* Enhanced catalytic activities of surfactant-assisted exfoliated WS_2 nanodots for hydrogen evolution. **ACS Nano**, v. 10, n. 2, p. 2159–2166, 2016. DOI: 10.1021/acsnano.5b06653.

39 ZHANG, S.; JIA, X.; WANG, E. Facile synthesis of optical pH-sensitive molybdenum disulfide quantum dots. **Nanoscale**, v. 8, n. 33, p. 15152–15157, 2016. DOI: 10.1039/C6NR04726B.

40 XU, S.; LI, D.; WU, P. One-pot, facile, and versatile synthesis of monolayer MoS_2/WS_2 quantum dots as bioimaging probes and efficient electrocatalysts for hydrogen evolution reaction. **Advanced Functional Materials**, v. 25, n. 7, p. 1127–1136, 2015. DOI: 10.1002/adfm.201403863.

41 WANG, L. *et al.* Atomic mechanism of dynamic electrochemical lithiation processes of MoS_2 nanosheets. **Journal of American Chemical Socoety**, v. 136, n. 18, p. 6693–6697, 2014. DOI: 10.1021/ja501686w.

42 LIN, Y.-C. *et al.* Atomic mechanism of the semiconducting-to-metallic phase transition in single-layered MoS_2. **Nature Nanotechnology**, v. 9, n. 5, p. 391–396, 2014. DOI: 10.1038/nnano.2014.64.

43 DUERLOO, K.-A. N.; LI, Y.; REED, E. J. Structural phase transitions in two-dimensional Mo- and W- dichalcogenide monolayers. **Nature Communications**, v. 5, n. 1, p. 4214, 2014. DOI: 10.1038/ncomms5214.

44 ZHOU, S. *et al.* MoS_2 edges and heterophase interfaces: energy, structure and phase engineering. **2D Materials**, v. 4, n. 2, p. 025080, 2017. DOI: 2053-1583/aa6d22.

45 HWANG, W. S. *et al.* High-voltage field effect transistors with wide-bandgap β-Ga_2O_3 nanomembranes. **Applied Physics Letters**, v. 104, n. 20, p. 203111, 2014. DOI: 10.1063/1.4879800.

46 BALAN, A. P. *et al.* Exfoliation of a non-van der Waals material from iron ore hematite. **Nature Nanotechnology**, v. 13, n. 7, p. 602–609, 2018. DOI: 10.1038/s41565-018-0134-y.

47 HAASTRUP, S. *et al.* The Computational 2D Materials Database: high-throughput modeling and discovery of atomically thin crystals. **2D Materials**, v. 5, n. 4, p. 042002, 2018. DOI: 10.1088/2053-1583/aacfc1.

48 LUCKING, M. C. *et al.* Traditional semiconductors in the two-dimensional limit. **Physical Review Letters**, v. 120, n. 8, p. 086101, 2018. DOI: 10.1103/PhysRevLett.120.086101.

49 HOCKINGS, E.; WHITE, J. The system iridium—tellurium. **Journal of Physical Chemistry**, v. 64, n. 8, p. 1042–1045, 1960. DOI: 10.1021/j100837a019.

50 WILSON, J.; YOFFE, A. The transition metal dichalcogenides discussion and interpretation of the observed optical, electrical and structural properties. **Advances in Physics**, v. 18, n. 73, p. 193–335, 1969. DOI: 10.1080/00018736900101307.

51 BITHER, T. A. *et al.* Transition metal pyrite dichalcogenides. high-pressure synthesis and correlation of properties. **Inorganic Chemistry**, v. 7, n. 11, p. 2208–2220, 1968. DOI: 10.1021/ic50069a008.

52 BROSTIGEN, G. *et al.* Compounds with the marcasite type crystal structure. VIII. redetermination of the prototype. **Acta Chemica Scandinavica**, v. 27, n. 6, p. 2791–2796, 1973.

53 RASMUSSEN, F. A.; THYGESEN, K. S. Computational 2D materials database: electronic structure of transition-metal dichalcogenides and oxides. **Journal of Physical Chemistry C**, v. 119, n. 23, p. 13169–13183, 2015. DOI: 10.1021/acs.jpcc.5b02950.

54 ROY, T. *et al.* Dual-gated MoS_2/WSe_2 van der Waals tunnel diodes and transistors. **ACS Nano**, v. 9, n. 2, p. 2071–2079, 2015. DOI: 10.1021/nn507278b.

55 LI, C. *et al.* Engineering graphene and TMDs based van der Waals heterostructures for photovoltaic and photoelectrochemical solar energy conversion. **Chemical Society Reviews**, v. 47, n. 13, p. 4981–5037, 2018. DOI: 10.1039/C8CS00067K.

56 FURCHI, M. M. *et al.* Device physics of van der Waals heterojunction solar cells. **npj 2D Materials and Applications**, v. 2, n. 1, p. 1–7, 2018. DOI: 10.1038/s41699-018-0049-3.

57 ÖZCELIK, V. O. *et al.* Band alignment of two-dimensional semiconductors for designing heterostructures with momentum space matching. **Physical Review B**, v. 94, n. 3, p. 035125, 2016. DOI: 10.1103/PhysRevB.94.035125.

58 ZHENG, W. *et al.* Direct vapor growth of 2D vertical heterostructures with tunable band alignments and interfacial charge transfer behaviors. **Advanced Science**, v. 6, n. 7, p. 1802204, 2019. DOI: 10.1002/advs.201802204.

59 YAN, R. *et al.* Esaki diodes in van der Waals heterojunctions with broken-gap energy band alignment. **Nano Letters**, v. 15, n. 9, p. 5791–5798, 2015. DOI: 10.1021/acs.nanolett.5b01792.

60 ANDERSON, R. Germanium-gallium arsenide heterojunctions. **IBM Journal of Research and Development**, v. 4, n. 3, p. 283–287, 1960. DOI: 10.1147/rd.43.0283.

61 CHIU, M.-H. *et al.* Band alignment of 2D transition metal dichalcogenide heterojunctions. **Advanced Functional Materials**, v. 27, n. 19, p. 1603756, 2016. DOI: 10.1002/adfm.201603756.

62 ZHAO, Q. *et al.* Band alignments and heterostructures of monolayer transition metal trichalcogenides MX_3 (M = Zr, Hf; X = S, Se) and dichalcogenides MX_2 (M = Tc, Re; X = S, Se) for solar applications. **Nanoscale**, v. 10, n. 7, p. 3547–3555, 2018. DOI: 10.1039/C7NR08413G.

63 DONG, R. *et al.* High-throughput bandstructure simulations of van der Waals hetero-bilayers formed by 1T and 2H monolayers. **npj 2D Materials and Applications**, v. 5, n. 1, p. 26, 2021. DOI: 10.1038/s41699-021-00200-9.

64 ZHANG, L.; ZUNGER, A. Evolution of electronic structure as a function of layer thickness in group-VIB transition metal dichalcogenides: emergence of localization prototypes. **Nano Letters**, v. 15, n. 2, p. 949–957, 2015. DOI: 10.1021/nl503717p.

65 ZHAO, Y. *et al.* Extraordinarily strong interlayer interaction in 2D layered PtS_2. **Advanced Materials**, v. 28, n. 12, p. 2399–2407, 2016. DOI: 10.1002/adma.201504572.

66 KODA, D. S. *et al.* Trends on band alignments: validity of anderson's rule in SnS_2- and $SnSe_2$- based van der Waals heterostructures. **Physical Review B**, v. 97, n. 16, p. 165402, 2018. DOI: 10.1103/PhysRevB.97.165402.

67 SI, Y. *et al.* A design rule for two-dimensional van der Waals heterostructures with unconventional band alignments. **Physical Chemistry Chemical Physics**, v. 22, n. 5, p. 3037–3047, 2020. DOI: 10.1039/C9CP06465F.

68 CEBALLOS, F. *et al.* Ultrafast charge separation and indirect exciton formation in a MoS_2–$MoSe_2$ van der Waals heterostructure. **ACS Nano**, v. 8, n. 12, p. 12717–12724, 2014. DOI: 10.1021/nn505736z.

69 HONG, X. *et al.* Ultrafast charge transfer in atomically thin MoS_2/WS_2 heterostructures. **Nature Nanotechnology**, v. 9, n. 9, p. 682, 2014. DOI: 10.1038/nnano.2014.167.

70 JIN, C. *et al.* Ultrafast dynamics in van der Waals heterostructures. **Nature Nanotechnology**, v. 13, n. 11, p. 994–1003, 2018. DOI: 10.1038/s41565-018-0298-5.

71 WANG, H. *et al.* The role of collective motion in the ultrafast charge transfer in van der Waals heterostructures. **Nature Communications**, v. 7, n. 1, p. 11504, 2016. DOI: 10.1038/ncomms11504.

72 LONG, R.; PREZHDO, O. V. Quantum coherence facilitates efficient charge separation at a MoS_2/$MoSe_2$ van der Waals junction. **Nano Letters**, v. 16, n. 3, p. 1996–2003, 2016. DOI: 10.1021/acs.nanolett.5b05264.

73 LI, L.; LONG, R.; PREZHDO, O. V. Charge separation and recombination in two-dimensional MoS_2/WS_2: time-domain ab initio modeling. **Chemistry of Materials**, v. 29, n. 6, p. 2466–2473, 2017. DOI: 10.1021/acs.chemmater.6b03727.

74 KANG, J. *et al.* Band offsets and heterostructures of two-dimensional semiconductors. **Applied Physics Letters**, v. 102, n. 1, p. 012111, 2013. DOI: 10.1063/1.4774090.

75 BELLUS, M. Z. *et al.* Type-I van der Waals heterostructure formed by MoS_2 and ReS_2 monolayers. **Nanoscale Horizons**, v. 2, n. 1, p. 31–36, 2017. DOI: 10.1039/C6NH00144K.

76 YING, H. *et al.* Band structure engineering in MoS_2 based heterostructures toward high-performance phototransistors. **Advanced Optical Materials**, v. 8, n. 13, p. 2000430, 2020. DOI: 10.1002/adom.202000430.

77 LEVINE, I. N. **Quantum chemistry**. 6th ed. New Jersey: Prentice Hall, 2009.

78 BORN, R. O. M. Zur Quantentheorie der Molekeln. **Annalen der Physik**, v. 389, n. 20, p. 457–484, 1927. DOI: 10.1002/andp.19273892002.

79 BORN, K. H. M. **Dynamical theory of crystal lattices**. Oxford: Clarendon Press, 1954.

80 MARTIN, R. M. **Electronic structure:** basic theory and practical methods. Cambridge: Cambridge University Press, 2004.

81 HOHENBERG, P.; KOHN, W. Inhomogeneous electron gas. **Physical Review**, v. 136, n. 3B, p. B864–B871, 1964. DOI: 10.1103/PhysRev.136.B864.

82 KOHN, W.; SHAM, L. J. Self-consistent equations including exchange and correlation effects. **Physical Review**, v. 140, n. 4A, p. A1133–A1138, 1965. DOI: 10.1103/PhysRev.140.A1133.

83 PARR, R. G.; YANG, W. **Density functional theory of atoms and molecules**. Oxford: Oxford University Press, 1989.

84 CARR JR, W. J. Energy, specific heat, and magnetic properties of the low-density electron gas. **Physical Review**, v. 122, n. 5, p. 1437–1446, 1961. DOI: 10.1103/PhysRev.122.1437.

85 CARR JR, W. J.; MARADUDIN, A. A. Ground-state energy of a high-density electron gas. **Physical Review**, v. 133, n. 2A, p. A371, 1964. DOI: 10.1103/PhysRev.133.A371.

86 CEPERLEY, D. M.; ALDER, B. J. Ground state of the electron gas by a stochastic method. **Physical Review Letters**, v. 45, n. 7, p. 566–569, 1980. DOI: 10.1103/PhysRevLett.45.566.

87 PERDEW, J. P.; ZUNGER, A. Self-interaction correction to density-functional approximations for many-electron systems. **Physical Review B**, v. 23, n. 10, p. 5048–5079, 1981. DOI: 10.1103/PhysRevB.23.5048.

88 PERDEW, J. P.; WANG, Y. Accurate and simple analytic representation of the electron-gas correlation energy. **Physical Review B**, v. 45, n. 23, p. 13244–13249, 1992. DOI: 10.1103/PhysRevB.45.13244.

89 PERDEW, J. P. *et al.* Atoms, molecules, solids, and surfaces: applications of the generalized gradient approximation for exchange and correlation. **Physical Review B**, v. 46, n. 11, p. 6671–6687, 1992. DOI: 10.1103/PhysRevB.46.6671.

90 BURKE, K.; PERDEW, J. P.; WANG, Y. Derivation of a generalized gradient approximation: the PW91 density functional. *In*: DOBSON, J. F.; VIGNALE, G.; DAS, M. P. (ed.). **Electronic density functional theory:** recent progress and new directions. New York: Springer, 1998. p. 81–111.

91 PERDEW, J. P.; BURKE, K.; ERNZERHOF, M. Generalized gradient approximation made simple. **Physical Review Letters**, v. 77, n. 18, p. 3865–3868, 1996. DOI: 10.1103/PhysRevLett.77.3865.

92 PERDEW, J. P. *et al.* Understanding band gaps of solids in generalized Kohn–Sham theory. **Proceedings of the National Academy of Sciences**, v. 114, n. 11, p. 2801–2806, 2017. DOI: 10.1073/pnas.1621352114.

93 PERDEW, J. P.; ERNZERHOF, M.; BURKE, K. Rationale for mixing exact exchange with density functional approximations. **Journal of Chemical Physics**, v. 105, n. 22, p. 9982–9985, 1996. DOI: 10.1063/1.472933.

94 HEYD, J.; SCUSERIA, G. E.; ERNZERHOF, M. Hybrid functionals based on a screened Coulomb potential. **Journal of Chemical Physics**, v. 118, n. 18, p. 8207–8215, 2003. DOI: 10.1063/1.1564060.

95 KRUKAU, A. V. *et al.* Influence of the exchange screening parameter on the performance of screened hybrid functionals. **Journal of Chemical Physics**, v. 125, n. 22, p. 224106, 2006. DOI: 10.1063/1.2404663.

96 PEELAERS, H.; WALLE, C. G. Van de. First-principles study of van der Waals interactions in MoS_2 and MoO_3. **Journal of Physics:** condensed matter, v. 26, n. 30, p. 305502, Jul 2014. DOI: 10.1088/0953-8984/26/30/305502.

97 RÊGO, C. R. C. *et al.* Comparative study of van der Waals corrections to the bulk properties of graphite. **Journal of Physics:** condensed matter, v. 27, n. 41, p. 415502, Sep 2015. DOI: 10.1088/0953-8984/27/41/415502.

98 GRIMME, S. *et al.* A consistent and accurate ab initio parametrization of density functional dispersion correction (DFT-D) for the 94 elements H-Pu. **Journal of Chemical Physics**, v. 132, n. 15, p. 154104, 2010. DOI: 10.1063/1.3382344.

99 RECKIEN, W. *et al.* Implementation of empirical dispersion corrections to density functional theory for periodic systems. **Journal of Computational Chemistry**, v. 33, n. 25, p. 2023–2031, 2012. DOI: 10.1002/jcc.23037.

100 RUNGE, E.; GROSS, E. K. Density-functional theory for time-dependent systems. **Physical Review Letters**, v. 52, n. 12, p. 997–1000, 1984. DOI: 10.1103/PhysRevLett.52.997.

101 GROSS, E. K. U.; DOBSON, J. F.; PETERSILKA, M. Density functional theory of time-dependent phenomena. *In*: NALEWAJSKI, R. F. (ed.). **Density functional theory II:** relativistic and time dependent extensions. Berlin: Spinger-Verlag, 1996. p. 81–172.

102 LI, T.-C.; TONG, P.-q. Time-dependent density-functional theory for multicomponent systems. **Physical Review A**, v. 34, n. 1, p. 529–532, 1986. DOI: 10.1103/PhysRevA.34.529.

103 MENG, S.; KAXIRAS, E. Real-time, local basis-set implementation of time-dependent density functional theory for excited state dynamics simulations. **Journal of Chemical Physics**, v. 129, n. 5, p. 054110, 2008. DOI: 10.1063/1.2960628.

104 ASHCROFT, N. W.; MERMIN, N. M. **Solid state physics**. Philadelphia: Saunders College Publishing, 1976.

105 KITTEL, C. **Introduction to solid state physics**. 8th ed. New York: John Wiley & Sons, 1996.

106 SOLER, J. M. *et al.* The SIESTA method for ab initio order-N materials simulation. **Journal of Physics:** condensed matter, v. 14, n. 11, p. 2745–2779, 2002. DOI: 10.1088/0953-8984/14/11/302.

107 BLÖCHL, P. E. Projector augmented-wave method. **Physical Review B**, v. 50, n. 24, p. 17953–17979, 1994. DOI: 10.1103/PhysRevB.50.17953.

108 KRESSE, G.; FURTHMÜLLER, J. Efficiency of ab-initio total energy calculations for metals and semiconductors using a plane-wave basis set. **Computational Materials Science**, v. 6, n. 1, p. 15–50, 1996. DOI: 10.1016/0927-0256(96)00008-0.

109 KRESSE, G.; FURTHMÜLLER, J. Efficient iterative schemes for ab initio total-energy calculations using a plane-wave basis set. **Physical Review B**, v. 54, n. 16, p. 11169–11186, 1996. DOI: 10.1103/PhysRevB.54.11169.

110 KRESSE, G.; JOUBERT, D. From ultrasoft pseudopotentials to the projector augmented-wave method. **Physical Review B**, v. 59, n. 3, p. 1758–1775, 1999. DOI: 10.1103/PhysRevB.59.1758.

111 BESSE, R. *et al.* Size-induced phase evolution of $MoSe_2$ nanoflakes revealed by density functional theory. **Journal of Physical Chemistry C**, v. 122, n. 35, p. 20483–20488, 2018. DOI: 10.1021/acs.jpcc.8b03254.

112 KATZKE, H.; TOLÉDANO, P.; DEPMEIER, W. Phase transitions between polytypes and intralayer superstructures in transition metal dichalcogenides. **Physical Review B**, v. 69, n. 13, p. 134111, 2004. DOI: 10.1103/PhysRevB.69.134111.

113 BROWN, B. E. The crystal structures of WTe_2 and high-temperature $MoTe_2$. **Acta Crystallographica**, v. 20, n. 2, p. 268–274, 1966. DOI: 10.1107/S0365110X66000513.

114 BRONSEMA, K. D.; BOER, J. D.; JELLINEK, F. On the structure of molybdenum diselenide and disulfide. **Zeitschrift für Anorganische und Allgemeine Chemie**, v. 540, n. 9-10, p. 15–17, 1986. DOI: 10.1002/zaac.19865400904.

115 PEIERLS, R. E. **Quantum theory of solids**. Oxford: Clarendon Press, 1955.

116 KAN, M. *et al.* Structures and phase transition of a MoS_2 monolayer. **Journal of Physical Chemistry C**, v. 118, n. 3, p. 1515–1522, 2014. DOI: 10.1021/jp4076355.

117 CUI, P. *et al.* Contrasting structural reconstructions, electronic properties, and magnetic orderings along different edges of zigzag transition metal dichalcogenide nanoribbons. **Nano Letters**, v. 17, n. 2, p. 1097–1101, 2017. DOI: 10.1021/acs.nanolett.6b04638.

118 BESSE, R.; LIMA, M. P.; DA SILVA, J. L. F. First-principles exploration of two-dimensional transition metal dichalcogenides based on Fe, Co, Ni, and Cu groups and their van der Waals heterostructures. **ACS Applied Energy Materials**, v. 2, n. 12, p. 8491–8501, 2019. DOI: 10.1021/acsaem.9b01433.

119 BERGERHOFF, G.; BROWN, I. Inorganic crystal structure database. *In*: ALLEN, F. H.; BERGERHOFF, G.; SIEVERS, R. (ed.). **Crystallogaphic databases**. Chester: International Union of Crystallography, 1987.

120 GRAŽULIS, S. *et al.* Crystallography open database – an open-access collection of crystal structures. **Journal of Applied Crystallography**, v. 42, n. 4, p. 726–729, 2009. DOI: 10.1107/S0021889809016690.

121 REITHMAYER, K. *et al.* High-pressure single-crystal structure study on calaverite, $AuTe_2$. **Acta Crystallographica Section B**, v. 49, n. 1, p. 6–11, 1993. DOI: 10.1107/S0108768192007286.

122 GRØNVOLD, F.; RØST, E. The crystal structure of $PdSe_2$ and PdS_2. **Acta Crystallographica**, v. 10, n. 4, p. 329–331, 1957. DOI: 10.1107/S0365110X57000948.

123 SOULARD, C. *et al.* Experimental and theoretical investigation on the relative stability of the PdS_2- and pyrite-type structures of $PdSe_2$. **Inorganic Chemistry**, v. 43, n. 6, p. 1943–1949, 2004. DOI: 10.1021/ic0352396.

124 BAYLISS, P. Crystal chemistry and crystallography of some minerals within the pyrite group. **American Mineralogist**, v. 74, n. 9-10, p. 1168–1176, 1989.

125 KJEKSHUS, A. *et al.* Compounds with the marcasite type crystal structure. IX. structural data for $FeAs_2$, $FeSe_2$, $NiAs_2$, $NiSb_2$, and $CuSe_2$. **Acta Chemica Scandinavica**, v. 28a, n. 9, p. 996–1000, 1974. DOI: 10.1016/0022-5088(68)90148-3.

126 JOBIC, S. *et al.* Properties of the transition metal dichalcogenides: the case of IrS_2 and $IrSe_2$. **Journal of Solid State Chemistry**, v. 89, n. 2, p. 315–327, 1990.

127 JOBIC, S. *et al.* Synthesis and crystal structure determination of a new pressure-induced iridium ditelluride phase, m-$IrTe_2$, and comparison of the crystal structures and relative stabilities of various $IrTe_2$ polymorphs. **Inorganic Chemistry**, v. 39, n. 19, p. 4370–4373, 2000. DOI: 10.1021/ic000351e.

128 TUNELL, G.; KSANDA, C. J. The crystal structure of krennerite. **Journal of the Washington Academy of Sciences**, v. 26, n. 12, p. 507–509, 1936.

129 DA SILVA, J. L. F. Effective coordination concept applied for phase change $(GeTe)_m(Sb_2Te_3)_n$ compounds. **Journal of Applied Physics**, v. 109, n. 2, p. 023502, Jan 2011. DOI: 10.1063/1.3533422.

130 SLATER, J. C. Atomic radii in crystals. **Journal of Chemical Physics**, v. 41, n. 10, p. 3199–3204, 1964. DOI: 10.1063/1.1725697.

131 GOULD, T.; BUČKO, T. C_6 coefficients and dipole polarizabilities for all atoms and many ions in rows 1–6 of the periodic table. **Journal of Chemical Theory and Computation**, v. 12, n. 8, p. 3603–3613, 2016. DOI: 10.1021/acs.jctc.6b00361.

132 BASTOS, C. M. O. *et al. Ab initio* investigation of structural stability and exfoliation energies in transition metal dichalcogenides based on Ti-, V-, and Mo-group elements. **Physical Review Materials**, v. 3, n. 4, p. 044002, 2019. DOI: 10.1103/PhysRevMaterials.3.044002.

133 BADER, R. F. W. **Atoms in molecules:** a quantum theory. Oxford: Clarendon Press, 1994.

134 HENKELMAN, G.; ARNALDSSON, A.; JÓNSSON, H. A fast and robust algorithm for Bader decomposition of charge density. **Computational Materials Science**, v. 36, n. 3, p. 354–360, 2006. DOI: 10.1016/j.commatsci.2005.04.010.

135 BECKE, A. D.; EDGECOMBE, K. E. A simple measure of electron localization in atomic and molecular systems. **Journal of Chemical Physics**, v. 92, n. 9, p. 5397–5403, 1990. DOI: 10.1063/1.458517.

136 SAVIN, A. *et al.* Electron localization in solid-state structures of the elements: the diamond structure. **Angewandte Chemie International Edition in English**, v. 31, n. 2, p. 187–188, 1992. DOI: 10.1002/anie.199201871.

137 SETYAWAN, W.; CURTAROLO, S. High-throughput electronic band structure calculations: challenges and tools. **Computational Materials Science**, v. 49, n. 2, p. 299–312, 2010. DOI: 10.1016/j.commatsci.2010.05.010.

138 WANG, Y. *et al.* Monolayer $PtSe_2$, a new semiconducting transition-metal-dichalcogenide, epitaxially grown by direct selenization of Pt. **Nano Letters**, v. 15, n. 6, p. 4013–4018, 2015. DOI: 10.1021/acs.nanolett.5b00964.

139 ZHANG, W. *et al.* The mechanism of layer number and strain dependent bandgap of 2D crystal $PtSe_2$. **Journal of Applied Physics**, v. 122, n. 20, p. 205701, 2017. DOI: 10.1063/1.5000419.

140 JARIWALA, D. *et al.* Van der Waals materials for atomically-thin photovoltaics: promise and outlook. **ACS Photonics**, v. 4, n. 12, p. 2962–2970, 2017. DOI: 10.1021/acsphotonics.7b01103.

141 DAS, S. *et al.* The role of graphene and other 2D materials in solar photovoltaics. **Advanced Materials**, v. 31, n. 1, p. 1802722, 2019. DOI: 10.1002/adma.201802722.

142 SCHARBER, M. C. *et al.* Design rules for donors in bulk-heterojunction solar cells—towards 10% energy-conversion efficiency. **Advanced Materials**, v. 18, n. 6, p. 789–794, 2006. DOI: 10.1002/adma.200501717.

143 BERNARDI, M.; PALUMMO, M.; GROSSMAN, J. C. Semiconducting monolayer materials as a tunable platform for excitonic solar cells. **ACS Nano**, v. 6, n. 11, p. 10082–10089, 2012. DOI: 10.1021/nn303815z.

144 BESSE, R. *et al.* Beyond the Anderson rule: importance of interfacial dipole and hybridization in van der Waals heterostructures. **2D Materials**, v. 8, n. 4, p. 041002, 2021. DOI: 10.1088/2053-1583/ac1902.

145 LAZIĆ, P. Cellmatch: combining two unit cells into a common supercell with minimal strain. **Computer Physics Communications**, v. 197, p. 324–334, 2015. DOI: 10.1016/j.cpc.2015.08.038.

146 LIU, K. *et al.* Evolution of interlayer coupling in twisted molybdenum disulfide bilayers. **Nature Communications**, v. 5, n. 1, p. 4966, 2014. DOI: 10.1038/ncomms5966.

147 WOOD, E. A. Vocabulary of surface crystallography. **Journal of Applied Physics**, v. 35, n. 4, p. 1306–1312, 1964. DOI: 10.1063/1.1713610.

148 PENG, Q. *et al.* Blue phosphorene/MS_2 (M = Nb, Ta) heterostructures as promising flexible anodes for lithium-ion batteries. **ACS Applied Materials & Interfaces**, v. 8, n. 21, p. 13449–13457, 2016. DOI: 10.1021/acsami.6b03368.

149 WANG, M. *et al.* van der Waals heterostructures of germanene, stanene, and silicene with hexagonal boron nitride and their topological domain walls. **Physical Review B**, v. 93, n. 15, p. 155412, 2016. DOI: 10.1103/PhysRevB.93.155412.

150 ATKINS, P.; de Paula, J. **Atkins' physical chemistry**. 8th ed. Oxford: Oxford University Press, 1994.

151 BENGTSSON, L. Dipole correction for surface supercell calculations. **Physical Review B**, v. 59, n. 19, p. 12301, 1999. DOI: 10.1103/PhysRevB.59.12301.

152 CHENG, K. *et al.* Carrier dynamics and transfer across the CdS/MoS_2 interface upon optical excitation. **Journal of Physical Chemistry Letters**, v. 11, n. 16, p. 6544–6550, 2020. DOI: 10.1021/acs.jpclett.0c01188.

153 TENGNER, S. Über diselenide und ditelluride von eisen, kobalt und nickel. **Zeitschrift für Anorganische und Allgemeine Chemie**, v. 239, n. 2, p. 126–132, 1938. DOI: 10.1002/zaac.19382390203.

154 LUTZ, H. *et al.* Structure refinement of pyrite-type ruthenium disulfide, RuS_2, and ruthenium diselenide, $RuSe_2$. **Acta Crystallographica C**, v. 46, n. 11, p. 2003–2005, 1990. DOI: 10.1107/S0108270190001925.

155 LUTZ, H.; JUNG, M.; WÄSCHENBACH, G. Kristallstrukturen des löllingits $FeAs_2$ und des pyrits $RuTe_2$. **Zeitschrift für Anorganische und Allgemeine Chemie**, v. 554, n. 11, p. 87–91, 1987. DOI: 10.1002/zaac.19875541110.

156 ZHAO, H.; SCHILS, H.; RAUB, C. J. Untersuchungen im system ruthenium-selen-tellur. **Journal of the Less Common Metals**, v. 113, n. 1, p. 75–82, 1985. DOI: 10.1016/0022-5088(85)90149-3.

157 STINGL, T.; MÜLLER, B.; LUTZ, H. Crystal structure refinement of osmium (II) disulfide, OsS_2. **Zeitschrift für Kristallographie – crystalline materials**, v. 202, n. 1-4, p. 161–162, 1992. DOI: 10.1524/zkri.1992.202.14.161.

158 STASSEN, W.; HEYDING, R. Crystal structures of $RuSe_2$, $OsSe_2$, $PtAs_2$, and α-$NiAs_2$. **Canadian Journal of Chemistry**, v. 46, n. 12, p. 2159–2163, 1968. DOI: 10.1139/v68-351.

159 GELLER, S.; CETLIN, B. The crystal structure of $RhSe_2$. **Acta Crystallographica**, v. 8, n. 5, p. 272–274, 1955. DOI: 10.1107/S0365110X5500087X.

160 HULLIGER, F. Crystal structure and electrical properties of some cobalt-group chalcogenides. **Nature**, v. 204, n. 4959, p. 644, 1964. DOI: 10.1038/204644a0.

161 GELLER, S. The crystal structures of RhTe and $RhTe_2$. **Journal of the American Chemical Society**, v. 77, n. 9, p. 2641–2644, 1955. DOI: 10.1021/ja01614a091.

162 MUNSON, R. A. The synthesis of iridium disulfide and nickel diarsenide having the pyrite structure. **Inorganic Chemistry**, v. 7, n. 2, p. 389–390, 1968. DOI: 10.1021/ic50060a047.

163 FURUSETH, S.; SELTE, K.; KJEKSHUS, A. Redetermined crystal structures of $NiTe_2$, $PdTe_2$, PtS_2, $PtSe_2$, and $PtTe_2$. **Acta Chemica Scandinavica**, v. 19, n. 1, p. 257–258, 1965. DOI: 10.3891/acta.chem.scand.19-0257.

164 KJEKSHUS, A.; RAKKE, T. Preparations and properties of magnesium, copper, zinc and cadmium dichalcogenides. **Acta Chemica Scandinavica**, v. 302, n. 4377/79, p. 617–620, 1979. DOI: 10.3891/acta.chem.scand.33a-0617.

APPENDIX

APPENDIX A – COMPUTATIONAL PARAMETERS

All calculations employed a total energy convergence criterion of 10^{-6} eV was used for the self-consistent solution of the KS equations. In VASP calculations of $MoSe_2$ for the studies of Chapter 3, the KS orbitals were expanded in a plane-wave basis set with a cutoff energy of 390 eV, except for stress tensor calculations, for bulks and monolayers, in which the cutoff energy was increased to 520 eV due to the slow convergence of the stress tensor with the size of basis set. These values of cutoff energy are 1.125 and 1.500 times larger than the maximum energy recommended for the employed PAW projectors (ENMAX parameter in the terminology of VASP PAW projectors), which were found adequate for the simulation of TMDs systems in a previous study.[132] Based on the same study, the **k**-points meshes for integrations in the FBZ were chosen, and 30 $Å^{-1}$ dense **k**-points meshes were employed for bulk solids. The same density was employed in the in-plane mesh for monolayers, and only the Γ-point was sampled in calculations of nanoflakes. To select the parameters for VASP calculations in the study of late TMs dichalcogenides discussed in Chapter 4, convergence tests were performed with two representative systems, pyrite-FeS_2 and 1T-$NiTe_2$, as shown in Figure 29. Based on the results, the parameters employed were cutoff energy of 690 eV to obtain equilibrium volumes and 490 eV for the remaining calculations, which correspond to 1.750 and 1.250 times the largest ENMAX among all the employed PAW projectors. Numerical integrations in the BZ were carried out with 40 $Å^{-1}$ dense **k**-points meshes, but the density was cut in half for HSE06 calculations due to the high computational cost. The calculations related to the discussions of Chapter 5 employed a cutoff energy of 438 eV, which was set based on the highest ENMAX among the chemical species, defining the cutoff energy as 1.125×ENMAX. To obtain equilibrium geometries, the cutoff energy was increased based on the convergence tests shown in Figure 30, and stress tensor calculations were performed with cutoff energy of 780 eV (2.0×ENMAX). To choose the **k**-mesh for Brillouin Zone integrations, convergence tests were performed with the 1T-$NiSe_2$ monolayer, which is the system with smallest band gap. Based on the results, shown in Figure 30, a density of 40 $Å^{-1}$ was employed. For the calculations performed with SIESTA, electron wave functions were expanded in a basis set of double-ζ plus polarization LCAO, associated with an energy shift $\delta\epsilon_l$ of 50 meV, and split norm of 0.15 for the generation of the double-ζ functions. The same **k**-point mesh density used for the study of vdW heterobilayers was employed, except in the TDDFT simulations, which employed only the Γ-point, as is explained in Chapter 6. The time-step of TDDFT and MD simulations was 24.19 as.

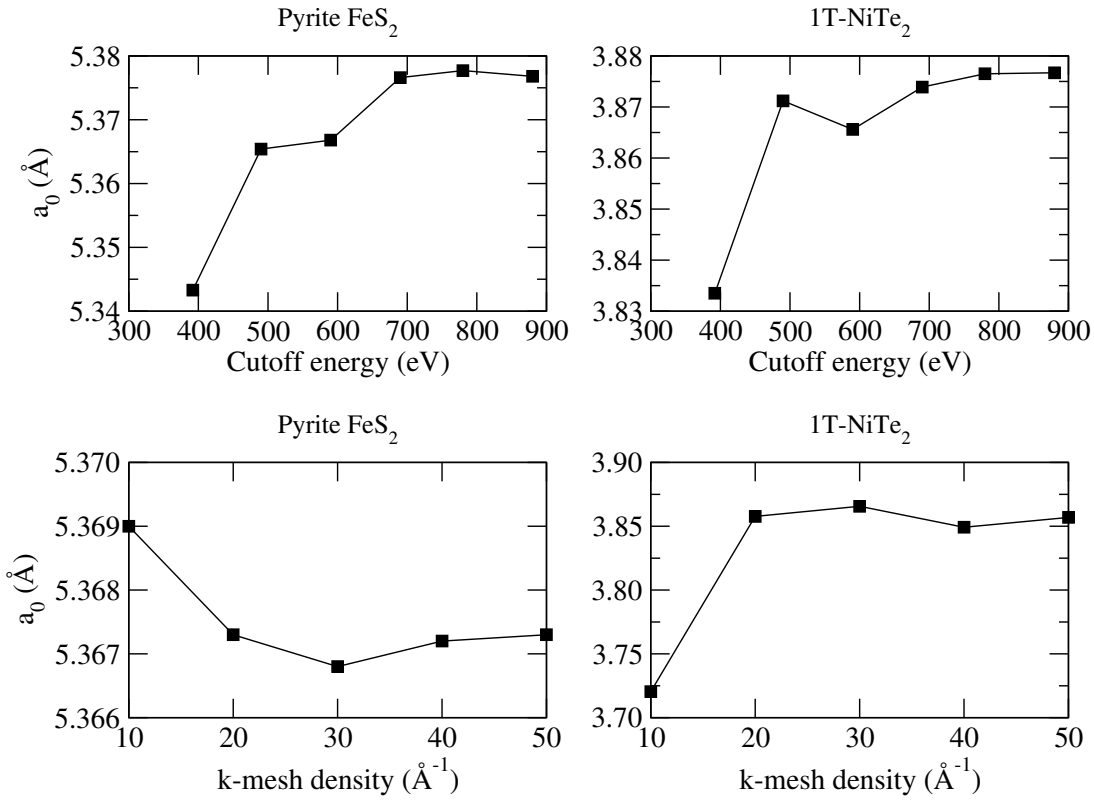

Figure 29 – Convergence tests of the cutoff energy and **k**-points mesh for representative systems in the study of late TMs dichalcogenides.

Source: By the author.

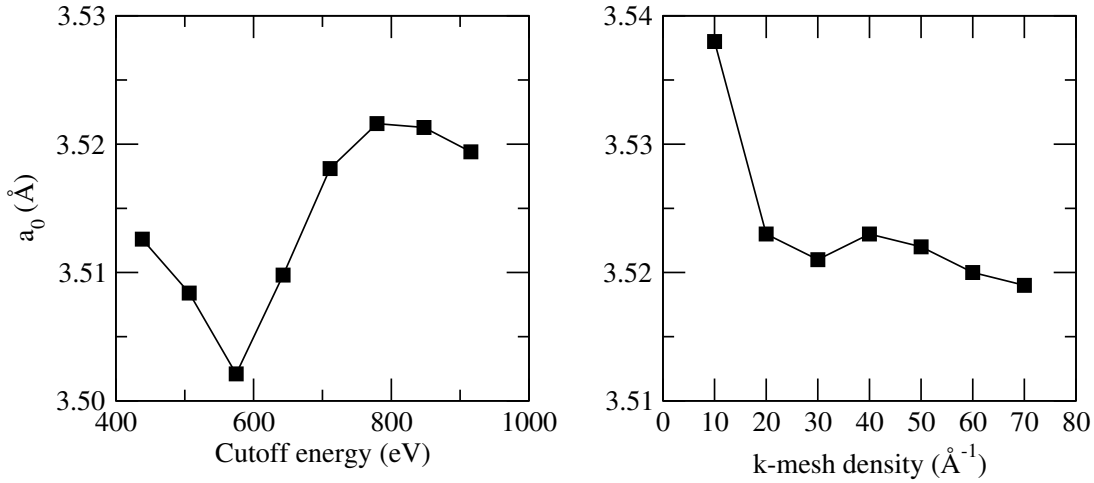

Figure 30 – Convergence tests of the cutoff energy and **k**-points mesh for the 1T-$NiSe_2$ monolayer, employed to define the parameters for the study of heterobilayers.

Source: By the author.

APPENDIX B – SUPPLEMENTARY DATA: DICHALCOGENIDES OF Fe-, Co-, Ni-, AND Cu-GROUPS

Table 9 – Equilibrium lattice parameters and relative total energies of FeS_2 in the 11 studied crystal structures, obtained with PBE+D3, and reference experimental data. The PdS_2-type structure is changed to pyrite after relaxation.

Structure	a_0 (Å)	b_0 (Å)	c_0 (Å)	α (°)	β (°)	γ (°)	ΔE (meV/f.u.)
1T	3.26	3.26	5.09	90.0	90.0	120.0	832
1T′	5.29	3.23	11.19	90.0	90.0	90.0	608
2H	3.14	3.14	11.58	90.0	90.0	120.0	979
Calaverite	5.70	3.23	5.09	90.0	89.7	90.0	831
PdS_2-type	5.38	5.38	5.38	90.0	90.0	90.0	16
Pyrite	5.38	5.38	5.38	90.0	90.0	90.0	17
Pyrite (Exp.)	5.42	5.42	5.42	90.0	90.0	90.0	
distorted-Pyrite	5.38	5.38	5.38	90.0	90.0	90.0	17
distorted-Pyrite (Exp.)	5.42	5.42	5.42	90.0	90.0	90.0	
Marcasite	4.41	5.38	3.38	90.0	90.0	90.0	0
Marcasite (Exp.)	4.44	5.39	3.37	90.0	90.0	90.0	
Krennerite	14.23	7.68	3.27	90.0	90.0	90.0	1074
IrS_2-type	17.76	3.40	5.44	90.0	90.0	90.0	236
$IrTe_2$-type	16.55	3.40	4.47	90.0	82.2	90.0	300

Source: BITHER *et al.*;[51] BESSE; LIMA; DA SILVA;[118] BAYLISS.[124]

Table 10 – Equilibrium lattice parameters and relative total energies of $FeSe_2$ in the 11 studied crystal structures, obtained with PBE+D3, and reference experimental data. The PdS_2-type structure is changed to pyrite after relaxation.

Structure	a_0 (Å)	b_0 (Å)	c_0 (Å)	α (°)	β (°)	γ (°)	ΔE (meV/f.u.)
1T	3.43	3.43	5.33	90.0	90.0	120.0	533
1T′	5.55	3.41	11.28	90.0	90.0	90.0	334
2H	3.27	3.27	12.14	90.0	90.0	120.0	611
Calaverite	6.05	3.35	5.32	90.0	88.5	90.0	526
PdS_2-type	5.74	5.74	5.74	90.0	90.0	90.0	56
Pyrite	5.74	5.74	5.74	90.0	90.0	90.0	56
Pyrite (Exp.)	5.79	5.79	5.79	90.0	90.0	90.0	
distorted-Pyrite	5.74	5.74	5.74	90.0	90.0	90.0	56
Marcasite	4.75	5.74	3.58	90.0	90.0	90.0	0
Marcasite (Exp.)	4.80	5.78	3.58	90.0	90.0	90.0	
Krennerite	15.51	8.21	3.34	90.0	90.0	90.0	807
IrS_2-type	19.21	3.60	5.80	90.0	90.0	90.0	226
$IrTe_2$-type	17.62	3.59	4.83	90.0	83.8	90.0	286

Source: BITHER *et al.*;[51] BESSE; LIMA; DA SILVA;[118] KJEKSHUS; RAKKE; ANDRESEN.[125]

Table 11 – Equilibrium lattice parameters and relative total energies of $FeTe_2$ in the 11 studied crystal structures, obtained with PBE+D3, and reference experimental data. The PdS_2-type structure is changed to pyrite after relaxation.

Structure	a_0 (Å)	b_0 (Å)	c_0 (Å)	α (°)	β (°)	γ (°)	ΔE (meV/f.u.)
1T	3.71	3.71	5.62	90.0	90.0	120.0	501
1T′	5.92	3.69	12.12	90.0	90.0	90.0	333
2H	3.72	3.72	12.53	90.0	90.0	120.0	606
Calaverite	6.42	3.73	5.60	90.0	90.3	90.0	499
PdS_2-type	6.22	6.22	6.22	90.0	90.0	90.0	97
Pyrite	6.21	6.21	6.21	90.0	90.0	90.0	97
Pyrite (Exp.)	6.29	6.29	6.29	90.0	90.0	90.0	
distorted-Pyrite	6.22	6.22	6.22	90.0	90.0	90.0	97
Marcasite	5.18	6.20	3.86	90.0	90.0	90.0	0
Marcasite (Exp.)	5.34	6.26	3.85	90.0	90.0	90.0	
Krennerite	16.69	8.68	3.73	90.0	90.0	90.0	650
IrS_2-type	21.06	3.87	6.27	90.0	90.0	90.0	220
$IrTe_2$-type	19.06	3.80	5.30	90.0	86.8	90.0	277

Source: BITHER *et al.*;[51] BESSE; LIMA; DA SILVA;[118] TENGNER.[153]

Table 12 – Equilibrium lattice parameters and relative total energies of RuS_2 in the 11 studied crystal structures, obtained with PBE+D3, and reference experimental data. The PdS_2-type structure is changed to pyrite after relaxation.

Structure	a_0 (Å)	b_0 (Å)	c_0 (Å)	α (°)	β (°)	γ (°)	ΔE (meV/f.u.)
1T	3.41	3.41	4.90	90.0	90.0	120.0	1349
1T′	5.54	3.46	11.00	90.0	90.0	90.0	783
2H	3.30	3.30	11.26	90.0	90.0	120.0	1566
Calaverite	6.53	3.03	4.86	90.0	91.8	90.0	1200
PdS_2-type	5.62	5.62	5.62	90.0	90.0	90.0	0
Pyrite	5.62	5.62	5.62	90.0	90.0	90.0	0
Pyrite (Exp.)	5.61	5.61	5.61	90.0	90.0	90.0	
distorted-Pyrite	5.62	5.62	5.62	90.0	90.0	90.0	0
Marcasite	4.54	5.64	3.59	90.0	90.0	90.0	115
Krennerite	15.18	8.20	3.08	90.0	90.0	90.0	1409
IrS_2-type	18.28	3.61	5.68	90.0	90.0	90.0	359
$IrTe_2$-type	17.36	3.61	4.57	90.0	81.6	90.0	437

Source: BESSE; LIMA; DA SILVA;[118] LUTZ *et al.*[154]

Table 13 – Equilibrium lattice parameters and relative total energies of $RuSe_2$ in the 11 studied crystal structures, obtained with PBE+D3, and reference experimental data. The PdS_2-type structure is changed to pyrite after relaxation.

Structure	a_0 (Å)	b_0 (Å)	c_0 (Å)	α (°)	β (°)	γ (°)	ΔE (meV/f.u.)
1T	3.57	3.57	5.20	90.0	90.0	120.0	992
1T′	5.76	3.61	11.50	90.0	90.0	90.0	455
2H	3.44	3.44	11.85	90.0	90.0	120.0	1118
Calaverite	6.27	3.52	5.21	90.0	89.4	90.0	993
PdS_2-type	5.96	5.96	5.96	90.0	90.0	90.0	0
Pyrite	5.96	5.96	5.96	90.0	90.0	90.0	0
Pyrite (Exp.)	5.93	5.93	5.93	90.0	90.0	90.0	
distorted-Pyrite	5.96	5.96	5.96	90.0	90.0	90.0	0
Marcasite	4.86	5.98	3.78	90.0	90.0	90.0	79
Krennerite	16.91	8.56	3.13	90.0	90.0	90.0	1070
IrS_2-type	19.65	3.75	5.98	90.0	90.0	90.0	444
$IrTe_2$-type	18.39	3.79	4.92	90.0	82.8	90.0	401

Source: BESSE; LIMA; DA SILVA.[118]

Table 14 – Equilibrium lattice parameters and relative total energies of $RuTe_2$ in the 11 studied crystal structures, obtained with PBE+D3, and reference experimental data. The PdS_2-type structure is changed to pyrite after relaxation.

Structure	a_0 (Å)	b_0 (Å)	c_0 (Å)	α (°)	β (°)	γ (°)	ΔE (meV/f.u.)
1T	3.82	3.82	5.58	90.0	90.0	120.0	807
1T′	6.09	3.86	12.13	90.0	90.0	90.0	440
2H	3.69	3.69	12.48	90.0	90.0	120.0	970
Calaverite	6.63	3.81	5.58	90.0	90.0	90.0	807
PdS_2-type	6.41	6.41	6.41	90.0	90.0	90.0	0
Pyrite	6.41	6.41	6.41	90.0	90.0	90.0	0
Pyrite (Exp.)	6.39	6.39	6.39	90.0	90.0	90.0	
distorted-Pyrite	6.41	6.41	6.41	90.0	90.0	90.0	0
Marcasite	5.27	6.42	4.04	90.0	90.0	90.0	31
Marcasite (Exp.)	5.29	6.40	4.01	90.0	90.0	90.0	
Krennerite	19.02	8.95	3.27	90.0	90.0	90.0	986
IrS_2-type	21.38	4.06	6.49	90.0	90.0	90.0	291
$IrTe_2$-type	19.69	4.06	5.36	90.0	83.7	90.0	361

Source: BESSE; LIMA; DA SILVA;[118] LUTZ; JUNG; WÄSCHENBACH;[155] ZHAO; SCHILS; RAUB.[156]

Table 15 – Equilibrium lattice parameters and relative total energies of OsS_2 in the 11 studied crystal structures, obtained with PBE+D3, and reference experimental data. The PdS_2-type structure is changed to pyrite after relaxation.

Structure	a_0 (Å)	b_0 (Å)	c_0 (Å)	α (°)	β (°)	γ (°)	ΔE (meV/f.u.)
1T	3.48	3.48	4.96	90.0	90.0	120.0	1282
1T′	5.52	3.53	11.07	90.0	90.0	90.0	529
2H	3.34	3.34	11.20	90.0	90.0	120.0	1618
Calaverite	6.57	3.04	4.98	90.0	89.9	90.0	1072
PdS_2-type	5.64	5.64	5.64	90.0	90.0	90.0	0
Pyrite	5.64	5.64	5.64	90.0	90.0	90.0	0
Pyrite (Exp.)	5.62	5.62	5.62	90.0	90.0	90.0	
distorted-Pyrite	5.64	5.64	5.64	90.0	90.0	90.0	0
Marcasite	4.55	5.66	3.63	90.0	90.0	90.0	85
Krennerite	16.08	8.13	3.03	90.0	90.0	90.0	1355
IrS_2-type	18.36	3.64	5.69	90.0	90.0	90.0	374
$IrTe_2$-type	17.41	3.65	4.58	90.0	81.9	90.0	462

Source: BESSE; LIMA; DA SILVA;[118] STINGL; MÜLLER; LUTZ.[157]

Table 16 – Equilibrium lattice parameters and relative total energies of $OsSe_2$ in the 11 studied crystal structures, obtained with PBE+D3, and reference experimental data. The PdS_2-type structure is changed to pyrite after relaxation.

Structure	a_0 (Å)	b_0 (Å)	c_0 (Å)	α (°)	β (°)	γ (°)	ΔE (meV/f.u.)
1T	3.64	3.64	5.20	90.0	90.0	120.0	1012
1T′	5.74	3.68	11.58	90.0	90.0	90.0	276
2H	3.48	3.48	11.79	90.0	90.0	120.0	1203
Calaverite	6.35	3.61	5.19	90.0	89.6	90.0	1010
PdS_2-type	5.98	5.98	5.98	90.0	90.0	90.0	0
Pyrite	5.98	5.98	5.98	90.0	90.0	90.0	0
Pyrite (Exp.)	5.95	5.95	5.95	90.0	90.0	90.0	
distorted-Pyrite	5.98	5.98	5.98	90.0	90.0	90.0	0
Marcasite	4.86	5.99	3.82	90.0	90.0	90.0	58
Krennerite	15.03	8.65	3.74	90.0	90.0	90.0	926
IrS_2-type	19.75	3.83	6.04	90.0	90.0	90.0	340
$IrTe_2$-type	18.42	3.83	4.93	90.0	83.3	90.0	420

Source: BESSE; LIMA; DA SILVA;[118] STASSEN; HEYDING.[158]

Table 17 – Equilibrium lattice parameters and relative total energies of $OsTe_2$ in the 11 studied crystal structures, obtained with PBE+D3, and reference experimental data. The PdS_2-type structure is changed to pyrite after relaxation.

Structure	a_0 (Å)	b_0 (Å)	c_0 (Å)	α (°)	β (°)	γ (°)	ΔE (meV/f.u.)
1T	3.88	3.88	5.54	90.0	90.0	120.0	914
1T′	6.08	3.92	12.23	90.0	90.0	90.0	416
2H	3.72	3.72	12.50	90.0	90.0	120.0	1101
Calaverite	6.72	3.88	5.54	90.0	90.2	90.0	918
PdS_2-type	6.42	6.42	6.42	90.0	90.0	90.0	0
Pyrite	6.42	6.42	6.42	90.0	90.0	90.0	0
Pyrite (Exp.)	6.40	6.40	6.40	90.0	90.0	90.0	
distorted-Pyrite	6.42	6.42	6.42	90.0	90.0	90.0	0
Marcasite	5.26	6.43	4.08	90.0	90.0	90.0	24
Krennerite	16.09	9.08	4.00	90.0	90.0	90.0	988
IrS_2-type	21.40	4.09	6.49	90.0	90.0	90.0	310
$IrTe_2$-type	19.71	4.10	5.36	90.0	84.1	90.0	381

Source: BESSE; LIMA; DA SILVA;[118] STINGL; MÜLLER; LUTZ.[157]

Table 18 – Equilibrium lattice parameters and relative total energies of CoS_2 in the 11 studied crystal structures, obtained with PBE+D3, and reference experimental data. The PdS_2-type structure is changed to pyrite after relaxation.

Structure	a_0 (Å)	b_0 (Å)	c_0 (Å)	α (°)	β (°)	γ (°)	ΔE (meV/f.u.)
1T	3.30	3.30	4.61	90.0	90.0	120.0	309
1T′	5.62	3.31	9.88	90.0	90.0	90.0	396
2H	3.22	3.22	10.53	90.0	90.0	120.0	867
Calaverite	5.77	3.27	4.62	90.0	90.3	90.0	310
PdS_2-type	5.47	5.47	5.46	90.0	90.0	90.0	0
Pyrite	5.47	5.47	5.47	90.0	90.0	90.0	0
Pyrite (Exp.)	5.53	5.53	5.53	90.0	90.0	90.0	
distorted-Pyrite	5.47	5.47	5.47	90.0	90.0	90.0	0
Marcasite	4.48	5.45	3.45	90.0	90.0	90.0	25
Krennerite	13.74	7.57	3.28	90.0	90.0	90.0	484
IrS_2-type	18.95	3.36	5.40	90.0	90.0	90.0	13
$IrTe_2$-type	16.81	3.35	4.46	90.0	89.9	90.0	7

Source: BITHER *et al.*;[51] BESSE; LIMA; DA SILVA.[118]

Table 19 – Equilibrium lattice parameters and relative total energies of $CoSe_2$ in the 11 studied crystal structures, obtained with PBE+D3, and reference experimental data. The PdS_2-type structure is changed to pyrite after relaxation.

Structure	a_0 (Å)	b_0 (Å)	c_0 (Å)	α (°)	β (°)	γ (°)	ΔE (meV/f.u.)
1T	3.48	3.48	4.96	90.0	90.0	120.0	175
1T′	5.92	3.47	10.48	90.0	90.0	90.0	242
2H	3.36	3.36	11.18	90.0	90.0	120.0	635
Calaverite	6.00	3.49	4.97	90.0	90.5	90.0	175
PdS_2-type	5.78	5.78	5.78	90.0	90.0	90.0	69
Pyrite	5.78	5.78	5.78	90.0	90.0	90.0	69
Pyrite (Exp.)	5.86	5.86	5.86	90.0	90.0	90.0	
distorted-Pyrite	5.78	5.78	5.78	90.0	90.0	90.0	69
Marcasite	4.82	5.77	3.62	90.0	90.0	90.0	61
Krennerite	14.55	8.10	3.50	90.0	90.0	90.0	383
IrS_2-type	19.93	3.58	5.75	90.0	90.0	90.0	30
$IrTe_2$-type	17.82	3.55	4.79	90.0	89.8	90.0	0

Source: BITHER *et al.*;[51] BESSE; LIMA; DA SILVA.[118]

Table 20 – Equilibrium lattice parameters and relative total energies of $CoTe_2$ in the 11 studied crystal structures, obtained with PBE+D3, and reference experimental data. The PdS_2-type structure is changed to pyrite after relaxation.

Structure	a_0 (Å)	b_0 (Å)	c_0 (Å)	α (°)	β (°)	γ (°)	ΔE (meV/f.u.)
1T	3.76	3.76	5.32	90.0	90.0	120.0	63
1T′	6.42	3.74	11.27	90.0	90.0	90.0	133
2H	3.61	3.61	12.03	90.0	90.0	120.0	484
Calaverite	6.52	3.76	5.33	90.0	90.1	90.0	60
PdS_2-type	6.24	6.24	6.24	90.0	90.0	90.0	44
Pyrite	6.24	6.24	6.24	90.0	90.0	90.0	44
Pyrite (Exp.)	6.32	6.32	6.32	90.0	90.0	90.0	
distorted-Pyrite	6.24	6.24	6.24	90.0	90.0	90.0	44
Marcasite	5.27	6.23	3.89	90.0	90.0	90.0	62
Marcasite (Exp.)	5.30	6.30	3.88	90.0	90.0	90.0	
Krennerite	15.85	8.73	3.79	90.0	90.0	90.0	303
IrS_2-type	21.61	3.86	6.21	90.0	90.0	90.0	36
$IrTe_2$-type	19.25	3.84	5.18	90.0	90.3	90.0	0

Source: BITHER *et al.*;[51] BESSE; LIMA; DA SILVA;[118] TENGNER.[153]

Table 21 – Equilibrium lattice parameters and relative total energies of RhS_2 in the 11 studied crystal structures, obtained with PBE+D3. The PdS_2-type structure is changed to pyrite after relaxation.

Structure	a_0 (Å)	b_0 (Å)	c_0 (Å)	α (°)	β (°)	γ (°)	ΔE (meV/f.u.)
1T	3.49	3.49	4.68	90.0	90.0	120.0	421
1T′	6.20	3.42	9.84	90.0	90.0	90.0	549
2H	3.36	3.36	10.75	90.0	90.0	120.0	1379
Calaverite	6.10	3.46	4.67	90.0	90.8	90.0	419
PdS_2-type	5.71	5.71	5.72	90.0	90.0	90.0	128
Pyrite	5.71	5.71	5.71	90.0	90.0	90.0	128
distorted-Pyrite	5.71	5.71	5.71	90.0	90.0	90.0	128
Marcasite	4.63	5.66	3.69	90.0	90.0	90.0	212
Krennerite	14.30	7.89	3.44	90.0	90.0	90.0	551
IrS_2-type	19.78	3.56	5.64	90.0	90.0	90.0	0
$IrTe_2$-type	17.68	3.57	4.59	90.0	90.1	90.0	58

Source: BESSE; LIMA; DA SILVA.[118]

Table 22 – Equilibrium lattice parameters and relative total energies of $RhSe_2$ in the 11 studied crystal structures, obtained with PBE+D3, and reference experimental data. The PdS_2-type structure is changed to pyrite after relaxation.

Structure	a_0 (Å)	b_0 (Å)	c_0 (Å)	α (°)	β (°)	γ (°)	ΔE (meV/f.u.)
1T	3.65	3.65	4.94	90.0	90.0	120.0	245
1T′	6.53	3.57	10.33	90.0	90.0	90.0	363
2H	3.50	3.50	11.30	90.0	90.0	120.0	965
Calaverite	6.45	3.61	4.94	90.0	91.3	90.0	250
PdS_2-type	6.04	6.03	6.03	90.0	90.0	90.0	53
Pyrite	6.03	6.03	6.03	90.0	90.0	90.0	53
Pyrite (Exp.)	5.99	5.99	5.99	90.0	90.0	90.0	
distorted-Pyrite	6.04	6.04	6.04	90.0	90.0	90.0	53
Marcasite	4.97	6.00	3.85	90.0	90.0	90.0	108
Krennerite	15.07	8.34	3.63	90.0	90.0	90.0	385
IrS_2-type	20.81	3.76	5.97	90.0	90.0	90.0	24
IrS_2-type (Exp.)	20.91	3.71	5.95	90.0	90.0	90.0	
$IrTe_2$-type	18.65	3.75	4.89	90.0	90.2	90.0	0

Source: BESSE; LIMA; DA SILVA;[118] GELLER; CETLIN;[159] HULLIGER.[160]

Table 23 – Equilibrium lattice parameters and relative total energies of $RhTe_2$ in the 11 studied crystal structures, obtained with PBE+D3, and reference experimental data. The PdS_2-type structure is changed to pyrite after relaxation.

Structure	a_0 (Å)	b_0 (Å)	c_0 (Å)	α (°)	β (°)	γ (°)	ΔE (meV/f.u.)
1T	3.94	3.94	5.24	90.0	90.0	120.0	122
1T (Exp.)	3.92	3.92	5.41	90.0	90.0	120.0	
1T′	6.75	3.90	11.25	90.0	90.0	90.0	263
2H	3.76	3.76	12.11	90.0	90.0	120.0	682
Calaverite	6.83	3.93	5.24	90.0	89.9	90.0	116
PdS_2-type	6.46	6.46	6.46	90.0	90.0	90.0	0
Pyrite	6.46	6.46	6.46	90.0	90.0	90.0	0
Pyrite (Exp.)	6.44	6.44	6.44	90.0	90.0	90.0	
distorted-Pyrite	6.46	6.46	6.46	90.0	90.0	90.0	0
Marcasite	5.40	6.45	4.10	90.0	90.0	90.0	109
Krennerite	16.04	8.90	3.96	90.0	90.0	90.0	299
IrS_2-type	22.22	4.05	6.42	90.0	90.0	90.0	55
$IrTe_2$-type	20.05	4.03	5.24	90.0	90.7	90.0	0

Source: BESSE; LIMA; DA SILVA;[118] GELLER.[161]

Table 24 – Equilibrium lattice parameters and relative total energies of IrS_2 in the 11 studied crystal structures, obtained with PBE+D3, and reference experimental data. The PdS_2-type structure is changed to pyrite after relaxation.

Structure	a_0 (Å)	b_0 (Å)	c_0 (Å)	α (°)	β (°)	γ (°)	ΔE (meV/f.u.)
1T	3.53	3.53	4.72	90.0	90.0	120.0	458
1T′	6.07	3.54	10.09	90.0	90.0	90.0	589
2H	3.38	3.38	10.85	90.0	90.0	120.0	1754
Calaverite	6.12	3.53	4.72	90.0	90.4	90.0	461
PdS_2-type	5.70	5.70	5.70	90.0	90.0	90.0	218
Pyrite	5.70	5.70	5.70	90.0	90.0	90.0	218
Pyrite (Exp.)	5.68	5.68	5.68	90.0	90.0	90.0	
distorted-Pyrite	5.70	5.70	5.70	90.0	90.0	90.0	218
Marcasite	4.78	5.66	3.65	90.0	90.0	90.0	253
Krennerite	14.43	7.93	3.50	90.0	90.0	90.0	697
IrS_2-type	19.80	3.60	5.63	90.0	90.0	90.0	0
IrS_2-type (Exp.)	19.78	3.57	5.62	90.0	90.0	90.0	
$IrTe_2$-type	17.69	3.60	4.62	90.0	90.1	90.0	99

Source: BESSE; LIMA; DA SILVA;[118] HULLIGER;[160] MUNSON.[162]

Table 25 – Equilibrium lattice parameters and relative total energies of $IrSe_2$ in the 11 studied crystal structures, obtained with PBE+D3, and reference experimental data. The PdS_2-type structure is changed to pyrite after relaxation.

Structure	a_0 (Å)	b_0 (Å)	c_0 (Å)	α (°)	β (°)	γ (°)	ΔE (meV/f.u.)
1T	3.70	3.70	4.97	90.0	90.0	120.0	265
1T′	6.50	3.64	10.46	90.0	90.0	90.0	395
2H	3.52	3.52	11.42	90.0	90.0	120.0	1248
Calaverite	6.42	3.69	4.96	90.0	90.3	90.0	266
PdS_2-type	6.04	6.04	6.04	90.0	90.0	90.0	207
Pyrite	6.04	6.04	6.04	90.0	90.0	90.0	207
distorted-Pyrite	6.04	6.04	6.04	90.0	90.0	90.0	207
Marcasite	5.04	6.00	3.85	90.0	90.0	90.0	224
Krennerite	15.18	8.35	3.68	90.0	90.0	90.0	483
IrS_2-type	20.97	3.78	5.96	90.0	90.0	90.0	0
IrS_2-type (Exp.)	20.96	3.74	5.94	90.0	90.0	90.0	
$IrTe_2$-type	18.65	3.78	4.91	90.0	90.3	90.0	22

Source: BESSE; LIMA; DA SILVA;[118] JOBIC *et al.*[126]

Table 26 – Equilibrium lattice parameters and relative total energies of $IrTe_2$ in the 11 studied crystal structures, obtained with PBE+D3, and reference experimental data. The PdS_2-type structure is changed to pyrite after relaxation.

Structure	a_0 (Å)	b_0 (Å)	c_0 (Å)	α (°)	β (°)	γ (°)	ΔE (meV/f.u.)
1T	3.96	3.96	5.27	90.0	90.0	120.0	121
1T (Exp.)	3.93	3.93	5.39	90.0	90.0	120.0	
1T′	6.84	3.91	11.31	90.0	90.0	90.0	279
2H	3.77	3.77	12.15	90.0	90.0	120.0	886
Calaverite	6.84	3.97	5.26	90.0	90.1	90.0	120
PdS_2-type	6.48	6.48	6.48	90.0	90.0	90.0	150
Pyrite	6.48	6.48	6.48	90.0	90.0	90.0	150
distorted-Pyrite	6.48	6.48	6.48	90.0	90.0	90.0	150
Marcasite	5.44	6.45	4.12	90.0	90.0	90.0	249
Krennerite	16.21	8.92	3.96	90.0	90.0	90.0	344
IrS_2-type	22.58	4.05	6.40	90.0	90.0	90.0	41
$IrTe_2$-type	20.06	4.04	5.27	90.0	90.8	90.0	0
$IrTe_2$-type (Exp.)	19.98	4.00	5.31	90.0	90.8	90.0	

Source: HOCKINGS; WHITE;[49] BESSE; LIMA; DA SILVA;[118] JOBIC *et al.*[127]

Table 27 – Equilibrium lattice parameters and relative total energies of NiS_2 in the 11 studied crystal structures, obtained with PBE+D3, and reference experimental data. The PdS_2-type structure is changed to pyrite after relaxation.

Structure	a_0 (Å)	b_0 (Å)	c_0 (Å)	α (°)	β (°)	γ (°)	ΔE (meV/f.u.)
1T	3.39	3.39	4.44	90.0	90.0	120.0	152
1T′	5.81	3.38	9.61	90.0	90.0	90.0	219
2H	3.47	3.47	9.79	90.0	90.0	120.0	728
Calaverite	5.87	3.39	4.43	90.0	90.1	90.0	152
PdS_2-type	5.57	5.57	5.58	90.0	90.0	90.0	0
Pyrite	5.57	5.57	5.57	90.0	90.0	90.0	0
Pyrite (Exp.)	5.69	5.69	5.69	90.0	90.0	90.0	
distorted-Pyrite	5.57	5.57	5.57	90.0	90.0	90.0	0
Marcasite	4.55	5.55	3.52	90.0	90.0	90.0	31
Krennerite	13.76	7.44	3.37	90.0	90.0	90.0	311
IrS_2-type	18.80	3.34	6.13	90.0	90.0	90.0	133
$IrTe_2$-type	17.95	3.39	4.42	90.0	88.1	90.0	103

Source: BITHER *et al.*;[51] BESSE; LIMA; DA SILVA.[118]

Table 28 – Equilibrium lattice parameters and relative total energies of $NiSe_2$ in the 11 studied crystal structures, obtained with PBE+D3, and reference experimental data. The PdS_2-type structure is changed to pyrite after relaxation.

Structure	a_0 (Å)	b_0 (Å)	c_0 (Å)	α (°)	β (°)	γ (°)	ΔE (meV/f.u.)
1T	3.59	3.59	4.68	90.0	90.0	120.0	0
1T′	6.19	3.56	9.92	90.0	90.0	90.0	68
2H	3.47	3.47	10.61	90.0	90.0	120.0	522
Calaverite	6.21	3.59	4.69	90.0	89.8	90.0	0
PdS_2-type	5.88	5.88	5.87	90.0	90.0	90.0	33
Pyrite	5.87	5.87	5.87	90.0	90.0	90.0	33
Pyrite (Exp.)	5.96	5.96	5.96	90.0	90.0	90.0	
distorted-Pyrite	5.87	5.87	5.87	90.0	90.0	90.0	33
Marcasite	4.85	5.95	3.67	90.0	90.0	90.0	54
Krennerite	14.64	7.91	3.60	90.0	90.0	90.0	138
IrS_2-type	19.86	3.65	5.92	90.0	90.0	90.0	77
$IrTe_2$-type	18.30	3.60	4.80	90.0	89.9	90.0	20

Source: BITHER *et al.*;[51] BESSE; LIMA; DA SILVA.[118]

Table 29 – Equilibrium lattice parameters and relative total energies of $NiTe_2$ in the 11 studied crystal structures, obtained with PBE+D3, and reference experimental data. The PdS_2-type structure is changed to pyrite after relaxation.

Structure	a_0 (Å)	b_0 (Å)	c_0 (Å)	α (°)	β (°)	γ (°)	ΔE (meV/f.u.)
1T	3.86	3.86	5.08	90.0	90.0	120.0	4
1T (Exp.)	3.85	3.85	5.26	90.0	90.0	120.0	
1T′	6.66	3.84	10.72	90.0	90.0	90.0	82
2H	3.69	3.69	11.64	90.0	90.0	120.0	373
Calaverite	6.71	3.86	5.07	90.0	90.3	90.0	0
PdS_2-type	6.34	6.34	6.34	90.0	90.0	90.0	77
Pyrite	6.34	6.34	6.34	90.0	90.0	90.0	78
Pyrite (Exp.)	6.37	6.37	6.37	90.0	90.0	90.0	
distorted-Pyrite	6.34	6.34	6.33	90.0	90.0	90.0	78
Marcasite	5.27	6.44	3.93	90.0	90.0	90.0	140
Krennerite	15.98	8.52	3.88	90.0	90.0	90.0	126
IrS_2-type	21.72	3.90	6.38	90.0	90.0	90.0	145
$IrTe_2$-type	19.69	3.89	5.20	90.0	90.2	90.0	69

Source: BITHER *et al.*;[51] BESSE; LIMA; DA SILVA.[118]

Table 30 – Equilibrium lattice parameters and relative total energies of PdS_2 in the 11 studied crystal structures, obtained with PBE+D3, and reference experimental data.

Structure	a_0 (Å)	b_0 (Å)	c_0 (Å)	α (°)	β (°)	γ (°)	ΔE (meV/f.u.)
1T	3.60	3.60	4.45	90.0	90.0	120.0	261
1T′	6.18	3.57	9.88	90.0	90.0	90.0	358
2H	3.87	3.87	9.53	90.0	90.0	120.0	1143
Calaverite	6.24	3.60	4.46	90.0	89.9	90.0	263
PdS_2-type	5.52	5.59	7.46	90.0	90.0	90.0	0
PdS_2-type (Exp.)	5.46	5.54	7.53	90.0	90.0	90.0	
Pyrite	5.90	5.90	5.90	90.0	90.0	90.0	77
distorted-Pyrite	5.90	5.89	5.90	90.0	90.0	90.0	77
Marcasite	4.77	5.78	3.81	90.0	90.0	90.0	129
Krennerite	14.17	7.76	3.56	90.0	90.0	90.0	419
IrS_2-type	19.30	3.56	6.56	90.0	90.0	90.0	286
$IrTe_2$-type	21.71	3.53	4.39	90.0	88.8	90.0	174

Source: BESSE; LIMA; DA SILVA;[118] GRØNVOLD; RØST.[122]

Table 31 – Equilibrium lattice parameters and relative total energies of $PdSe_2$ in the 11 studied crystal structures, obtained with PBE+D3, and reference experimental data. The PdS_2-type structure is changed to pyrite after relaxation.

Structure	a_0 (Å)	b_0 (Å)	c_0 (Å)	α (°)	β (°)	γ (°)	ΔE (meV/f.u.)
1T	3.79	3.79	4.67	90.0	90.0	120.0	0
1T′	6.51	3.77	10.05	90.0	90.0	90.0	139
2H	3.62	3.62	10.72	90.0	90.0	120.0	827
Calaverite	6.57	3.78	4.68	90.0	90.0	90.0	1
PdS_2-type	6.20	6.21	6.19	90.0	90.0	90.0	49
PdS_2-type (Exp.)	5.74	5.87	7.69	90.0	90.0	90.0	
Pyrite	6.20	6.20	6.20	90.0	90.0	90.0	49
distorted-Pyrite	6.20	6.20	6.20	90.0	90.0	90.0	49
Marcasite	5.05	6.21	3.93	90.0	90.0	90.0	97
Krennerite	14.98	8.19	3.77	90.0	90.0	90.0	96
IrS_2-type	20.55	3.94	6.13	90.0	90.0	90.0	128
$IrTe_2$-type	19.51	3.83	4.86	90.0	90.6	90.0	65

Source: BESSE; LIMA; DA SILVA;[118] GRØNVOLD; RØST.[122]

Table 32 – Equilibrium lattice parameters and relative total energies of $PdTe_2$ in the 11 studied crystal structures, obtained with PBE+D3, and reference experimental data. The PdS_2-type structure is changed to pyrite after relaxation.

Structure	a_0 (Å)	b_0 (Å)	c_0 (Å)	α (°)	β (°)	γ (°)	ΔE (meV/f.u.)
1T	4.07	4.07	5.01	90.0	90.0	120.0	3
1T (Exp.)	4.03	4.03	5.13	90.0	90.0	120.0	
1T′	7.07	4.02	10.69	90.0	90.0	90.0	155
2H	3.87	3.87	11.58	90.0	90.0	120.0	549
Calaverite	7.04	4.08	5.02	90.0	89.5	90.0	0
PdS_2-type	6.61	6.61	6.61	90.0	90.0	90.0	101
Pyrite	6.61	6.61	6.61	90.0	90.0	90.0	101
distorted-Pyrite	6.61	6.61	6.61	90.0	90.0	90.0	101
Marcasite	5.42	6.77	4.16	90.0	90.0	90.0	206
Krennerite	16.17	8.78	4.08	90.0	90.0	90.0	87
IrS_2-type	22.29	4.15	6.63	90.0	90.0	90.0	222
$IrTe_2$-type	20.78	4.12	5.22	90.0	91.0	90.0	121

Source: BESSE; LIMA; DA SILVA;[118] FURUSETH; SELTE; KJEKSHUS.[163]

Table 33 – Equilibrium lattice parameters and relative total energies of PtS_2 in the 11 studied crystal structures, obtained with PBE+D3, and reference experimental data.

Structure	a_0 (Å)	b_0 (Å)	c_0 (Å)	α (°)	β (°)	γ (°)	ΔE (meV/f.u.)
1T	3.61	3.61	4.58	90.0	90.0	120.0	0
1T (Exp.)	3.54	3.54	5.04	90.0	90.0	120.0	
1T′	6.20	3.58	10.18	90.0	90.0	90.0	55
2H	3.45	3.45	10.34	90.0	90.0	120.0	1695
Calaverite	6.25	3.61	4.59	90.0	90.0	90.0	0
PdS_2-type	5.47	5.55	7.85	90.0	90.0	90.0	155
Pyrite	5.84	5.84	5.84	90.0	90.0	90.0	597
distorted-Pyrite	5.84	5.84	5.84	90.0	90.0	90.0	597
Marcasite	4.80	5.59	3.93	90.0	90.0	90.0	704
Krennerite	14.34	7.69	3.63	90.0	90.0	90.0	417
IrS_2-type	21.39	3.65	5.53	90.0	90.0	90.0	427
$IrTe_2$-type	17.20	3.65	5.16	90.0	91.6	90.0	365

Source: BESSE; LIMA; DA SILVA;[118] FURUSETH; SELTE; KJEKSHUS.[163]

Table 34 – Equilibrium lattice parameters and relative total energies of $PtSe_2$ in the 11 studied crystal structures, obtained with PBE+D3, and reference experimental data.

Structure	a_0 (Å)	b_0 (Å)	c_0 (Å)	α (°)	β (°)	γ (°)	ΔE (meV/f.u.)
1T	3.79	3.79	4.75	90.0	90.0	120.0	0
1T (Exp.)	3.73	3.73	5.04	90.0	90.0	120.0	
1T′	6.50	3.75	10.42	90.0	90.0	90.0	82
2H	3.61	3.61	10.90	90.0	90.0	120.0	1241
Calaverite	6.57	3.79	4.75	90.0	89.9	90.0	0
PdS_2-type	5.76	5.89	8.16	90.0	90.0	90.0	356
Pyrite	6.16	6.16	6.16	90.0	90.0	90.0	481
distorted-Pyrite	6.16	6.16	6.16	90.0	90.0	90.0	481
Marcasite	5.35	5.95	3.90	90.0	90.0	90.0	533
Krennerite	15.12	8.12	3.81	90.0	90.0	90.0	266
IrS_2-type	21.81	3.85	5.98	90.0	90.0	90.0	401
$IrTe_2$-type	19.09	3.85	4.98	90.0	92.5	90.0	328

Source: BESSE; LIMA; DA SILVA;[118] FURUSETH; SELTE; KJEKSHUS.[163]

Table 35 – Equilibrium lattice parameters and relative total energies of $PtTe_2$ in the 11 studied crystal structures, obtained with PBE+D3, and reference experimental data. The PdS_2-type structure is changed to pyrite after relaxation.

Structure	a_0 (Å)	b_0 (Å)	c_0 (Å)	α (°)	β (°)	γ (°)	ΔE (meV/f.u.)
1T	4.07	4.07	5.03	90.0	90.0	120.0	0
1T (Exp.)	4.03	4.03	5.22	90.0	90.0	120.0	
1T′	6.95	4.02	10.93	90.0	90.0	90.0	127
2H	3.84	3.84	11.68	90.0	90.0	120.0	827
Calaverite	7.04	4.06	5.05	90.0	89.9	90.0	4
PdS_2-type	6.60	6.60	6.63	90.0	90.0	90.0	376
Pyrite	6.61	6.61	6.61	90.0	90.0	90.0	376
distorted-Pyrite	6.61	6.61	6.61	90.0	90.0	90.0	376
Marcasite	5.37	6.81	4.18	90.0	90.0	90.0	519
Krennerite	16.35	8.69	4.07	90.0	90.0	90.0	170
IrS_2-type	22.83	3.99	7.08	90.0	90.0	90.0	375
$IrTe_2$-type	20.67	4.11	5.30	90.0	91.8	90.0	305

Source: BESSE; LIMA; DA SILVA;[118] FURUSETH; SELTE; KJEKSHUS.[163]

Table 36 – Equilibrium lattice parameters and relative total energies of CuS_2 in the 11 studied crystal structures, obtained with PBE+D3, and reference experimental data. The PdS_2-type structure is changed to pyrite after relaxation.

Structure	a_0 (Å)	b_0 (Å)	c_0 (Å)	α (°)	β (°)	γ (°)	ΔE (meV/f.u.)
1T	3.48	3.48	4.28	90.0	90.0	120.0	715
1T′	6.38	3.35	8.81	90.0	90.0	90.0	777
2H	3.67	3.67	9.09	90.0	90.0	120.0	894
Calaverite	6.31	3.41	4.29	90.0	90.7	90.0	671
PdS_2-type	5.75	5.75	5.76	90.0	90.0	90.0	0
Pyrite	5.75	5.75	5.75	90.0	90.0	90.0	0
Pyrite (Exp.)	5.79	5.79	5.79	90.0	90.0	90.0	
distorted-Pyrite	5.75	5.75	5.75	90.0	90.0	90.0	0
Marcasite	4.67	5.79	3.59	90.0	90.0	90.0	2
Marcasite (Exp.)	4.65	5.66	3.52	90.0	90.0	90.0	
Krennerite	13.77	7.50	3.97	90.0	90.0	90.0	211
IrS_2-type	18.68	3.60	5.83	90.0	90.0	90.0	51
$IrTe_2$-type	17.78	3.58	4.70	90.0	82.1	90.0	70

Source: BITHER *et al.*;[51] BESSE; LIMA; DA SILVA;[118] KJEKSHUS; RAKKE.[164]

Table 37 – Equilibrium lattice parameters and relative total energies of $CuSe_2$ in the 11 studied crystal structures, obtained with PBE+D3, and reference experimental data. The PdS_2-type structure is changed to pyrite after relaxation.

Structure	a_0 (Å)	b_0 (Å)	c_0 (Å)	α (°)	β (°)	γ (°)	ΔE (meV/f.u.)
1T	3.69	3.69	4.56	90.0	90.0	120.0	231
1T′	6.68	3.61	9.38	90.0	90.0	90.0	280
2H	3.75	3.75	9.76	90.0	90.0	120.0	533
Calaverite	6.66	3.69	4.53	90.0	90.7	90.0	188
PdS_2-type	6.09	6.09	6.09	90.0	90.0	90.0	0
Pyrite	6.09	6.09	6.09	90.0	90.0	90.0	0
Pyrite (Exp.)	6.12	6.12	6.12	90.0	90.0	90.0	
distorted-Pyrite	6.09	6.09	6.09	90.0	90.0	90.0	0
Marcasite	5.00	6.15	3.75	90.0	90.0	90.0	4
Marcasite (Exp.)	5.02	6.20	3.75	90.0	90.0	90.0	
Krennerite	14.74	7.96	4.00	90.0	90.0	90.0	65
IrS_2-type	19.99	3.78	6.19	90.0	90.0	90.0	43
$IrTe_2$-type	19.25	3.72	4.95	90.0	84.4	90.0	64

Source: BITHER *et al.*;[51] BESSE; LIMA; DA SILVA;[118] KJEKSHUS; RAKKE; ANDRESEN.[125]

Table 38 – Equilibrium lattice parameters and relative total energies of $CuTe_2$ in the 11 studied crystal structures, obtained with PBE+D3, and reference experimental data. The PdS_2-type structure is changed to pyrite after relaxation.

Structure	a_0 (Å)	b_0 (Å)	c_0 (Å)	α (°)	β (°)	γ (°)	ΔE (meV/f.u.)
1T	3.99	3.99	5.00	90.0	90.0	120.0	2
1T′	4.95	4.02	15.37	90.0	90.0	90.0	95
2H	3.91	3.91	11.00	90.0	90.0	120.0	293
Calaverite	6.98	4.03	4.98	90.0	90.7	90.0	0
PdS_2-type	6.55	6.56	6.56	90.0	90.0	90.0	29
Pyrite	6.56	6.56	6.56	90.0	90.0	90.0	29
Pyrite (Exp.)	6.12	6.12	6.12	90.0	90.0	90.0	
distorted-Pyrite	6.56	6.56	6.56	90.0	90.0	90.0	29
Marcasite	5.48	6.68	3.99	90.0	90.0	90.0	68
Krennerite	16.01	8.55	4.25	90.0	90.0	90.0	2
IrS_2-type	21.98	4.03	6.68	90.0	90.0	90.0	99
$IrTe_2$-type	20.85	3.96	5.25	90.0	89.7	90.0	81

Source: BITHER *et al.*;[51] BESSE; LIMA; DA SILVA.[118]

Table 39 – Equilibrium lattice parameters and relative total energies of AgS_2 in the 11 studied crystal structures, obtained with PBE+D3. The PdS_2-type structure is changed to pyrite after relaxation.

Structure	a_0 (Å)	b_0 (Å)	c_0 (Å)	α (°)	β (°)	γ (°)	ΔE (meV/f.u.)
1T	3.71	3.71	4.42	90.0	90.0	120.0	926
1T′-derived	6.07	3.69	12.66	90.0	90.0	90.0	721
2H	4.10	4.10	9.08	90.0	90.0	120.0	1097
Calaverite	7.03	3.48	4.48	90.0	89.2	90.0	819
PdS_2-type	6.15	6.15	6.17	90.0	90.0	90.0	0
Pyrite	6.16	6.16	6.16	90.0	90.0	90.0	0
distorted-Pyrite	6.16	6.16	6.16	90.0	90.0	90.0	0
Marcasite	4.95	6.19	3.88	90.0	90.0	90.0	13
Krennerite	15.21	8.18	3.87	90.0	90.0	90.0	325
IrS_2-type	19.78	3.90	6.23	90.0	90.0	90.0	49
$IrTe_2$-type	19.04	3.87	4.97	90.0	81.4	90.0	68

Source: BESSE; LIMA; DA SILVA.[118]

Table 40 – Equilibrium lattice parameters and relative total energies of $AgSe_2$ in the 11 studied crystal structures, obtained with PBE+D3. The PdS_2-type structure is changed to pyrite after relaxation.

Structure	a_0 (Å)	b_0 (Å)	c_0 (Å)	α (°)	β (°)	γ (°)	ΔE (meV/f.u.)
1T	3.91	3.91	4.67	90.0	90.0	120.0	365
1T′	7.51	3.73	9.48	90.0	90.0	90.0	397
2H	3.68	3.68	10.76	90.0	90.0	120.0	862
Calaverite	7.30	3.78	4.68	90.0	89.8	90.0	283
PdS_2-type	6.48	6.48	6.48	90.0	90.0	90.0	0
Pyrite	6.48	6.48	6.48	90.0	90.0	90.0	0
distorted-Pyrite	6.48	6.48	6.48	90.0	90.0	90.0	0
Marcasite	5.27	6.56	4.01	90.0	90.0	90.0	15
Krennerite	15.46	8.48	4.12	90.0	90.0	90.0	86
IrS_2-type	21.06	4.04	6.60	90.0	90.0	90.0	51
$IrTe_2$-type	20.15	4.00	5.30	90.0	82.1	90.0	70

Source: BESSE; LIMA; DA SILVA.[118]

Table 41 – Equilibrium lattice parameters and relative total energies of $AgTe_2$ in the 11 studied crystal structures, obtained with PBE+D3. The PdS_2-type structure is changed to pyrite after relaxation.

Structure	a_0 (Å)	b_0 (Å)	c_0 (Å)	α (°)	β (°)	γ (°)	ΔE (meV/f.u.)
1T	4.22	4.22	5.07	90.0	90.0	120.0	81
1T′	4.38	4.48	17.69	90.0	90.0	90.0	169
2H	4.29	4.29	10.75	90.0	90.0	120.0	401
Calaverite	7.62	4.20	5.06	90.0	90.1	90.0	60
PdS_2-type	6.94	6.94	6.96	90.0	90.0	90.0	53
Pyrite	6.95	6.95	6.95	90.0	90.0	90.0	53
distorted-Pyrite	6.94	6.95	6.95	90.0	90.0	90.0	53
Marcasite	5.75	7.10	4.23	90.0	90.0	90.0	80
Krennerite	16.58	9.02	4.37	90.0	90.0	90.0	0
IrS_2-type	22.88	4.26	7.14	90.0	90.0	90.0	112
$IrTe_2$-type	22.44	4.21	5.45	90.0	90.1	90.0	122

Source: BESSE; LIMA; DA SILVA.[118]

Table 42 – Equilibrium lattice parameters and relative total energies of AuS_2 in the 11 studied crystal structures, obtained with PBE+D3.

Structure	a_0 (Å)	b_0 (Å)	c_0 (Å)	α (°)	β (°)	γ (°)	ΔE (meV/f.u.)
1T	3.71	3.71	4.38	90.0	90.0	120.0	424
1T′	6.35	3.75	9.43	90.0	90.0	90.0	662
2H	4.03	4.03	9.16	90.0	90.0	120.0	1540
Calaverite	6.43	3.72	4.37	90.0	89.9	90.0	428
PdS_2-type	5.64	6.20	7.17	90.0	90.0	90.0	148
Pyrite	6.15	6.15	6.15	90.0	90.0	90.0	184
distorted-Pyrite	6.15	6.14	6.15	90.0	90.0	90.0	184
Marcasite	5.17	5.72	4.10	90.0	90.0	90.0	183
Krennerite	15.29	7.82	4.02	90.0	90.0	90.0	0
IrS_2-type	16.93	3.72	7.69	90.0	90.0	90.0	374
$IrTe_2$-type	22.46	3.64	4.62	90.0	82.0	90.0	294

Source: BESSE; LIMA; DA SILVA.[118]

Table 43 – Equilibrium lattice parameters and relative total energies of $AuSe_2$ in the 11 studied crystal structures, obtained with PBE+D3.

Structure	a_0 (Å)	b_0 (Å)	c_0 (Å)	α (°)	β (°)	γ (°)	ΔE (meV/f.u.)
1T	3.90	3.90	4.65	90.0	90.0	120.0	126
1T′	6.78	3.91	9.82	90.0	90.0	90.0	331
2H	3.66	3.66	10.79	90.0	90.0	120.0	879
Calaverite	6.75	3.89	4.66	90.0	89.9	90.0	122
PdS_2-type	6.05	6.44	7.22	90.0	90.0	90.0	278
Pyrite	6.46	6.46	6.46	90.0	90.0	90.0	273
distorted-Pyrite	6.46	6.46	6.46	90.0	90.0	90.0	273
Marcasite	5.26	6.48	4.04	90.0	90.0	90.0	291
Krennerite	15.52	8.20	4.13	90.0	90.0	90.0	0
IrS_2-type	21.96	4.14	6.15	90.0	90.0	90.0	304
$IrTe_2$-type	21.68	3.90	5.01	90.0	89.9	90.0	228

Source: BESSE; LIMA; DA SILVA.[118]

Table 44 – Equilibrium lattice parameters and relative total energies of $AuTe_2$ in the 11 studied crystal structures, obtained with PBE+D3, and reference experimental data. The PdS_2-type structure is changed to pyrite after relaxation.

Structure	a_0 (Å)	b_0 (Å)	c_0 (Å)	α (°)	β (°)	γ (°)	ΔE (meV/f.u.)
1T	4.19	4.19	5.04	90.0	90.0	120.0	11
1T (Exp.)	4.11	4.11	5.03	90.0	90.0	120.0	
1T′	7.05	4.08	10.82	90.0	90.0	90.0	211
2H	3.94	3.94	11.57	90.0	90.0	120.0	579
Calaverite	7.25	4.18	5.06	90.0	89.9	90.0	6
Calaverite (Exp.)	7.19	4.41	5.07	90.0	90.0	90.0	
PdS_2-type	6.91	6.90	6.91	90.0	90.0	90.0	359
Pyrite	6.89	6.89	6.89	90.0	90.0	90.0	359
distorted-Pyrite	6.90	6.89	6.89	90.0	90.0	90.0	359
Marcasite	5.73	7.03	4.23	90.0	90.0	90.0	400
Krennerite	16.56	8.78	4.38	90.0	90.0	90.0	0
Krennerite (Exp.)	16.51	8.80	4.45	90.0	90.0	90.0	
IrS_2-type	18.00	4.06	9.58	90.0	90.0	90.0	302
$IrTe_2$-type	22.64	4.14	5.28	90.0	90.3	90.0	292

Source: BESSE; LIMA; DA SILVA;[118] REITHMAYER *et al.*;[121] TUNELL; KSANDA.[128]

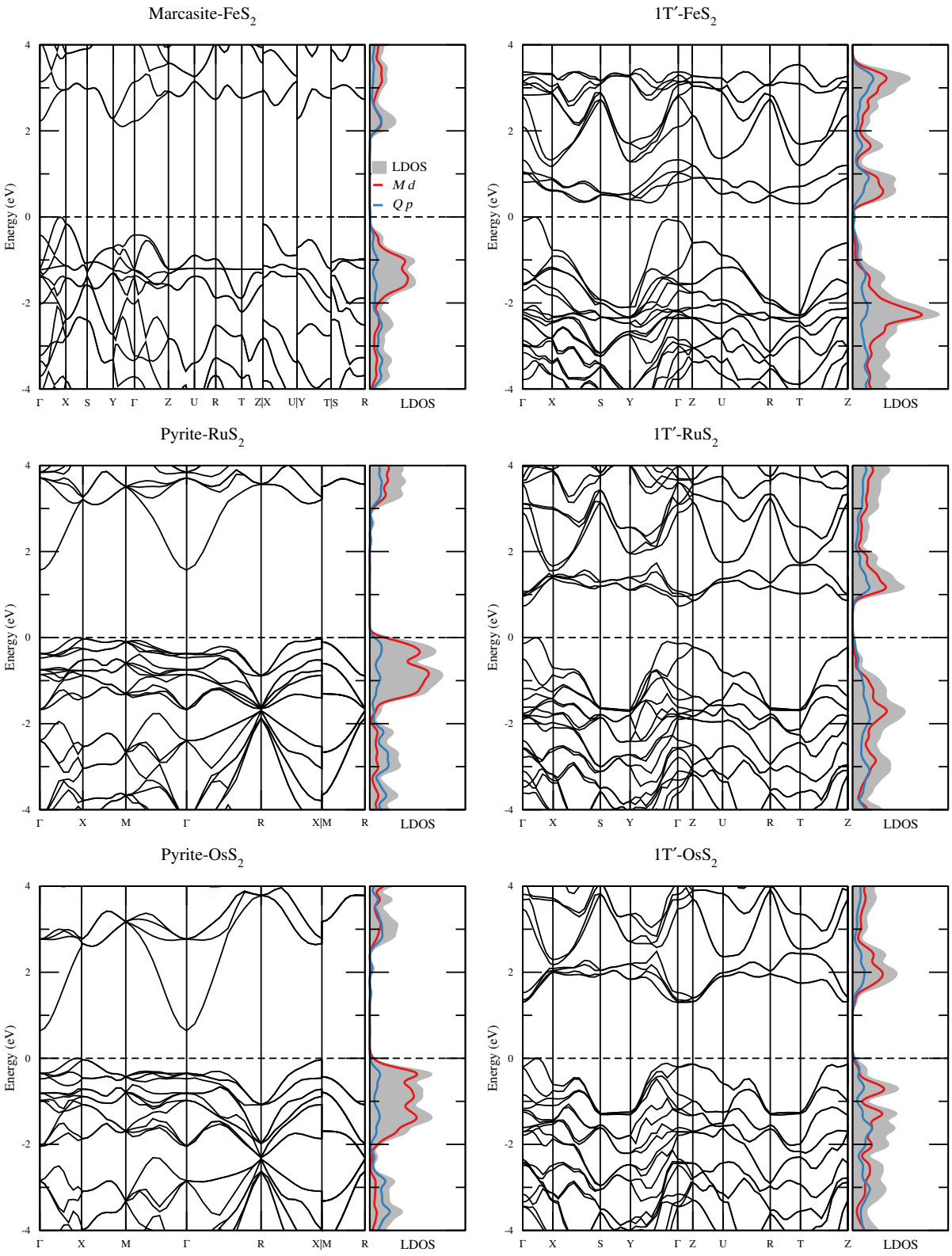

Figure 31 – DFT-HSE06 electronic band structures of the lowest energy 3D and 2D crystals of the Fe-group sulfides (MS_2, M = Fe, Ru, Os). Zero energy is set to the VBM, indicated by horizontal dashed line.

Source: By the author.

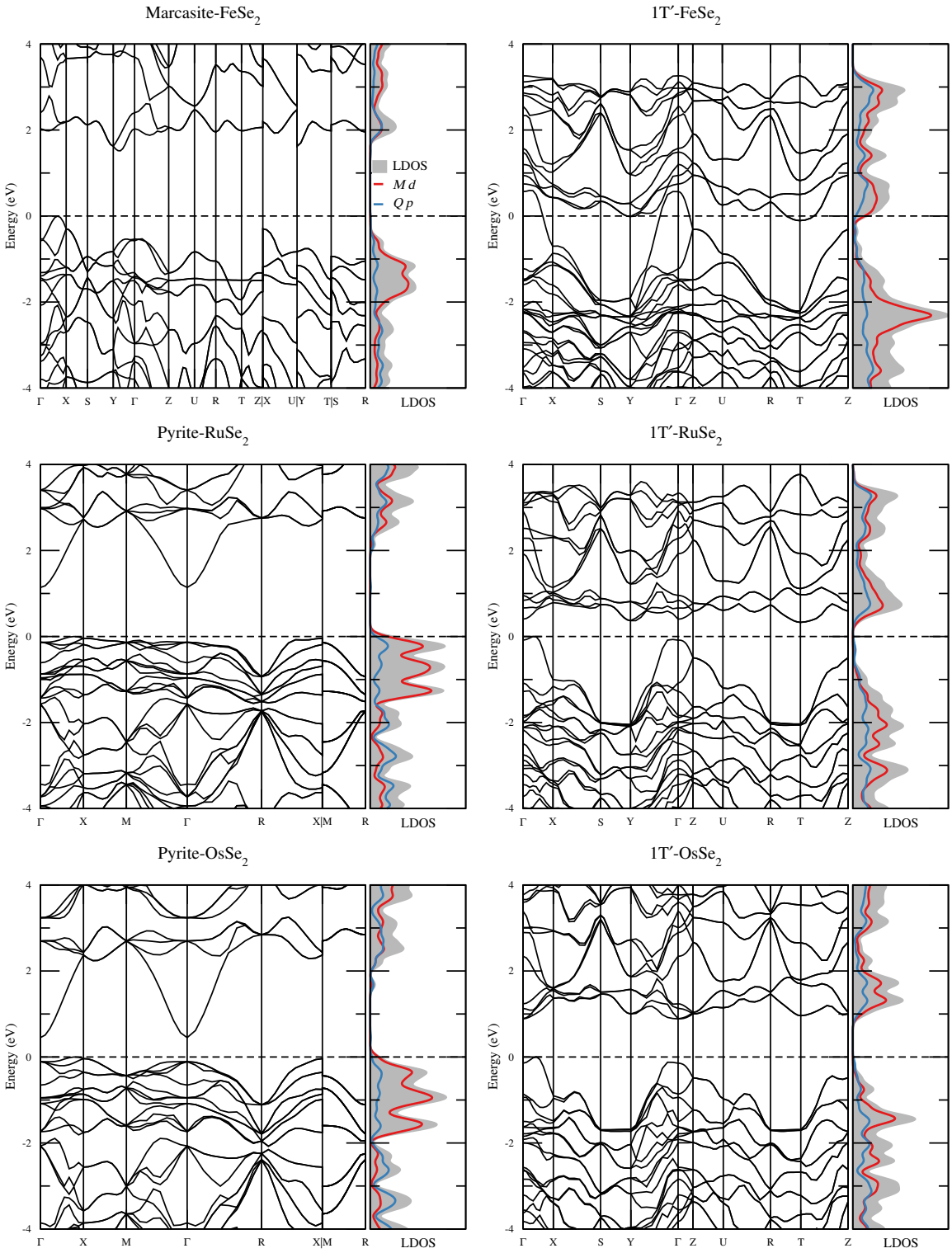

Figure 32 – DFT-HSE06 electronic band structures of the lowest energy 3D and 2D crystals of the Fe-group selenides (MSe$_2$, M = Fe, Ru, Os). Zero energy is set to the VBM, indicated by horizontal dashed line.

Source: By the author.

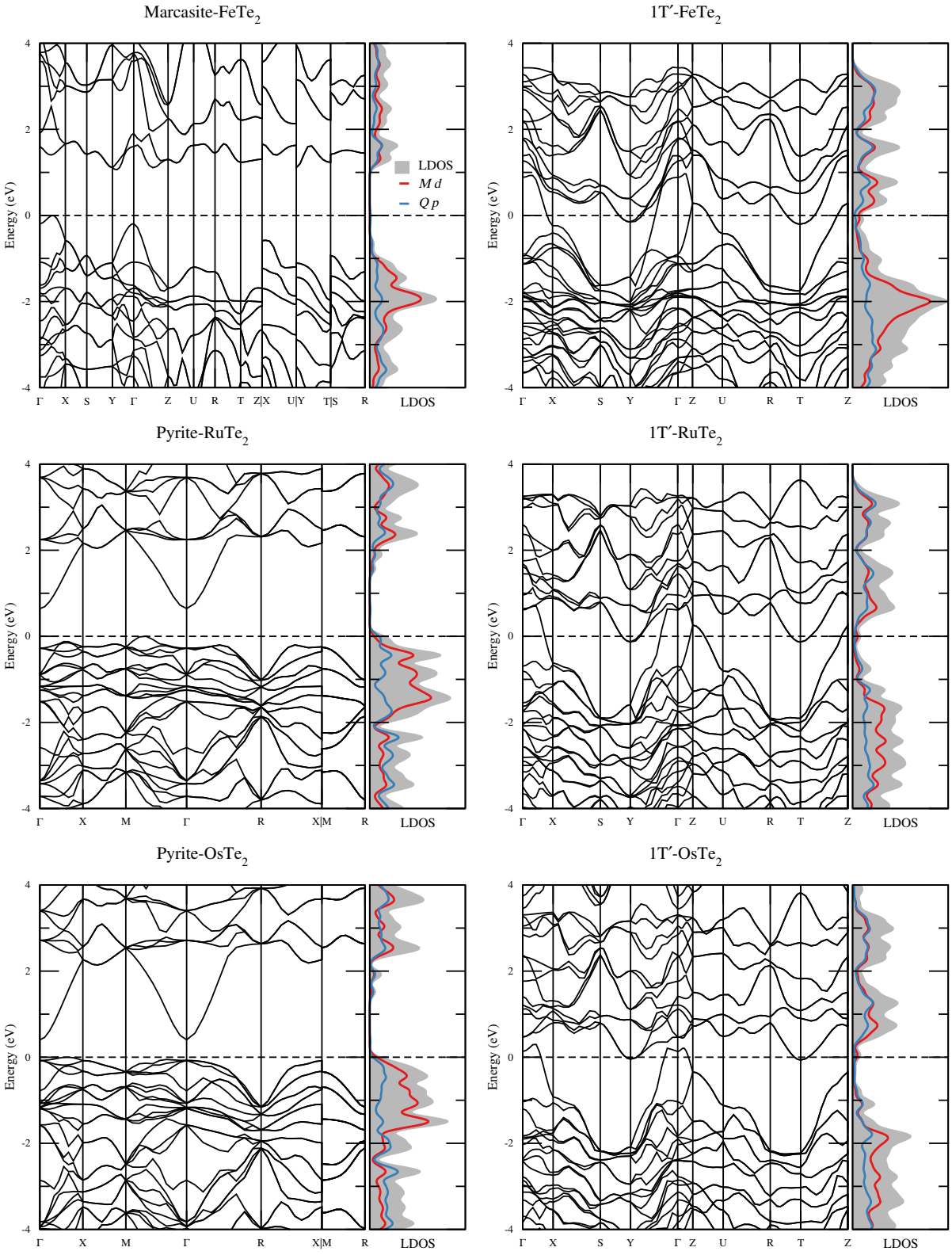

Figure 33 – DFT-HSE06 electronic band structures of the lowest energy 3D and 2D crystals of the Fe-group tellurides ($M\text{Te}_2$, M = Fe, Ru, Os). Zero energy is set to the VBM, indicated by horizontal dashed line.

Source: By the author.

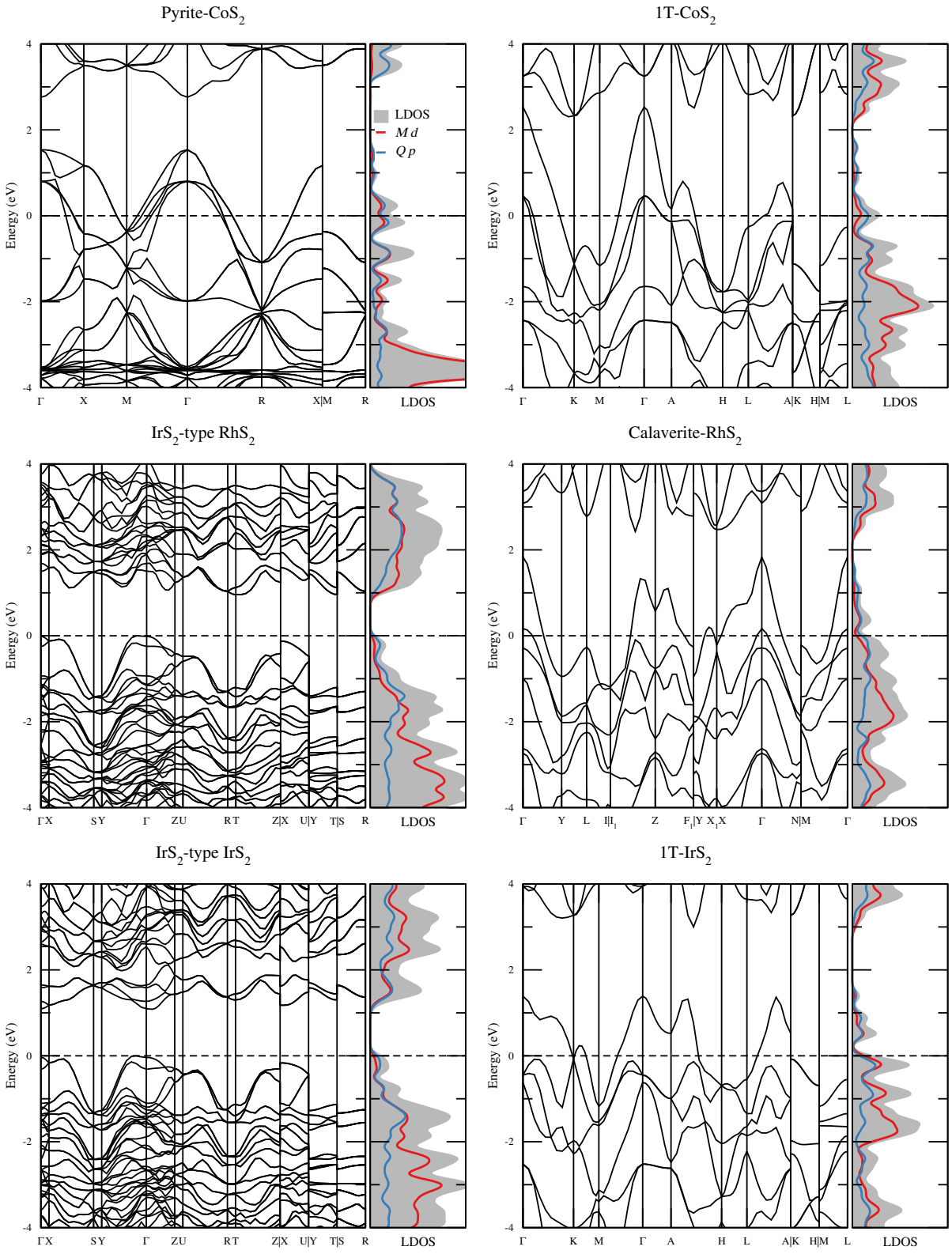

Figure 34 – DFT-HSE06 electronic band structures of the lowest energy 3D and 2D crystals of the Co-group sulfides (MS_2, M = Co, Rh, Ir). Zero energy is set to the VBM, indicated by horizontal dashed line.

Source: By the author.

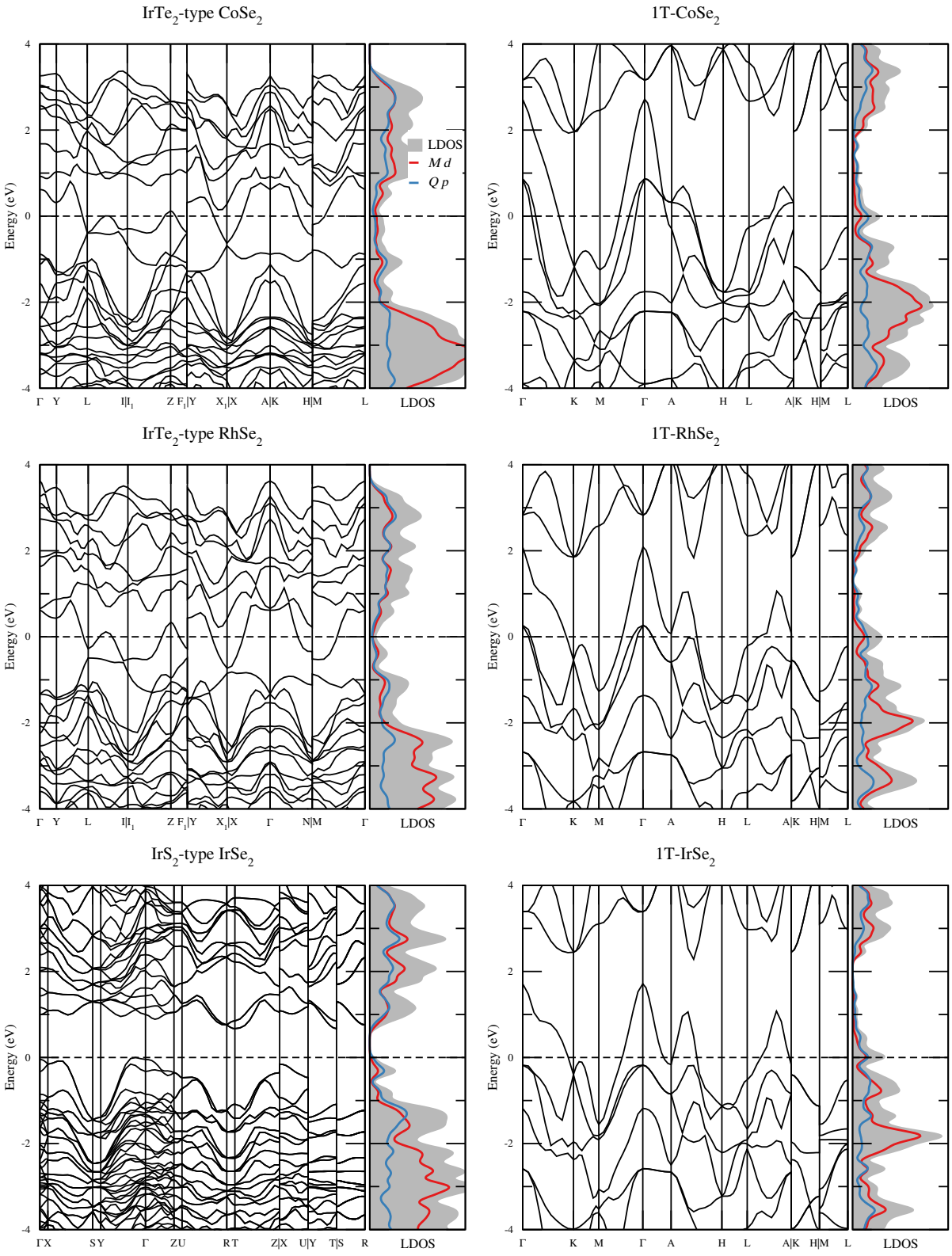

Figure 35 – DFT-HSE06 electronic band structures of the lowest energy 3D and 2D crystals of the Co-group selenides (MSe$_2$, M = Co, Rh, Ir). Zero energy is set to the VBM, indicated by horizontal dashed line.

Source: By the author.

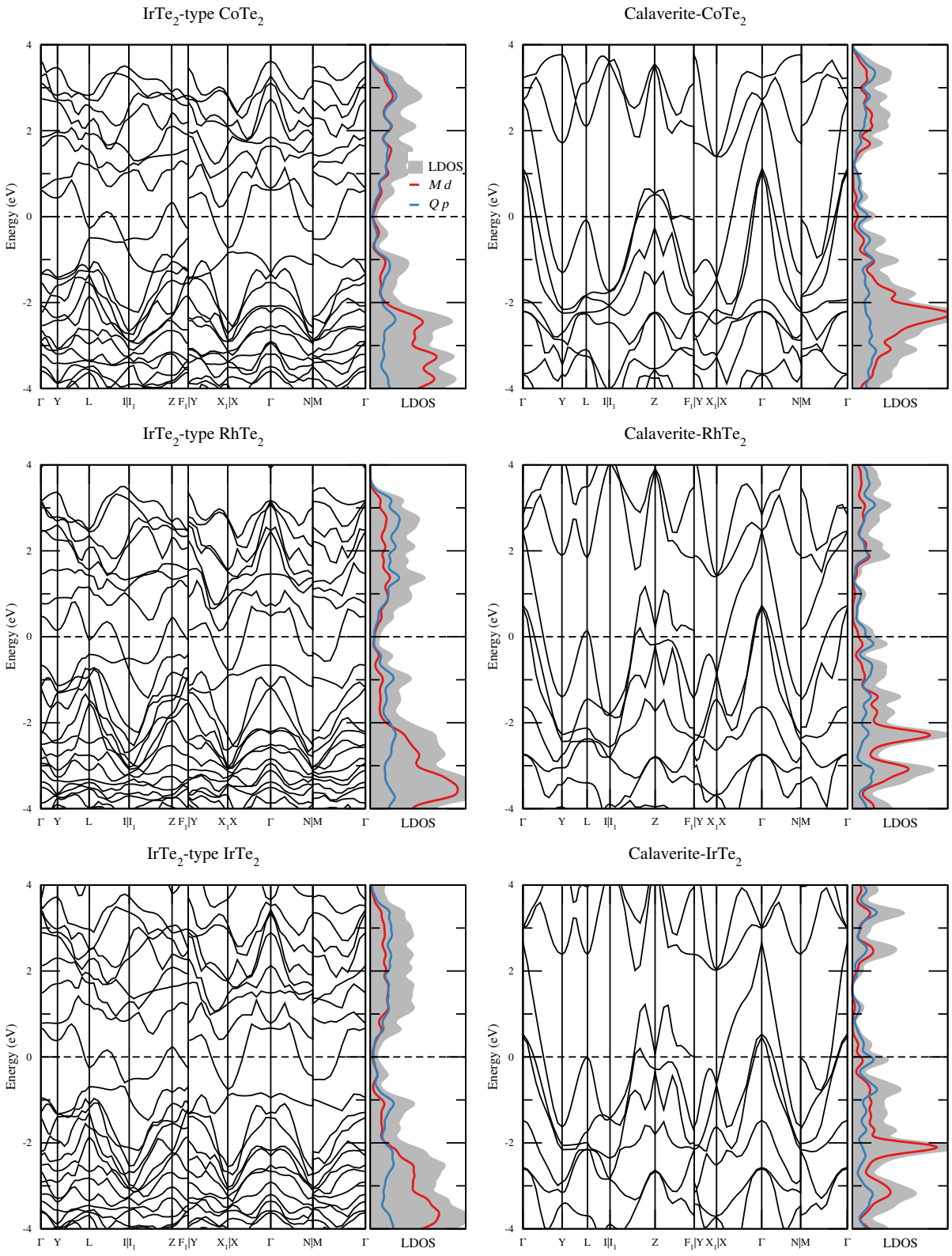

Figure 36 – DFT-HSE06 electronic band structures of the lowest energy 3D and 2D crystals of the Co-group tellurides ($M\text{Te}_2$, M = Co, Rh, Ir). Zero energy is set to the VBM, indicated by horizontal dashed line.

Source: By the author.

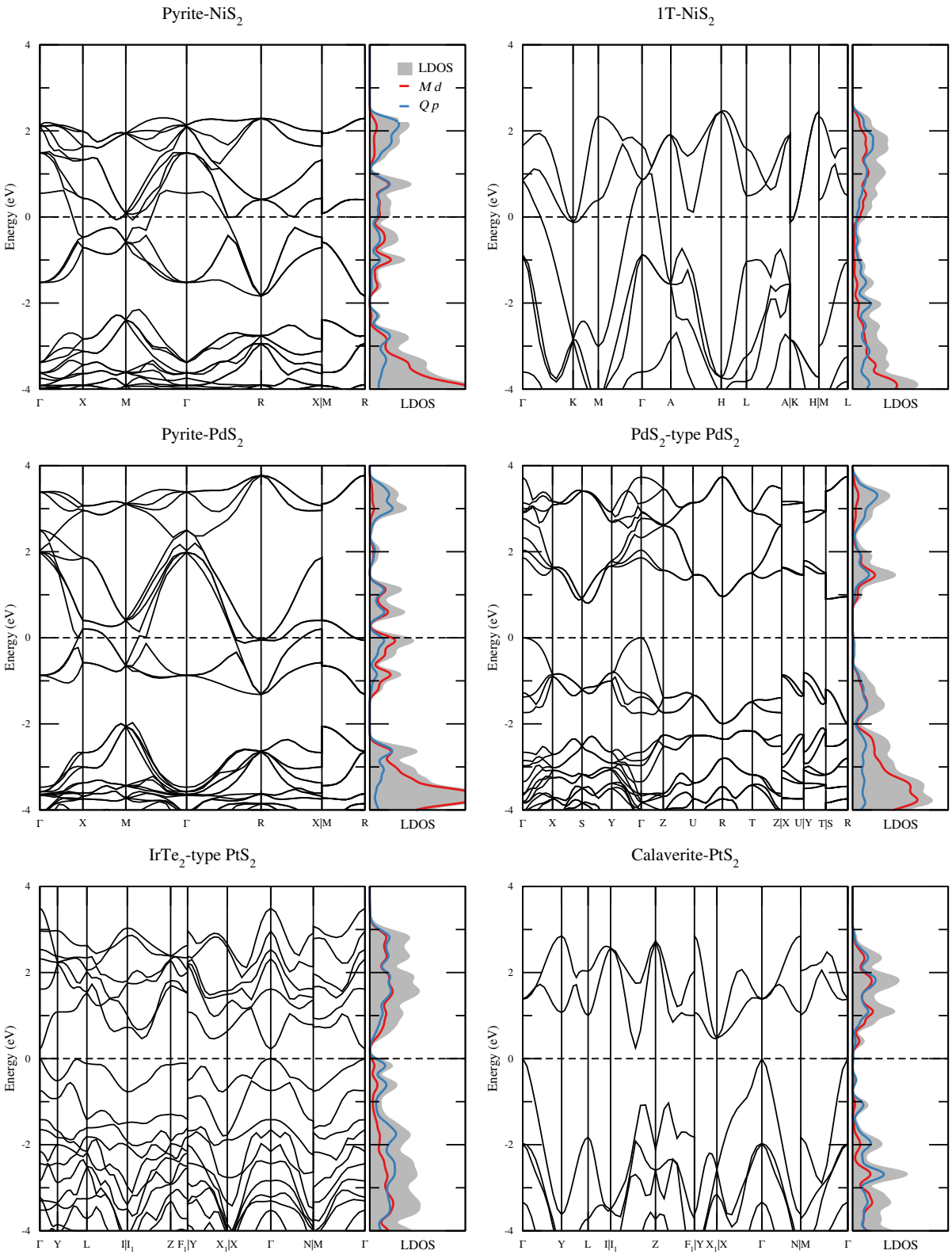

Figure 37 – DFT-HSE06 electronic band structures of the lowest energy 3D and 2D crystals of the Ni-group sulfides (MS_2, M = Ni, Pd, Pt). Zero energy is set to the VBM, indicated by horizontal dashed line.

Source: By the author.

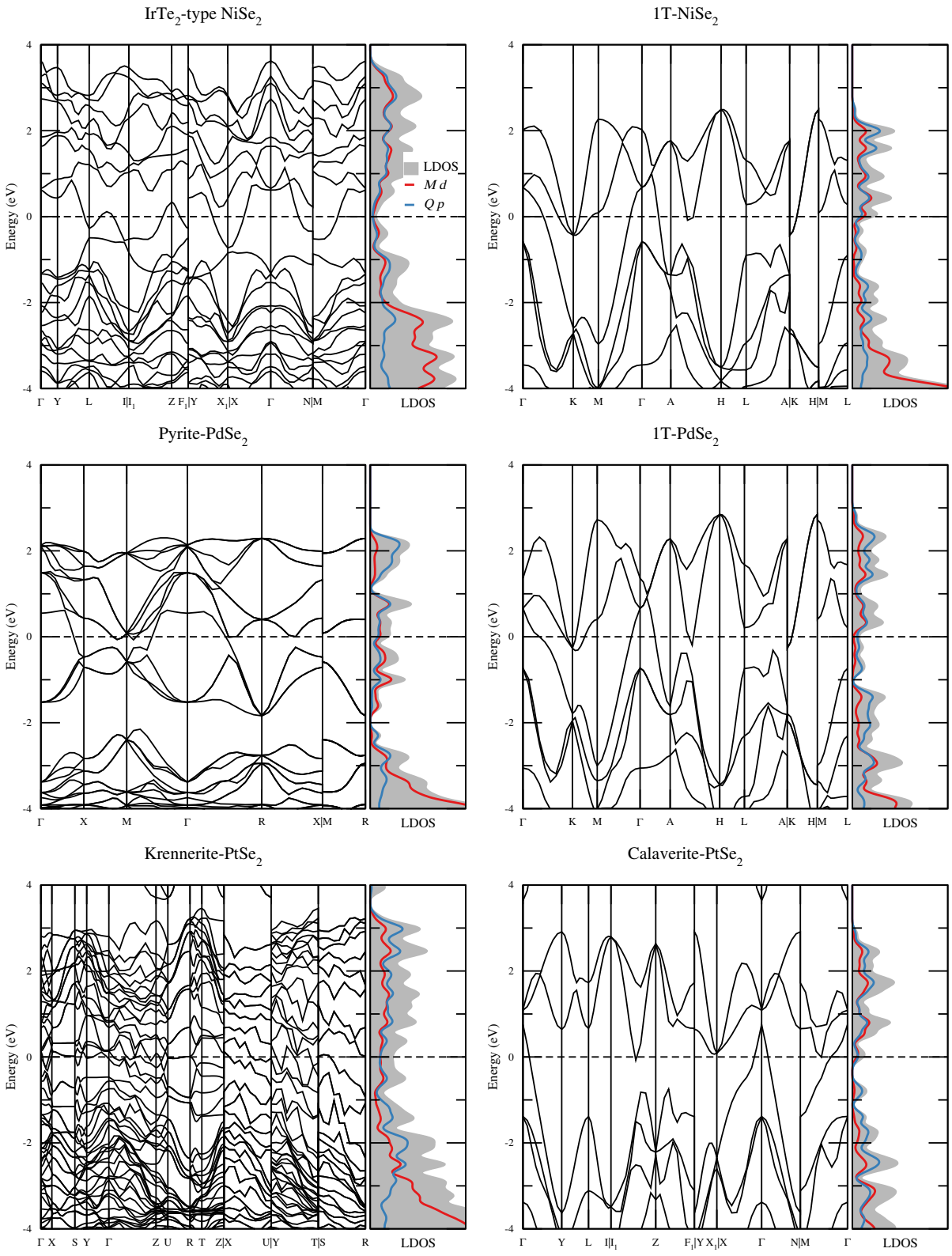

Figure 38 – DFT-HSE06 electronic band structures of the lowest energy 3D and 2D crystals of the Ni-group selenides (MSe$_2$, M = Ni, Pd, Pt). Zero energy is set to the VBM, indicated by horizontal dashed line.

Source: By the author.

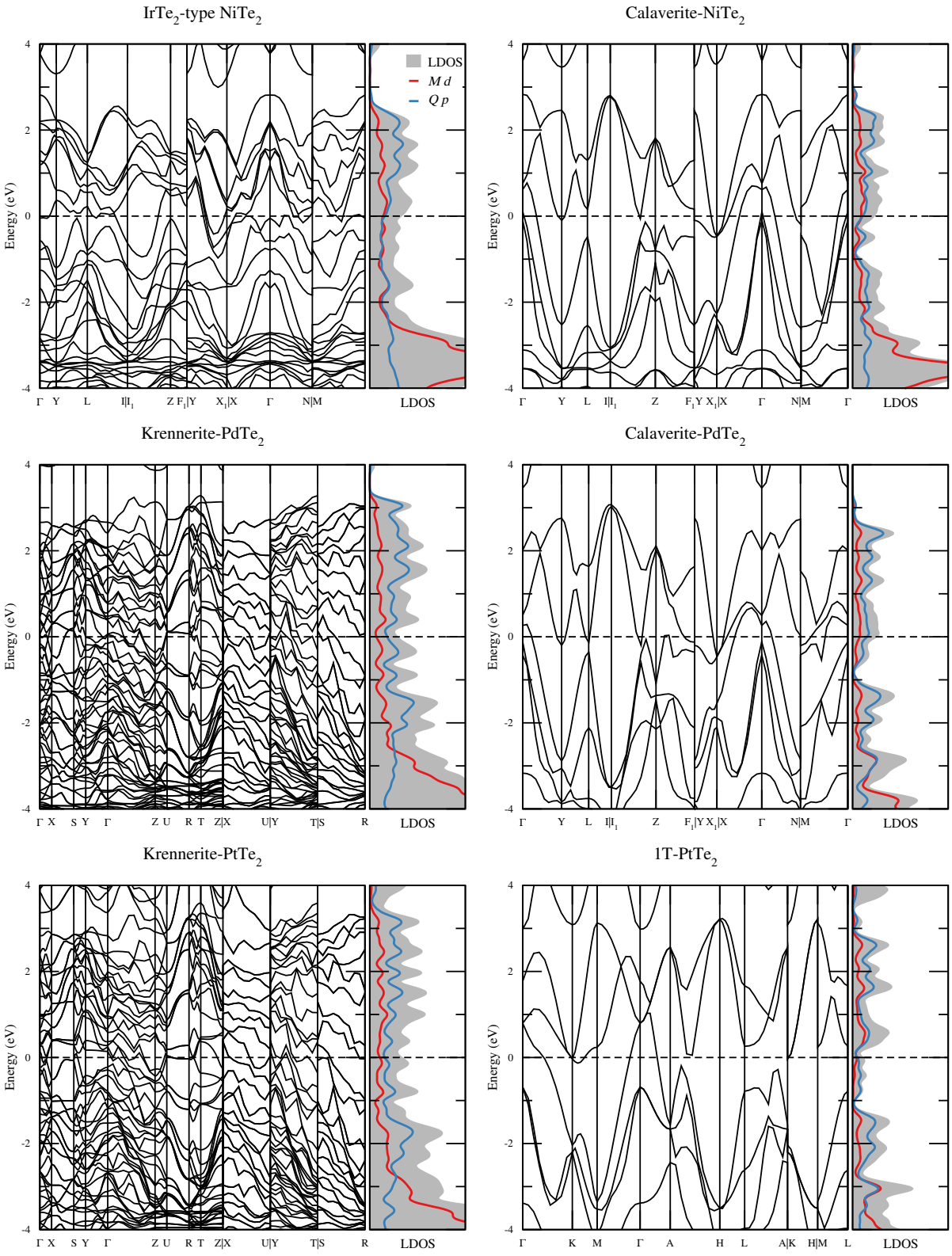

Figure 39 – DFT-HSE06 electronic band structures of the lowest energy 3D and 2D crystals of the Ni-group tellurides (MTe$_2$, M = Ni, Pd, Pt). Zero energy is set to the VBM, indicated by horizontal dashed line.

Source: By the author.

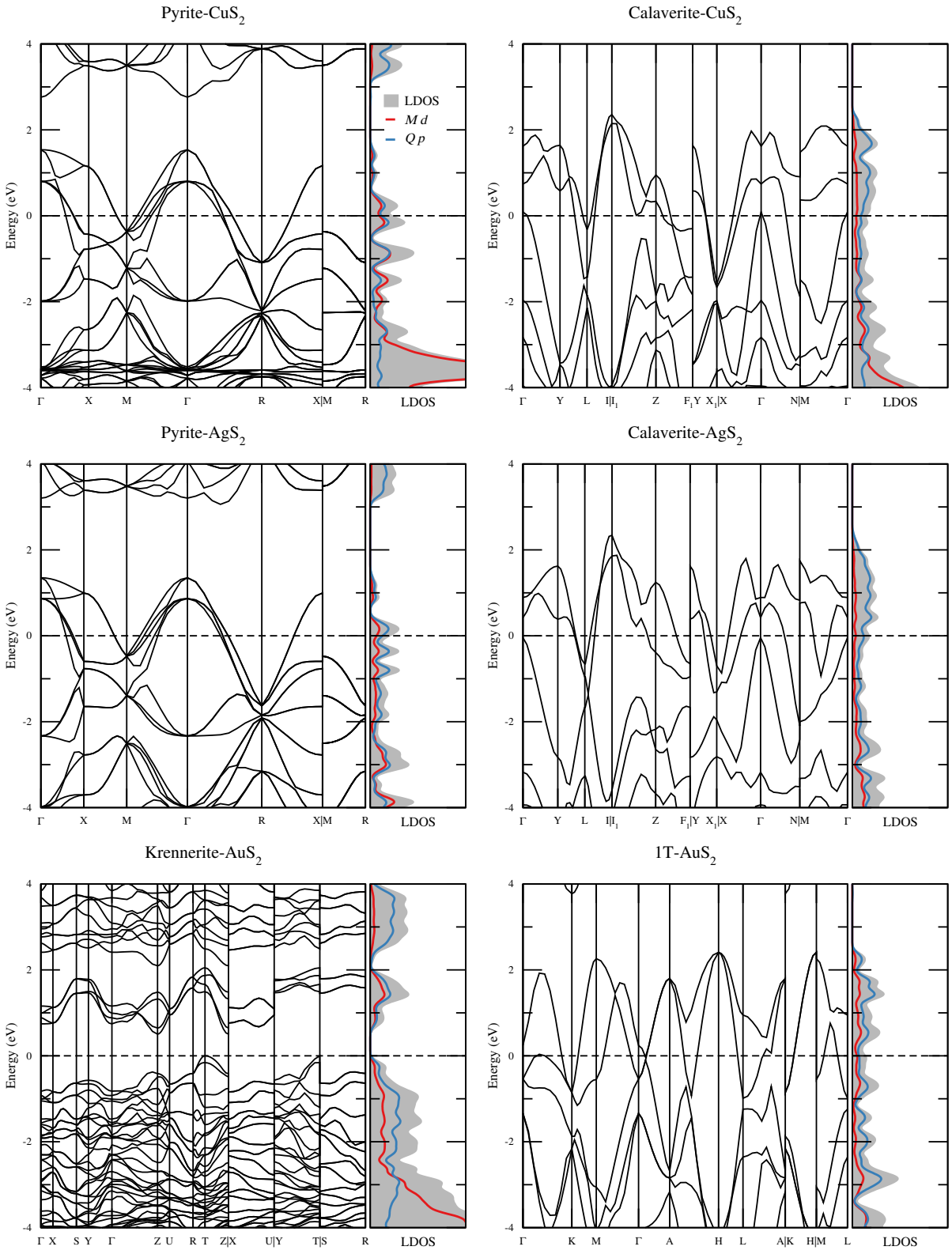

Figure 40 – DFT-HSE06 electronic band structures of the lowest energy 3D and 2D crystals of the Cu-group sulfides (MS_2, M = Cu, Ag, Au). Zero energy is set to the VBM, indicated by horizontal dashed line.

Source: By the author.

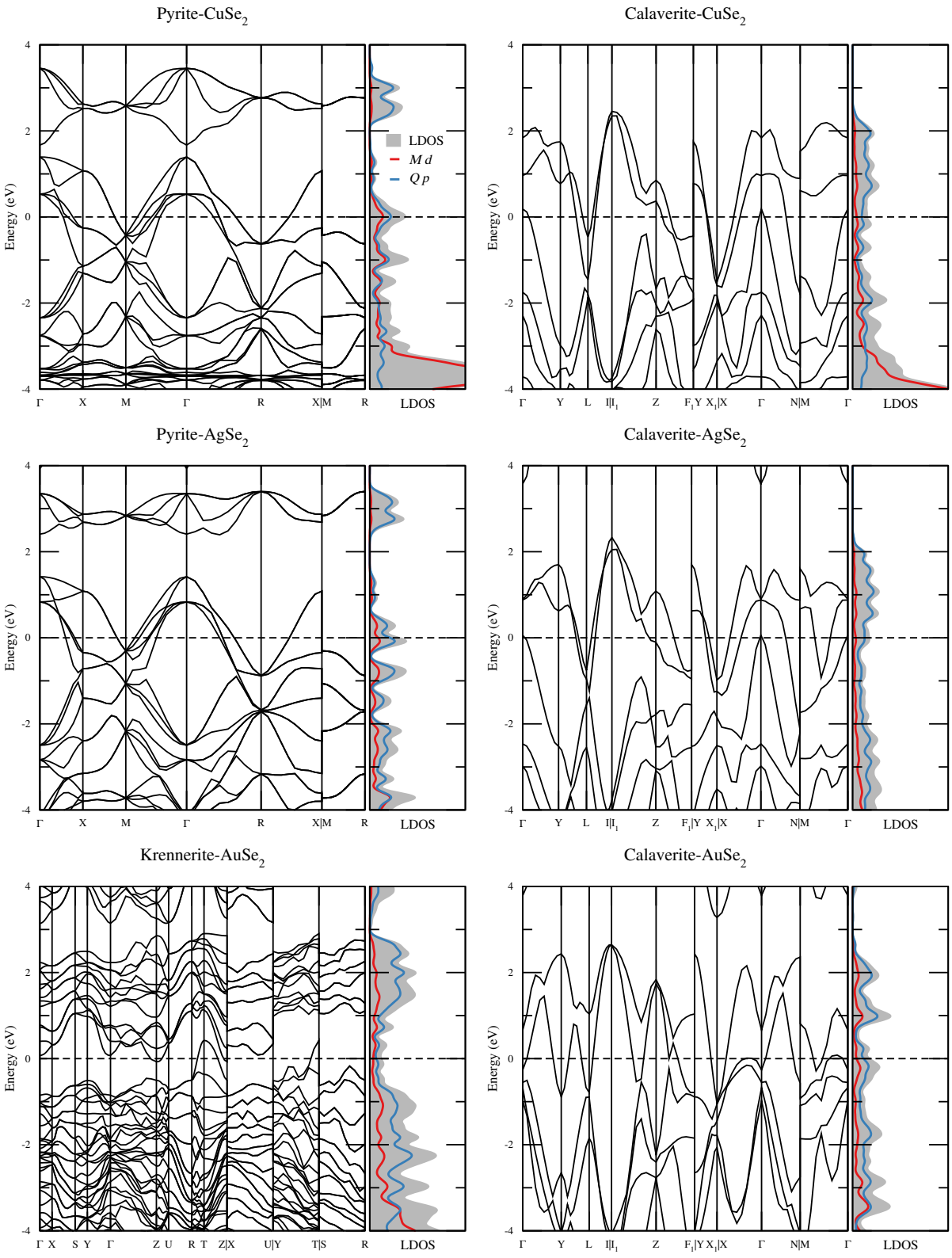

Figure 41 – DFT-HSE06 electronic band structures of the lowest energy 3D and 2D crystals of the Cu-group selenides (MSe$_2$, M = Cu, Ag, Au). Zero energy is set to the VBM, indicated by horizontal dashed line.

Source: By the author.

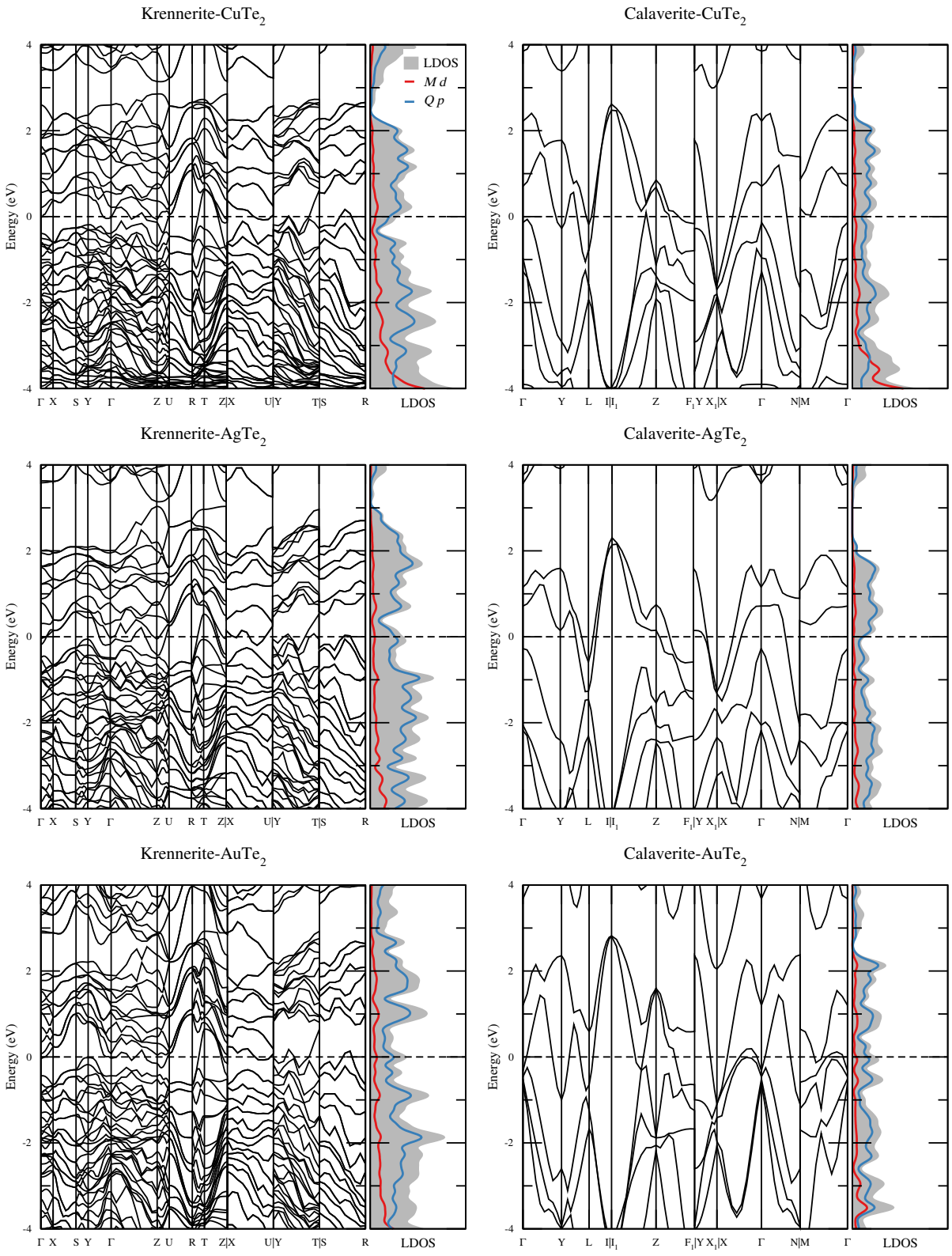

Figure 42 – DFT-HSE06 electronic band structures of the lowest energy 3D and 2D crystals of the Cu-group tellurides (MTe$_2$, M = Cu, Ag, Au). Zero energy is set to the VBM, indicated by horizontal dashed line.

Source: By the author.

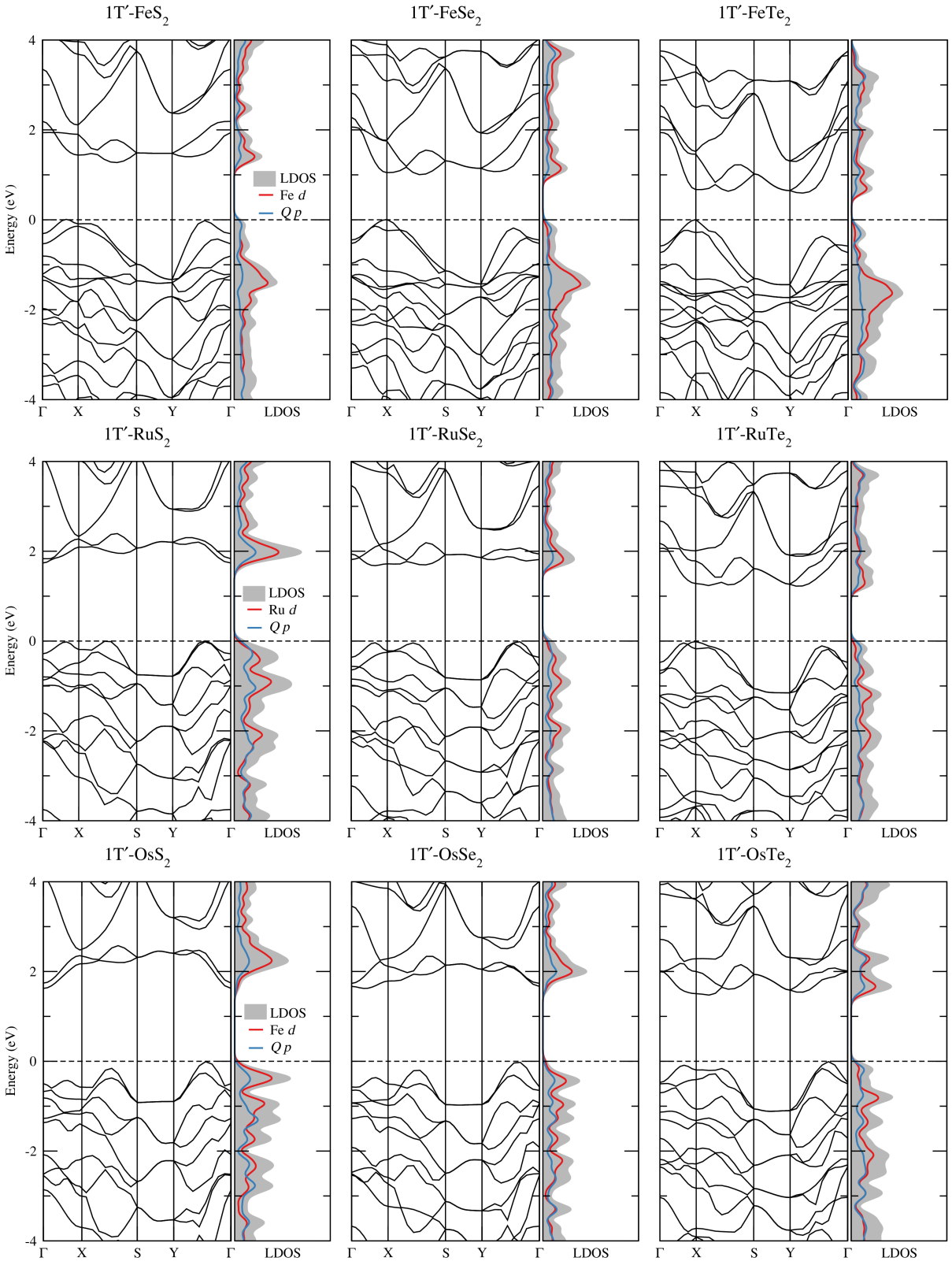

Figure 43 – DFT-HSE06 electronic band structures of monolayers of the Fe-group TMDs (MQ_2, M = Fe, Ru, Os; Q = S, Se, Te). Zero energy is set to the VBM, indicated by horizontal dashed line.

Source: By the author.

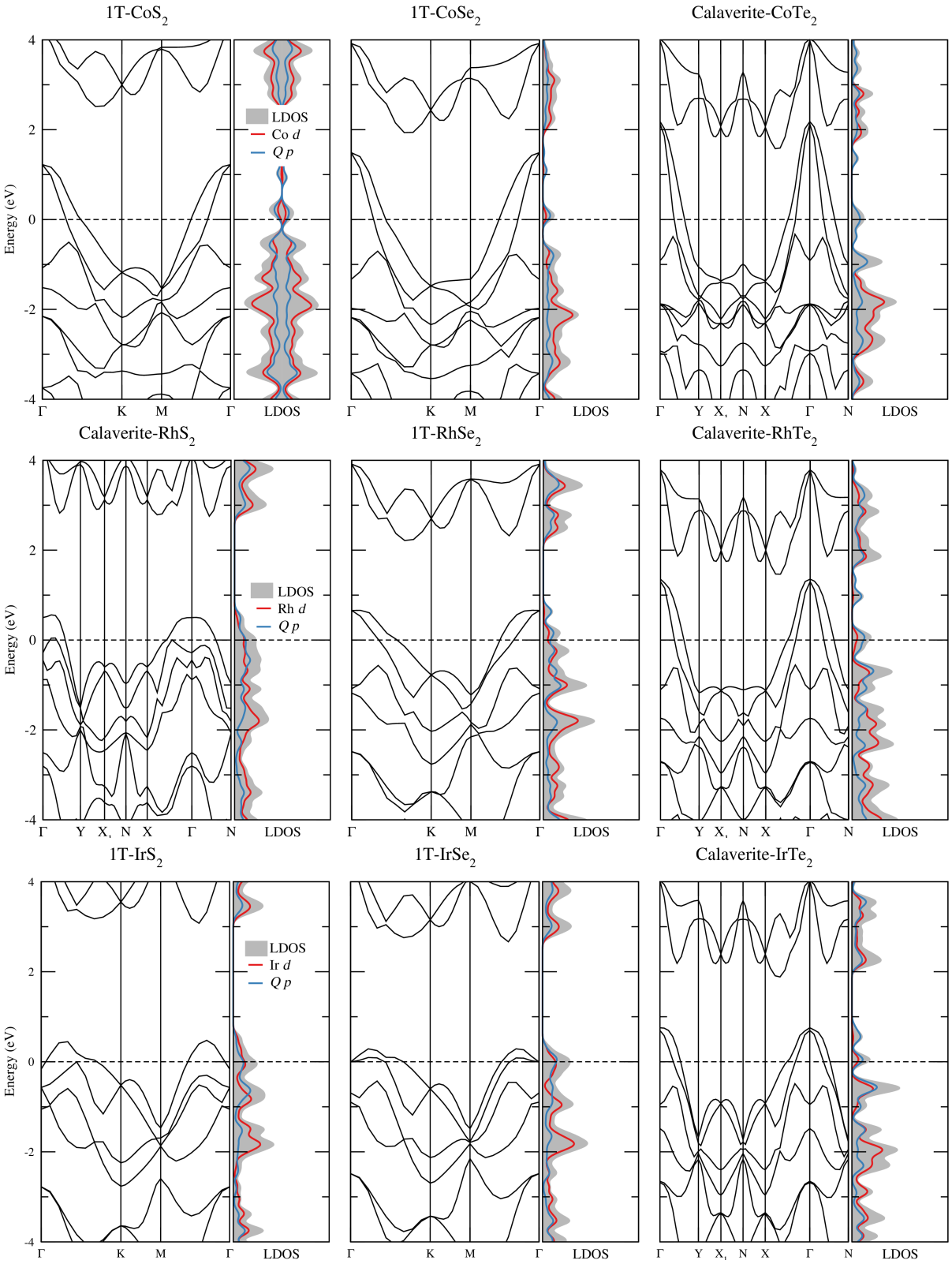

Figure 44 – DFT-HSE06 electronic band structures of monolayers of the Co-group TMDs (MQ_2, M = Co, Rh, Ir; Q = S, Se, Te). Zero energy is set to the VBM, indicated by horizontal dashed line.

Source: By the author.

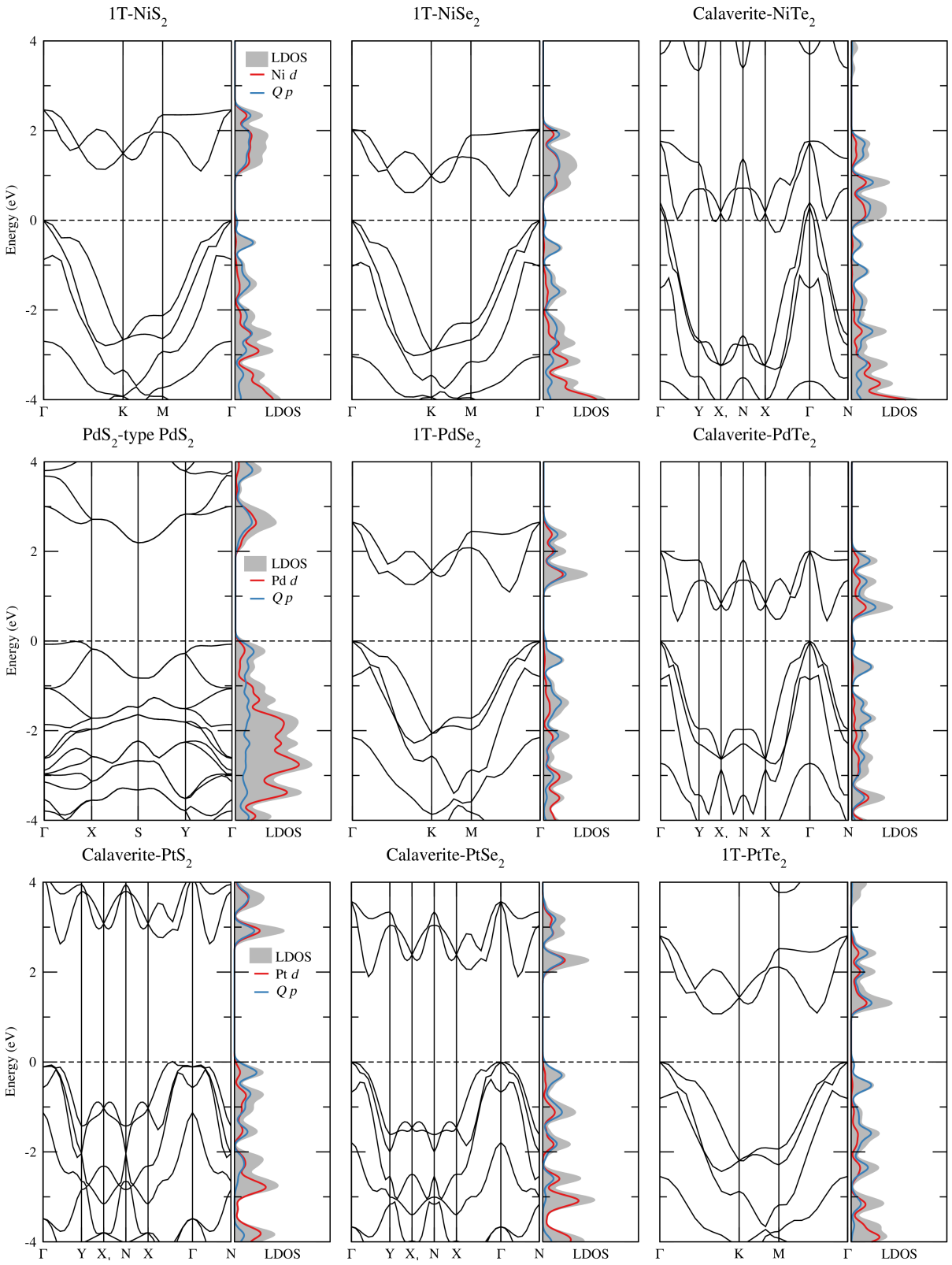

Figure 45 – DFT-HSE06 electronic band structures of monolayers of the Ni-group TMDs (MQ_2, M = Ni, Pd, Pt; Q = S, Se, Te). Zero energy is set to the VBM, indicated by horizontal dashed line.

Source: By the author.

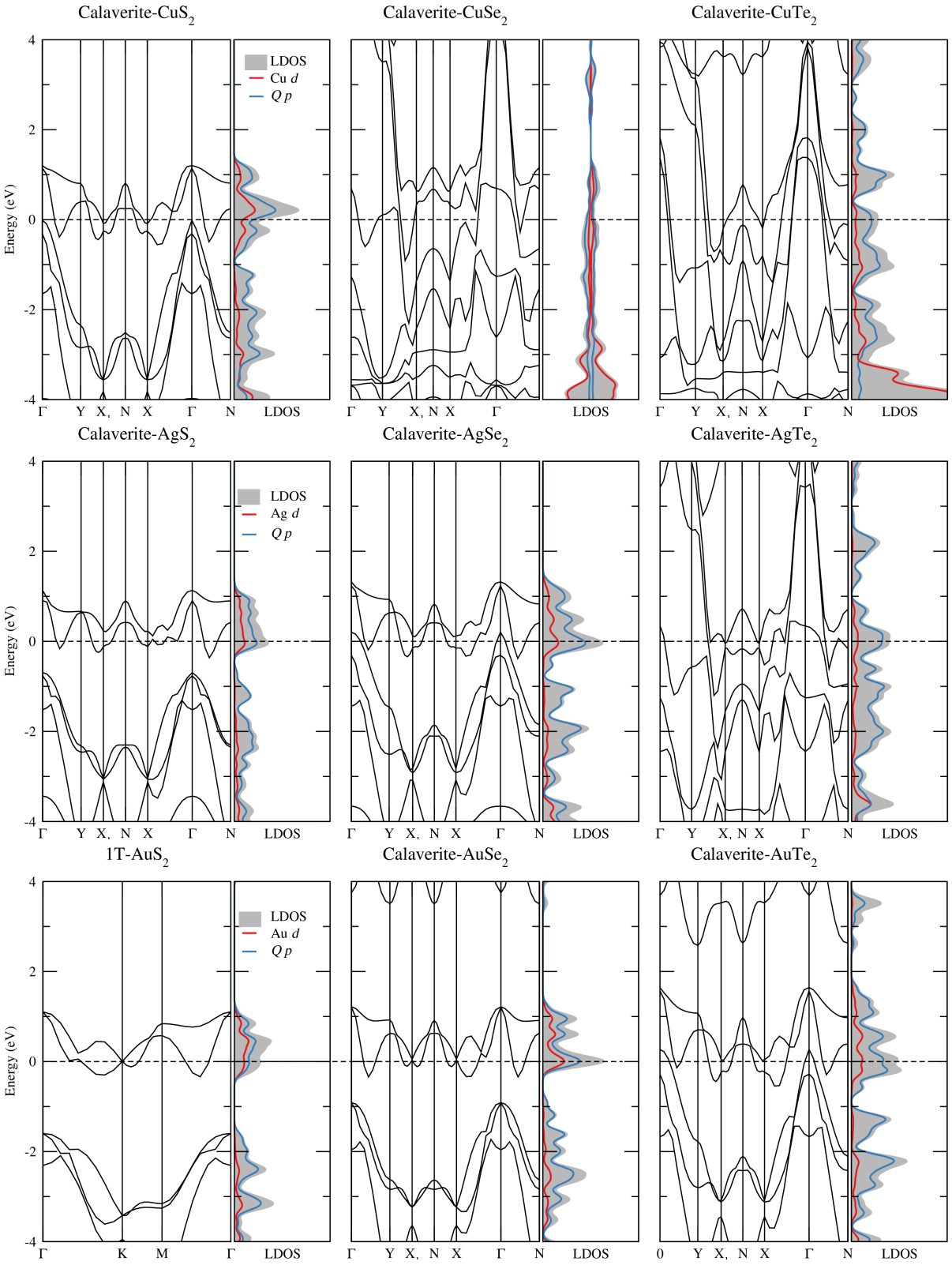

Figure 46 – DFT-HSE06 electronic band structures of monolayers of the Cu-group TMDs (MQ_2, M = Cu, Ag, Au; Q = S, Se, Te). Zero energy is set to the VBM, indicated by horizontal dashed line.

Source: By the author.

APPENDIX C – BAND STRUCTURES OF VAN DER WAALS HETEROBILAYERS

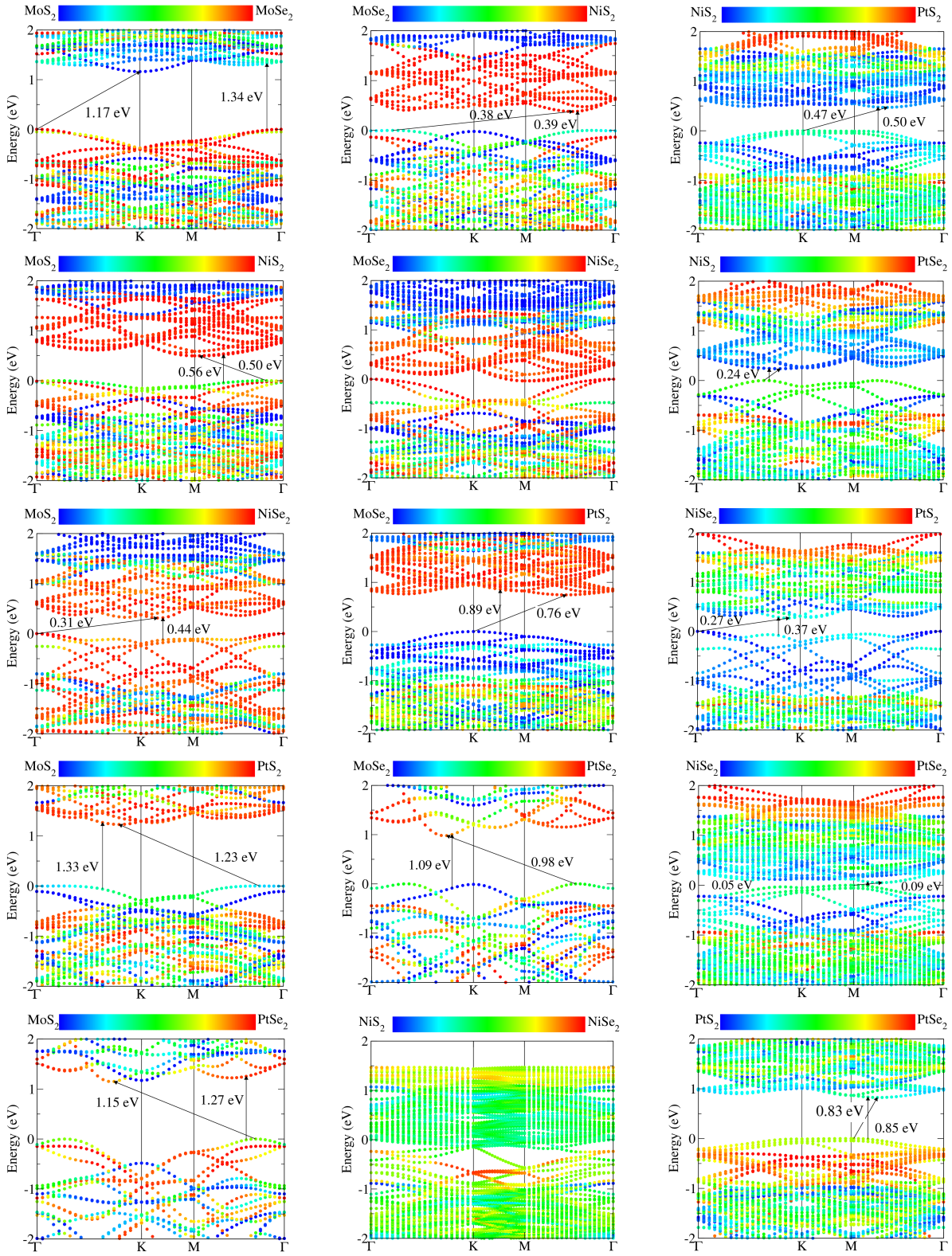

Figure 47 – Band structures of the heterobilayers of MQ_2 monolayers (M = Mo, Ni, and Pt; Q = S, Se). The color scale denotes the local projection of states onto each monolayer. For each system, the band gap and smallest direct band gap are indicated, and the VBM is at zero energy.

Source: By the author.